Battery Degradation Modeling For Vehicle Applications

by

Thomas Dylan Finley

A thesis

presented to the University of Waterloo

in fulfillment of the

thesis requirement for the degree of

Masters of Applied Science

in

Chemical Engineering

Waterloo, Ontario, Canada, 2014

AUTHOR'S DECLARATION

I hereby declare that I am the sole author of this thesis. This is a true copy of the thesis, including any required final revisions, as accepted by my examiners.

I understand that my thesis may be made electronically available to the public.

Abstract

Fuel efficiency is a fundamental part of the automotive industry and its impact on the global environment. This is a direct result of the Corporate Average Fuel Efficiency (CAFE) standards imposing a 70% improvement of fuel efficiency on all light duty line-ups between 2014 and 2025. To achieve such an improvement, automotive manufacturers will need to electrify their powertrains. Lithium ion battery technology has emerged as a leading component in electrification with the development of hybrid, plug-in hybrid, and battery electric vehicles. Therefore, the design and sizing of these battery packs must be accurate.

The correct design and sizing of a battery pack must account for the lifetime of the battery. In plug-in hybrid and battery electric vehicles, the battery pack is directly responsible for the all-electric range of that vehicle. As the battery ages, this range decreases. Convention has been to size the battery to account for a 20% loss in electric range; however the degradation rate varies from vehicle to vehicle depending on the driver's behavior. The convention can lead to severely oversized battery packs, which decreases operational efficiencies, and increases vehicle mass, and greenhouse gas emissions. Therefore, it is important to consider realistic driver behavior when sizing the battery pack.

The A123 AMP20 pouch battery was selected for the degradation analysis. A semi-empirical single particle battery degradation model was developed in MATLAB Simulink for the AMP20. 2 mAh half-cell coin cells were built from the AMP20 materials and cycled at C/50 to obtain a close approximation of the electrode open circuit potentials at various states of lithiation. The open circuit potentials were used in the single particle model. Additionally, rate capability tests and degradation cycling are conducted on the AMP20 to fit the single particle model parameters. The LFP particle resistance was empirically fit and depended upon the state of lithiation and whether the battery was charging or discharging.

A sensitivity analysis of the Tafel equation was performed to determine that the parasitic current density was a function of the negative electrode potential, the solid electrolyte interface (SEI) film resistance, and the negative electrode current density. The operational state-of-charge (SOC), the depth-of-discharge (DOD), the history of the battery, and the battery current are all vehicle parameters that impact the parasitic current density. For low current operations, a change in the SOC will yield the largest change in parasitic current density. For high current operation of a fresh battery, a change in the SEI resistance yields the largest change in parasitic current density; while an aged

battery yields the largest change in parasitic current density from a change in battery current. It was determined that the SEI resistance did not prove to be a significant factor affecting battery degradation. It was also determined that a long charging time, a high operational SOC, a large DOD, and aggressive current demand are primary factors that increase battery degradation.

Simulations on the single particle model were conducted to assess the degradation rates of common Environmental Protection Agency (EPA) drive cycles. The simulation results showed that the degradation rate significantly depends upon the duty cycle. The UDDS cycle degraded the battery at a dramatically faster rate than the US06 and HWFET cycles for 80% initial SOC, 17.41, 3.08, and 4.64 (µAh Li+)(Ah Processed)$^{-1}$; at 50% initial SOC, 7.04, 1.79, and 2.14 (µAh Li+)(Ah Processed)$^{-1}$; and at 20% initial SOC, 1.85, 0.46, and 0.54 (µAh Li+)(Ah Processed)$^{-1}$. It was concluded that the operational SOC, the charging time, and the current demand are the primary factors that affect the degradation rate of a duty cycle. Further simulations were performed with 1C charging after the duty cycle to return the operational SOC to its initial value and to account for the duty cycle DOD. Accounting for the duty cycle DOD increased degradation by between 47% and 86%; providing evidence that the DOD is an important factor of degradation.

An analysis of battery degradation on realistic driving behaviour was conducted using four sets of real-world driving data of Nissan Leaf drivers taken from CrossChasm Technologies Inc.'s real-world driving database. The charging time, mean operational SOC, mean DOD, and current demand were used to hypothesize that Driver 1, Driver 3, Driver 2, and Driver 4 would have the highest to lowest degradation over an eight year period. The simulation results on the driver's duty cycles agreed with the hypothesis, producing 5.51%, 5.17%, 4.16%, and 0.75% capacity fade, respectively. Therefore the conclusions made from the sensitivity analysis and the EPA study are applicable for real-world data.

The key finding from this work is that battery degradation depends on the duty cycle. Specifically, the charging time, the operational SOC, the DOD, and the current demand are all factors affecting battery degradation. Ultimately, the battery degradation rate is unique for each driver, depending on those factors.

Acknowledgements

There are so many people to acknowledge; for I would not have completed such an endeavor alone. This thesis has taken time, energy, and sanity away from me, but thanks to the following people and their efforts, I can relax and be happy.

First of all, I would like to acknowledge the most important and influential person in my life; my fiancée, Megan Allen. She has provided constant support and motivation throughout these two years and I could not have completed this thesis without her. However, I would like to thank her most of all for every single moment outside of my thesis; for those moments are the ones I will always remember. You have given me a life full of fun, excitement, happiness, and love.

I would also like to acknowledge Dr. Michael Fowler for playing an important part in my future. Not only has he helped me through the difficult times in my research, but he has been instrumental in my future career at CrossChasm Technologies. Without working in his lab in 2A, him introducing me to UWAFT during my BASc, and a brilliant recommendation for a co-op position, I would not be working at CrossChasm come September.

A special thank you to the following people for their help on my thesis: Mohammad Farkhondeh for his help fitting my battery degradation model; Mohammad Safari for his discussions and ideas at the early stages of my studies; Irene Lau for running the hybrid test bench, and alerting me of all the errors it's produced; Satyam Panchal for showing me how to run the original hybrid test bench and coming in to trouble shoot the system when things weren't working; John Huh who also helped run my degradation cycling; Manoj Matthews who valiantly attempted to fit my model parameters using his statistical magic; and William Scott for all of the discussions and puns in the office.

I would like to thank Matt Stevens and Chris Mendes for sponsoring my research with NSERC; Jen Bauman for keeping me sane by always having work for me to do in the office that *wasn't* my thesis; and Spenser Emery for satisfying all of my IT needs, and I had several.

Finally, I would like to acknowledge and thank my parents, Lynda and Dave, and my siblings, Dan and Melissa, for their constant support. My accomplishments are also my parent's, for they raised me to be a smart, curious, and driven man; all of which I have needed to succeed in life thus far. To the Allen family: Mr. Dad, Mrs. Mom, and Kaity; thank you for allowing me to blitz the end of my thesis at your house. Last but not least, I would like to thank my cat, Rory, for being adorable.

Dedication

To all who read this,

and find it interesting or useful.

Table of Contents

List of Figures

List of Tables

List of Abbreviations

ANN	*Artificial Neural Network*
BEV	*Battery Electric Vehicle*
BOL	*Beginning of Life*
CAFE	*Corporate Average Fuel Economy*
CAN	*Controller Area Network*
CC	*Constant Current*
CCCV	*Constant Current Constant Voltage*
DEC	*Diethyl Carbonate*
DMC	*Dimethyl Carbonate*
DOD	*Depth of Discharge*
EA	*Ethyl Acetate*
EC	*Ethylene Carbonate*
EIS	*Electrochemical Impedance Spectroscopy*
EMC	*Ethyl Methyl Carbonate*
EOL	*End of Life*
EOA	*Environmental Protection Agency*
ESS	*Energy Storage Systems*
GHG	*Greenhouse Gas*
GUI	*Graphical User Interface*
HEV	*Hybrid Electric Vehicle*
HPPC	*Hybrid Power Pulse Characterization*
HTB	*Hybrid Test Bench*
HWFET	*Highway Fuel Economy Test*
LCO	*Lithium Cobalt Oxide*
LFP	*Lithium Iron Phosphate*
LiB	*Lithium Ion Battery*
LMO	*Lithium Manganese Oxide*
LUT	*Look Up Table*
MA	*Methyl Acetate*
MBD	*Model Based Design*
MCMB	*Mesocarbon Microbeads*
MPC	*Methyl Propyl Carbonate*
MPG_e	*Mile Per Gallon Equivalent*
NCA	*Nickel Cobalt Aluminum*
NMC	*Nickel Manganese Cobalt*
OBD	*On Board Diagnosis*
OCP	*Open Circuit Potential*
OEM	*Original Equipment Manufacturers*
P2D	*Pseudo Two Dimensional*
PC	*Propylene Carbonate*
PHEV	*Plug-in Hybrid Electric Vehicle*
PM	*Palmgren Miner*
RC	*Resistor Capacitor*
RPT	*Reference Performance Test*
SEI	*Solid Electrolyte Interface*
SOC	*State of Charge*
SOH	*State of Health*
SP	*Single Particle*
UDDS	*Urban Dynamometer Driving Schedule*
USABC	*United States Advanced Battery Consortium*
UWAFT	*University of Waterloo Alternative Fuels Team*
VSSD	*Variable Solid State Diffusivity*

Nomenclature

I	Current, A	t	Time, s
N_c	Number of coulombs, C	Q	Capacity, Ah
SOC_0	Initial SOC, %	Q_{max}	Maximum battery capacity, Ah
t_0	Initial time, s	ε_c	Coulombic efficiency, %
Q_{dis}	Discharged capacity, Ah	Q_{chg}	Charged capacity, Ah
R_{int}	Internal resistance, ohm	V_0	Initial voltage, V
I_0	Initial current, A	V_{10}	Voltage at 10 s, V
I_{10}	Current at 10 s, A	c/d	Charge or discharge
U	Open circuit potential, V	N	Number of events of type i
i	Type of load events	Δt_i	Duration of event i, s
t_i^f	Time until the EOL, s	D_a	Total accumulated damage, Ah
S_i	Stress magnitude of event i	N_e	Number of events in a periodic motif
Δt_m	Duration of the periodic motif, s	F_{comb}	EPA combined fuel economy, MPG
F_{city}	EPA city fuel economy, MPG	F_{hwy}	EPA highway fuel economy, MPG
D_{trip}	Trip distance, miles	E	Trip energy consumption, kWh
τ	Electrical energy to fuel volume conversion constant, [334 kWh gal^{-1}]	σ	ΔSOC correction, kWh
V_{nom}	Nominal pack voltage, V	N_{ser}	Number of cells in series
N_{par}	Number of cells in parallel	ΔSOC	Change in SOC
V_{cell}	Cell potential, V	V_{LFP}	LFP electrode potential, V
V_G	Graphite electrode potential, V	n/p	Negative or positive electrode
$i_{n/p}^{int}$	Intercalation current density, A m^{-2}	F	Faraday's constant, [96587 C mol^{-1}]
$k_{n/p}^0$	Intercalation reaction rate constant, $m^{2.5}$ $mol^{-0.5}$ s^{-1}	c_e	Electrolyte concentration, mol m^{-3}
$c_{n/p}^{max}$	Maximum lithium concentration, mol m^{-3}	x_s	Dimensionless solid-state lithium concentration on graphite particle surface
y_s	Dimensionless solid-state lithium concentration on the LFP particle surface	β	Charge-transfer coefficient

R	Gas constant, [8.314 J mol^{-1} K^{-1}]	T	Absolute temperature, K
$\eta_{n/p}$	Surface overpotential, V	Φ_n	Solid-phase potential, V
R_{SEI}	SEI film resistance, ohm m^2	i_n^t	Total current density of the negative electrode, A m^{-2}
R_p	Reactive resistance of the LFP particles, ohm m^2	i_s	Parasitic current density, A m^{-2}
k_{fs}^{app}	Apparent rate constant of the side reaction, mol m^{-2} s^{-1}	δ_{SEI}	SEI film thickness, m
V_{SEI}	Molar volume of the SEI film, m^3 mol^{-1}	R_{SEI}^0	Initial SEI film resistance, ohm m^2
κ_{SEI}	Ionic conductivity of the SEI film, S m^{-1}	$L_{n/p}$	Electrode thickness, m
$a_{n/p}$	Specific interfacial area per unit volume of electrode, m^{-1}	$\bar{x}$	Dimensionless mean solid-state lithium concentration inside the graphite particles
$\bar{y}$	Dimensionless mean solid-state lithium concentration inside the LFP particles	$r_{n/p}$	Particle radius, m
$A_{n/p}$	Electrode surface area, m^2	$\varepsilon_{n/p}$	Electrode active material volume fraction
$\bar{q}_{n/p}$	Dimensionless volume-averaged flux of lithium concentration in the particles	$D_{n/p}$	Solid-state lithium diffusion coefficient in the particle, m^2 s^{-1}
D_p^0	Solid-state diffusion coefficient at a completely delithiated state of the LFP particle, m^2 s^{-1}		

Chapter 1
Introduction

Lithium ion batteries (LiBs) have led to significant advancements in electric vehicle development due to their high energy and power densities and long life. They have been used to develop hybrid electric vehicles (HEV), plug-in hybrid electric vehicles (PHEV), and battery electric vehicles (BEV). Batteries offer vehicle manufactures a cost-effective option for reducing fuel consumption and emissions levels of their product lines to satisfy the new Corporate Average Fuel Economy (CAFE) standards introduced by the US government. CAFE standards require vehicle manufacturers to improve the overall fuel economy of their light duty vehicles sold in a given year from 32.2 MPG in 2014 to 54.5 MPG by 2025 (Figure 1.1) [1]. Customers benefit from such an improvement by spending less on fuel, and society benefits through improved urban air quality and reduced energy exploration and consumption. However, before a CAFE standard of 54.5 MPG can be feasibly achieved there must be significant improvements in battery technology.

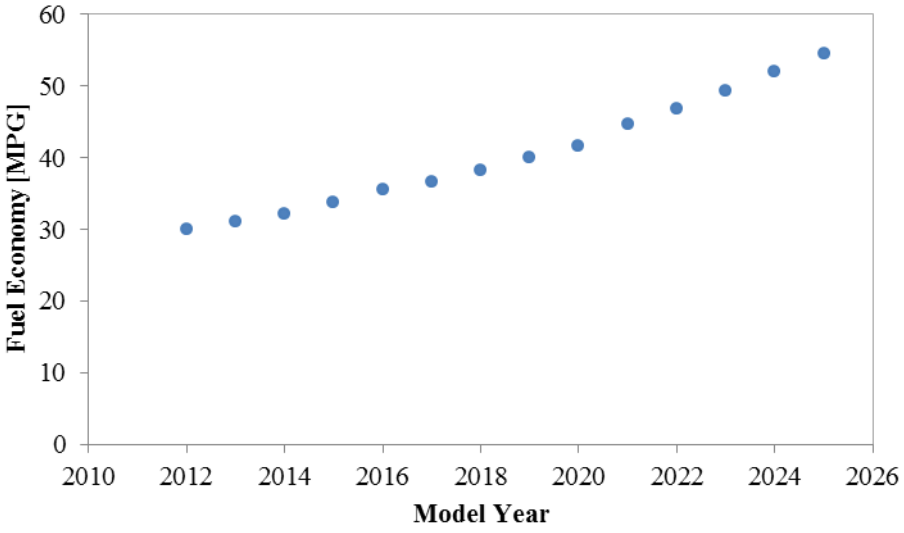

Figure 1.1 CAFE standards for light-duty vehicles [1]

Battery pack sizing is a facet of vehicle design currently understudied and thus has a high potential for improvement. The complexity of battery pack design is a result of considering mass, volume, and cost restrictions while attempting to maintain a sufficient electric range. A 2009 study by Shiau *et al.* revealed that as the all-electric range of a vehicle increased, the charge depletion and charge sustaining mode efficiencies decreased and the vehicle mass, operational cost, and operational

greenhouse gas (GHG) emissions increased (Figure 1.2) [2]. Therefore, it is important to correctly size the battery pack to avoid such negative effects on performance.

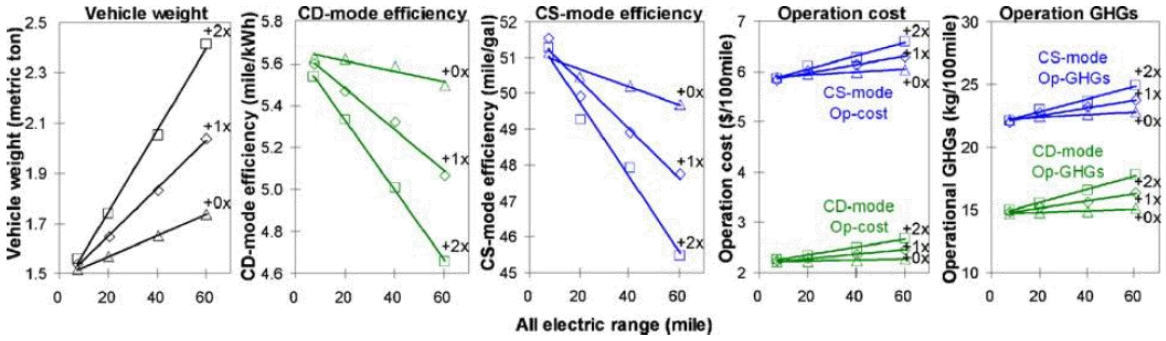

Figure 1.2 Effects of increasing the all-electric range of a PHEV on vehicle mass, efficiencies, costs, and GHG emissions [2]

Considering that the efficiencies, costs, and GHG emissions increase with battery pack size; it would make sense to select a smaller pack. However, as the vehicle usage increases and the battery pack begins to age, the all-electric range will begin to diminish. Shiau *et al.* do not consider degradation when analyzing the aforementioned results [2]. Degradation is often neglected or simplified during battery pack design. The United States Advanced Battery Consortium (USABC) declared that a battery has reached its end-of-life (EOL) if the battery capacity delivered to the powertrain is less than 80% of the rated capacity, or if the battery's peak power is less than 80% of the rated power at 80% depth-of-discharge (DOD) [3, 4]. Thus it is typically assumed that a battery will degrade 20% over the life of the vehicle, but making this assumption leads to oversized battery packs in an attempt to account degradation (Figure 1.3). One issue with assuming 20% capacity fade over the life of a vehicle is that it does not consider each driver to be unique. The aggressiveness of the driver behaviour will result in differing operational histories on the battery pack, and thus different amounts of degradation. More precise battery pack design can be achieved through an understanding of how the battery degrades over the vehicle lifetime. Battery lifetime can be assessed through experimentation, simulation, or some combination of the two methodologies.

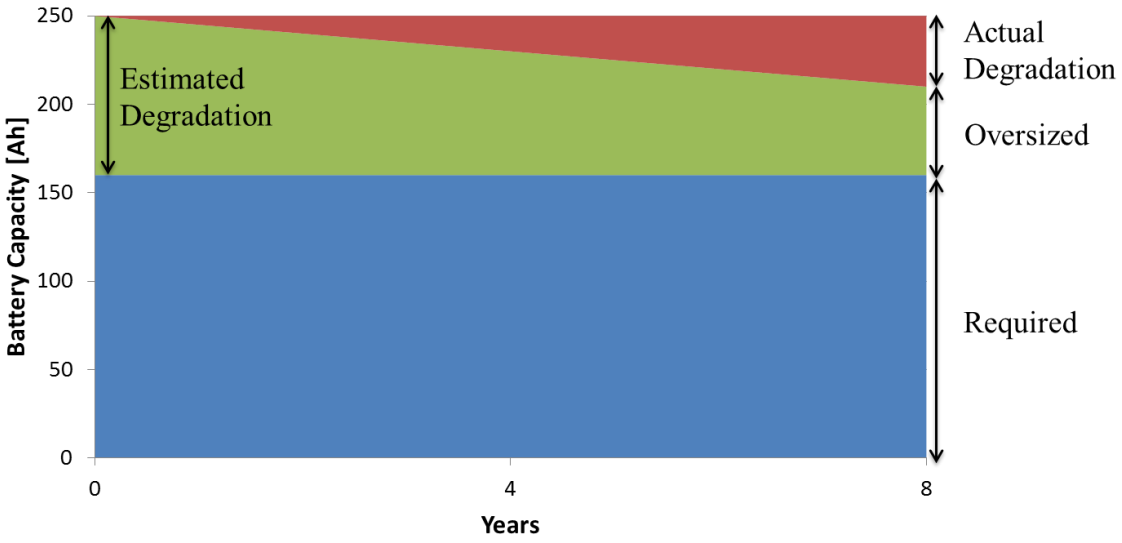

Figure 1.3 Battery pack oversizing due to unknown battery degradation for an 8 year lifetime

One method of lifetime assessment measures real-time battery degradation of a battery pack installed on a vehicle during driving events. While this test shows real-world battery degradation, it requires a working prototype of the vehicle, and a long testing period requiring up to eight years of driving. Additionally, this test does not consider that many drivers have different driving behaviours that will degrade the battery pack at different rates. It is assumed that different driving behaviours do significantly affect battery degradation because of the clear effect on fuel economy (Figure 1.4) and thus power usage; which is directly related to battery usage [5]. FleetCarma, a division of CrossChasm Technologies Inc., uses an Eco-Score as a metric for assessing driving behaviour. A low Eco-Score represents aggressive driving, and a high Eco-Score represents eco-driving. The assumption that degradation will depend upon driving behaviours will be investigated further throughout this work.

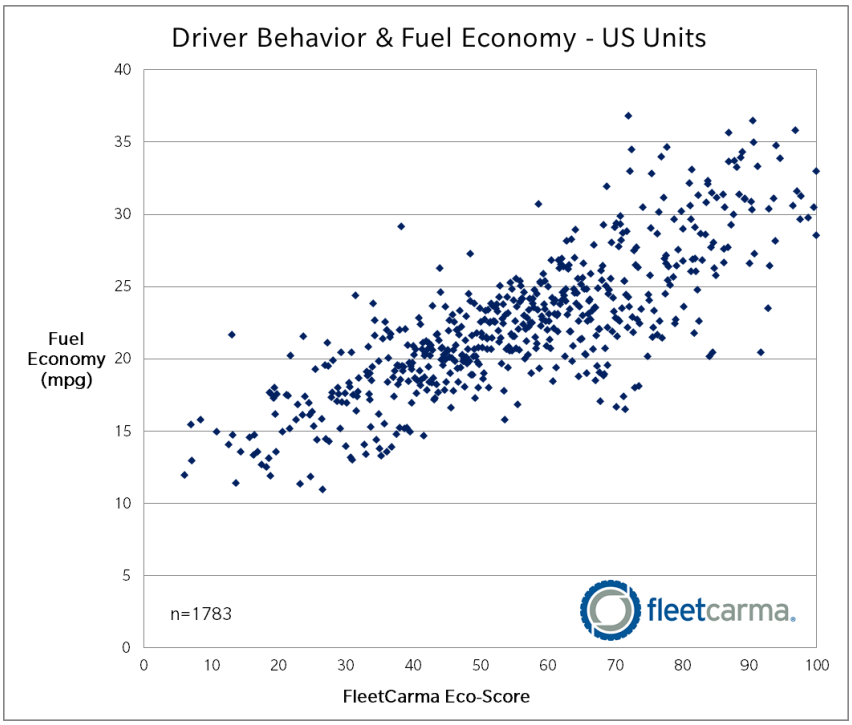

Figure 1.4 Driver behaviour effects on fuel economy, where better driving patterns are represented by a higher Eco-Score [5]

Another lifetime assessment method involves testing the battery pack or its constituents in the laboratory. Testing the individual batteries reduces costs since a pack does not need to be designed yet, a vehicle prototype does not have to be built, and the equipment used to test the battery is less expensive compared to equipment to test a high-voltage pack. Additionally, accelerated degradation test methods exist to reduce the test period. These methods include extreme temperatures, loads (*e.g.*, charge rates), or deep charging and discharging. This method is typically limited to galvanostatic cycling, single temperature testing, or fixed depth-of-discharge; reducing the applicability of the results. To include more complexities in operating conditions would dramatically increase the test periods.

The most fundamental assessment method, and the one used herein, is to develop a physics-based electrochemical model of the battery from experimental data. Limited battery testing is conducted to fit the model parameters to the data. After the model is validated, simulations on various load profiles can be run to predict battery performance and degradation. Integrating the battery degradation model into a vehicle model enables prediction of battery performance and degradation on any drive cycle. In

other words, battery performance and degradation over its lifetime can be determined for various drivers and their personal driving behaviours. However, such fundamental modeling entails a detailed understanding of all the reaction kinetics, including side reactions, and material degradation mechanisms. Such an understanding will take several years and extensive research efforts. The results of this work, and others like it, contribute to that understanding.

To demonstrate such an analysis in this work, an A123 AMP20 pouch battery of $LiFePO_4$ chemistry will be tested, modeled, and simulated to predict lifetime performance and degradation according to various Environmental Protection Agency (EPA) drive cycles as well as real-world drive cycles located in CrossChasm's real-world driving database. The primary factors affecting battery degradation will be discovered and analyzed to generate control strategies or preventative measures that reduce battery pack degradation on board vehicles.

Chapter 2
Lithium Ion Batteries

2.1 Battery Types

A battery is an electrochemical device that provides electrical energy from stored chemical energy. Batteries can be categorized into primary batteries, secondary batteries, and flow batteries. Primary batteries are constructed with high energy densities, and once discharged, are incapable of being recharged. Thus, primary batteries can only be discharged once. Secondary batteries are can be constructed with high energy density, high power density, or some compromise between the two. Once discharged, secondary batteries are capable of recharging by connecting a power supply to the battery instead of a load. Finally, a flow battery stores chemical energy outside of the battery in the form of a fluid. The fluid is passed through the battery, reacting electrochemically to produce electrical energy. Flow batteries can act as primary batteries, where the fluid acts as a fuel that is spent in the production of electrical energy, or as secondary batteries, where the electrochemical process can be reversed to store energy in the fluid once again. It is necessary to understand how these batteries work to determine their applicability to the automotive industry.

The automotive industry has been shifting towards battery technology, using secondary batteries as energy storage systems (ESSs) on-board their vehicles. Batteries are useful for vehicle applications because they are portable ESSs that can store and provide large quantities of energy and power to the powertrain. Since primary batteries are limited to single discharge applications, they are excluded from vehicle designs. Most flow batteries are better suited for large, stationary ESSs, such as wind or solar energy storage. One exception is the zinc-air battery that has begun to show promise for vehicle applications since the fluid (*i.e.*, air) is readily available around the vehicle. However, zinc-air batteries are still a young technology and are ultimately excluded from current vehicle designs. Secondary batteries are the best choice for vehicle applications because of their rechargeable design, high energy and power densities, and the level of knowledge and experience surrounding their use.

2.2 Secondary Battery Components

Secondary batteries are constructed from four primary components that work together to satisfy their performance requirements (Figure 2.1). In the simplified version of a secondary battery, two charged electrodes and a membrane separator are submerged in an electrolyte. While the battery is discharged,

the negative electrode (*i.e.*, anode) is oxidized in the presence of the electrolyte and provides electrons to an external circuit to power a load. The electrons leaving the load are accepted by the positive electrode (*i.e.*, cathode) as it is reduced in the presence of the electrolyte. The electrochemical reactions on the electrode surfaces can be reversed by providing power to the battery instead of removing it. The electrolyte acts as the medium for charge transport via ions between the two electrodes; thus completing the circuit. To prevent electron transfer between the two electrodes through the electrolyte, and effectively short circuiting the battery, the electrolyte must be electrically resistant. Additionally, the separator is designed to offer a mechanical barrier between the electrodes while remaining permeable to the electrolyte and its ions.

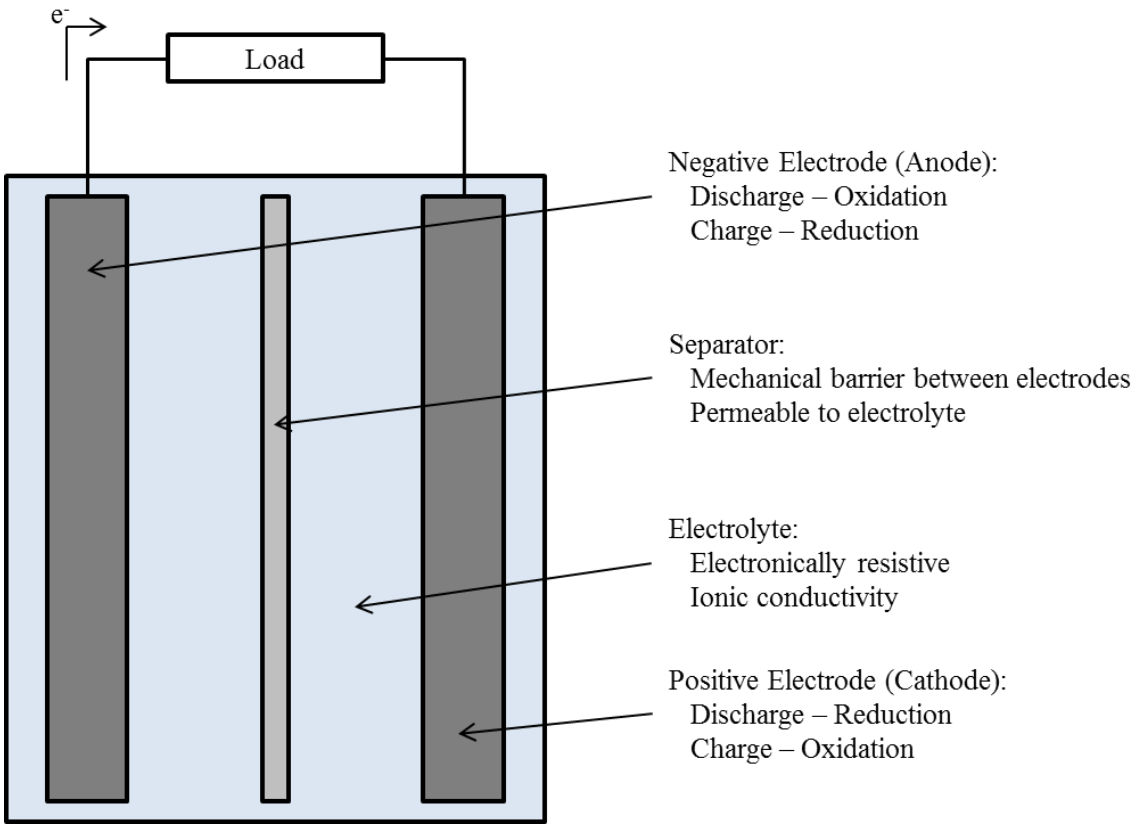

Figure 2.1 Simple representation of a secondary battery during a discharge event

It is important to note that upon charging, the negative electrode becomes the cathode while the positive electrode becomes the anode. Therefore, the terms ‘anode’ and ‘cathode’ will no longer be used to describe the charge of the electrodes.

2.3 Lithium Ion Battery Operation

There are several options of build materials available when designing a battery. For secondary batteries, the chemistry of the components can vary widely. However, lithium ion batteries represent the most viable option for power and energy requirements according to current vehicle technology (Figure 2.2). Therefore, only LiBs are considered.

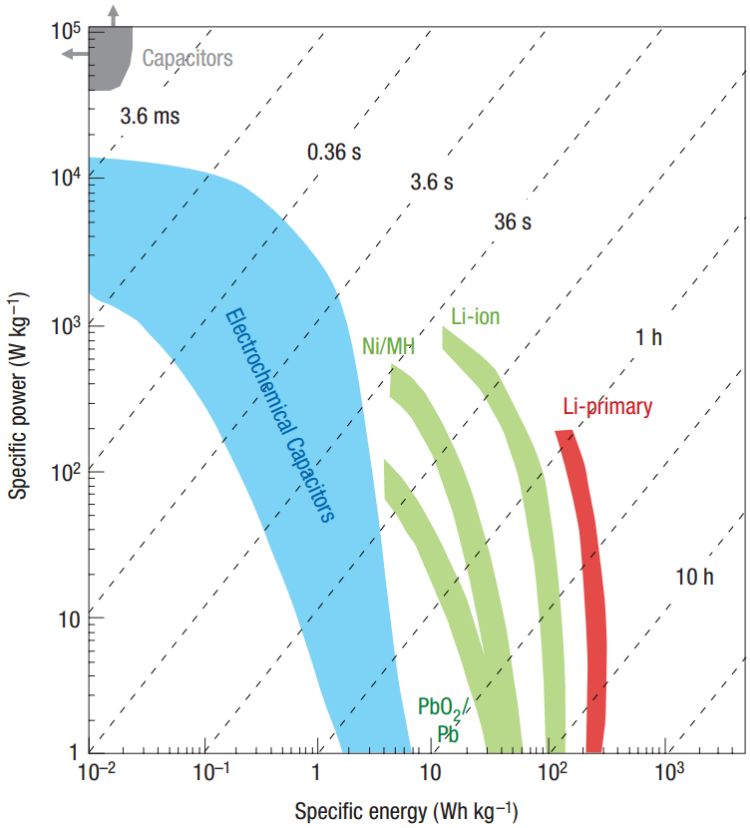

Figure 2.2 Ragone plot of various ESSs with time constants obtained through the division of energy density with power density [6]

In general, lithium ion batteries depend on the transport of lithium ions between the electrodes for successful operation (Figure 2.3). In a balanced cell, without excess lithium present, the positive current collector is coated with a lithium metal oxide ($Li_{1-x}MO_2$) and the remaining lithium in the cell is situated between the layers of graphite (Li_xC) coated onto the negative current collector.

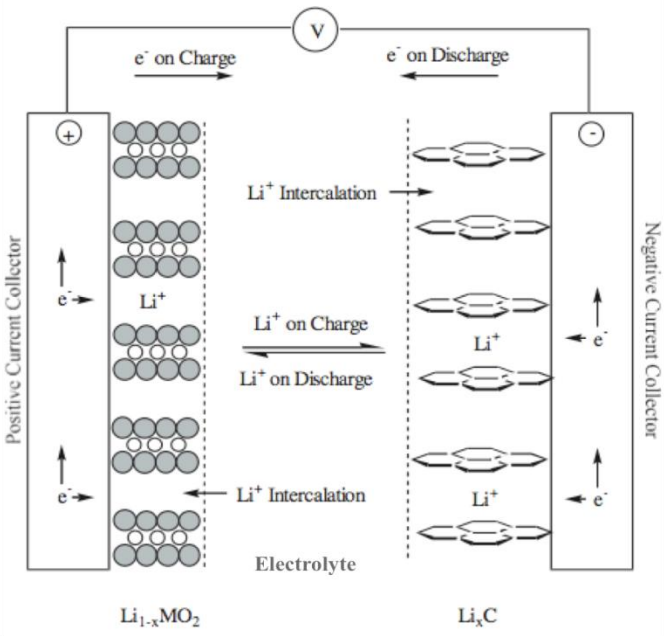

Figure 2.3 Operational schematic of a lithium ion battery [7]

During discharging, the lithium ions deintercalate from the negative electrode providing free electrons to power a load.

$$Li_xC \rightarrow C + xLi^+ + xe^- \tag{2.1}$$

The lithium ions are transported through the electrolyte to meet the electrons at the positive electrode and intercalate into the metal oxide active material.

$$Li_{1-x}MO_2 + xLi^+ + xe^- \rightarrow Li_xMO_2 \tag{2.2}$$

2.4 Secondary Battery Chemistries

After narrowing the general battery chemistry to lithium ion technology, there are several variants of LiBs. The component materials are selected to optimize the performance of the LiB, so different manufactures focus on different materials.

For the negative electrode, most manufacturers use a carbon-based active material bound to a copper current collector (Table 2.1). The current collector offers a structure to the active material layer and accumulates or disperses electrons evenly across the active material during use. Ideally, a

negative electrode active material is selected to maximize specific capacity while minimizing irreversible capacity [8]. Mesocarbon microbeads (MCMB) are a common selection.

Table 2.1 Properties of various carbon-based active materials [8]

Carbon	Type	Specific Capacity (mAh g^{-1})	Irreversible Capacity (mAh g^{-1})	Particle Size D_{50} (µm)	BET Surface Area (m^2 g^{-1})
KS6	Synthetic Graphite	316	60	6	22
KS15	Synthetic Graphite	350	190	15	14
KS44	Synthetic Graphite	345	45	44	10
MCMB 25-28	Graphite Sphere	305	19	26	0.86
MCMB 10-28	Graphite Sphere	290	30	10	2.64
Sterling 2700	Graphitized Carbon Black	200	152	0.075	30
XP30	Petroleum Coke	220	55	45	N/A
Repsol LQNC	Needle Coke	234	104	45	6.7
Grasker	Carbon Fiber	363	35	23	11
Sugar Carbon	Hard Carbon	575	215	N/A	40

The positive electrode is composed of a lithium metal oxide active material, bound to an aluminum current collector. The choice of metal(s) in the active material is typically synonymous with the battery chemistry. Chikkannanavar *et al.* recently reviewed these options and presented their performance capabilities (Table 2.2) [9]. From this list of materials, the LCO, NCA, LMO, NMC, and LFP are the most popular choices, but as is evident, there are many various blends capable of producing better performance results.

Table 2.2 Properties of various lithium metal oxide active materials [9]

Active Material	Capacity ($mAh\ g^{-1}$)	Average Voltage (V vs Li/Li^+)	Energy Density ($Wh\ kg^{-1}$)	Energy Density ($Wh\ L^{-1}$)
$LiCoO_2$ (LCO)	151	4.00	602	3073
$LiNi_{0.8}Co_{0.15}Al_{0.05}O_2$ (NCA)	195	3.80	742	3784
$LiMn_2O_4$ (LMO Spinel)	119	4.05	480	2065
$LiNi_{1/3}Mn_{1/3}Co_{1/3}O_2$ (NMC 333)	153	3.85	588	2912
$LiMn_xCo_yNi_zO_2$ (NMC non-stoichiometric)	220	4.0	720	3600
$LiFePO_4$ (LFP)	161	3.40	549	1976
$xLi_2MnO_3{\cdot}(1\text{-}x)LiMO_2$	250-280	~4.0	-	-
$LiCoO_2 – LiNi_{1/3}Mn_{1/3}Co_{1/3}O_2$ (7:3)	180	~3.9	-	-
$xLi_2MnO_3{\cdot}(1\text{-}x)LiMO_2 – LiFePO_4$	220	~3.6	>890	-
$Li[Li_{0.2}Mn_{0.54}Ni_{0.13}Co_{0.13}]O_2 – LiV_3O_8$	275	3.0-4.0	-	-
$Li[Li_{0.2}Mn_{0.54}Ni_{0.13}Co_{0.13}]O_2 – Li_4Mn_5O_{12}$	250	3.0-4.0	-	-
$Li[Li_{0.17}Mn_{0.58}Ni_{0.25}]O_2 – LiFePO_4$	~200	3.0-4.0	>700	-
Sulfur (in Li-sulfur system)	~1000	2.0-2.4	1550	-

With respect to the electrolyte, there are four forms in which it can be incorporated into the battery. The first form is as a liquid solution of lithium salt in an organic solvent. Liquid electrolytes are beneficial since they are absorbed by the separator and immerse the electrodes [8]. The second form is a high molecular weight polymer with the lithium salt dissolved into it. Polymer electrolytes are beneficial due to their safety from the lack of a volatile component [8]. The third form is a gel, where the liquid electrolyte is dissolved or mixed with a polymer. Gel electrolytes are beneficial since the higher viscosity lowers the change of a leakage compared to the liquid electrolyte [8]. The fourth

form is a ceramic electrolyte composed of inorganic, solid-state materials [8]. Ceramic electrolytes are not commonly used in vehicle applications.

Important aspects of an electrolyte are its ionic conductivity and its compatibility with the other components in the battery [8]. The salts commonly used in the electrolytes are presented in Table 2.3, where the most common is $LiPF_6$.

Table 2.3 Lithium salts used in the electrolyte [8]

Common Name	Formula	Molecular Weight (g mol^{-1})	Typical Impurities	Comments
Lithium hexafluorophosphate	$LiPF_6$	151.9	H_2O (15 ppm) HF (100 ppm)	Most commonly used
Lithium tetrafluoroborate	$LiBF_4$	93.74	H_2O (15 ppm) HF (75 ppm)	Less hygroscopic than $LiPF_6$
Lithium perchlorate	$LiClO_4$	106.39	H_2O (15 ppm) HF (75 ppm)	When dry, less stable than alternatives
Lithium hexafluoroarsenate	$LiAsF_6$	195.85	H_2O (75 ppm) HF (15 ppm)	Contains arsenic
Lithium triflate	$LiSO_3CF_3$	156.01	H_2O (100 ppm)	Al corrosion above 2.8 V, stable to water
Lithium bisperflurorethane-sulfonimide	$LiN(SO_2C_2F_5)_2$	287	N/A	No Al corrosion below 4.4 V, stable to water

Furthermore, the available solvents and their mixtures are selected to maximize ionic conductivity of the salts (Figure 2.4). The most common solvents are propylene carbonate (PC), ethylene carbonate (EC), dimethyl carbonate (DMC), diethyl carbonate (DEC), ethyl methyl carbonate (EMC), methyl acetate (MA), methyl propyl carbonate (MPC), and ethyl acetate (EA) [8].

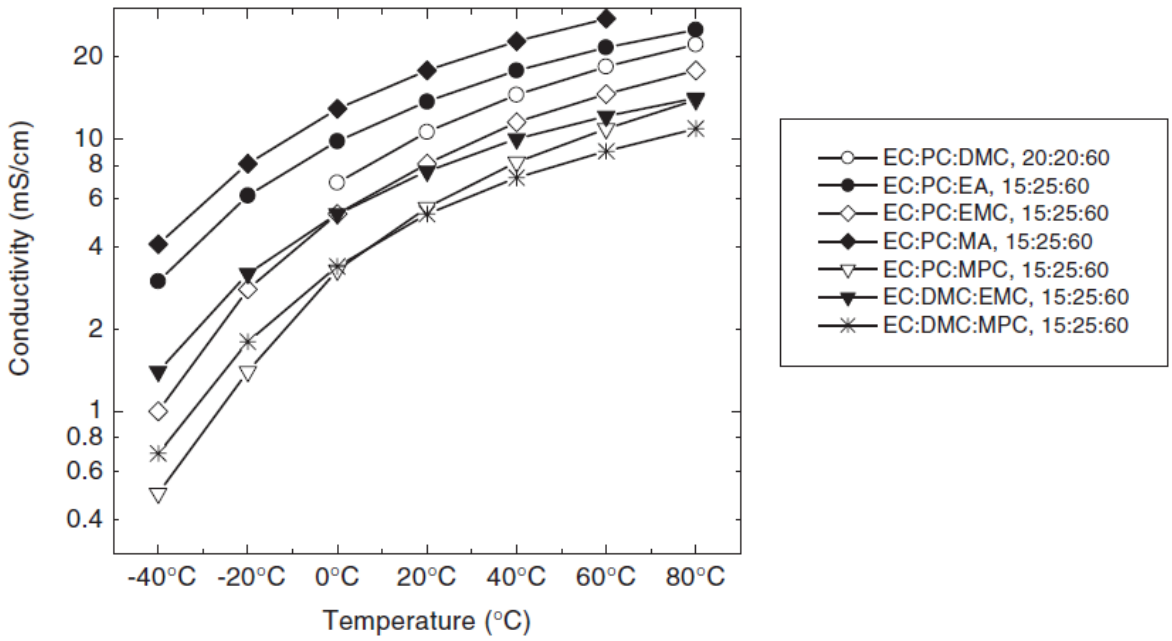

Figure 2.4 Solvent mixture conductivities of 1M $LiPF_6$ [8]

The separator integrated into the battery is often a microporous (0.03 µm to 0.1 µm) film of polyethylene or polypropylene, approximately 10 µm to 30µm thick, which offers electrical resistance to prevent short circuiting the battery [8].

In addition to all of these components, various additives are often found in commercial batteries to improve performance.

2.5 Battery Construction

Once the battery components are selected, they must be packaged into a useful form. There are four types of packing used for lithium ion batteries (Figure 3.2). The cylindrical and prismatic batteries are built from wound electrodes and separators, immersed in electrolyte, containing several electrochemical cells within. The coin battery is a small flat construction containing a single electrochemical cell within it. The pouch battery is also a flat construction but contains several electrochemical cells within it. The cylindrical, prismatic, and pouch packaging are often used in automotive applications due to the large surface areas of the electrodes. The intended operating conditions for the battery determine which packaging is selected by the automotive manufacturer. For

example, the Chevrolet Volt and Nissan Leaf use pouch batteries while the Tesla Model S uses cylindrical batteries.

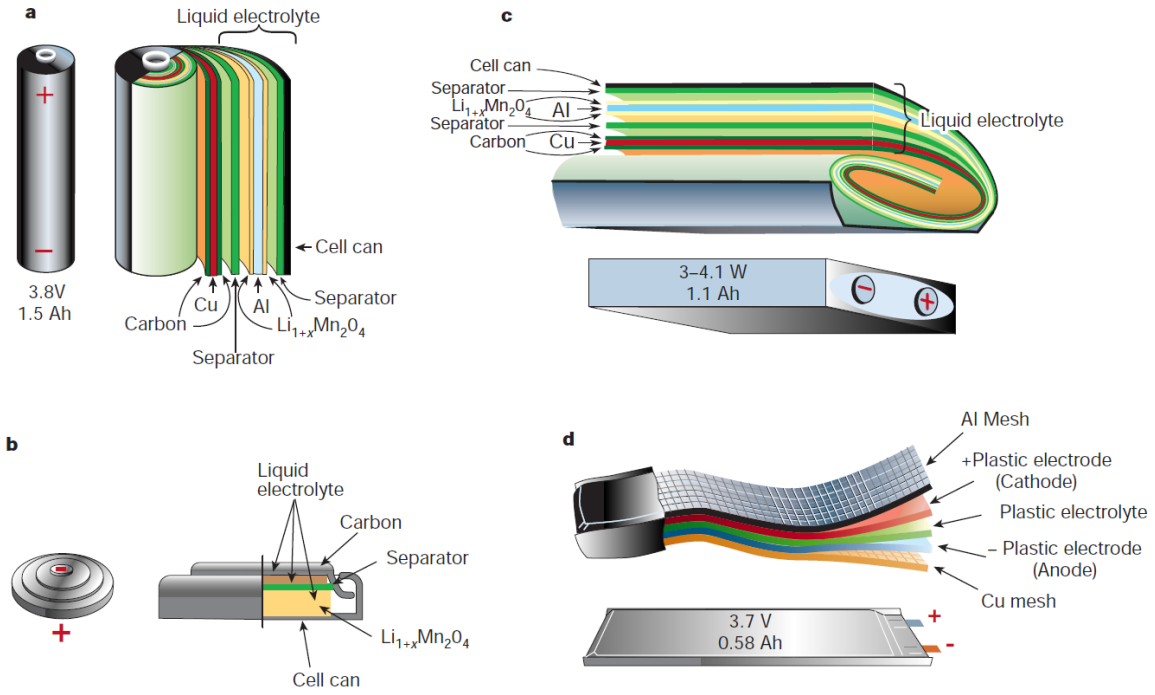

Figure 2.5 (a) Cylindrical, (b) prismatic, (c) coin, and (d) pouch packaging for lithium ion batteries [10]

2.6 Vehicle-Grade Batteries

Vehicle-grade batteries are built to the highest standards in an attempt to provide an optimal mixture of power and energy, and to last between 10-15 years [11]. As with many vehicle components, the battery is not immune to degradation. The battery will age as time and usage progresses. The mechanisms and types of aging can be generalized; however the physics behind those generalizations are specific to the chemistries of the batteries. Since the drivable range of a vehicle is important, how the range changes as a battery degrades is also important. Typically if a battery has lost 20% of its original range, the battery is considered to have reached its EOL. Therefore when designing batteries for vehicle applications, one must consider the performance requirements and their impact on battery degradation. Usually, the battery is oversized to account for unexpected rates of degradation. This identifies the necessity of this work since accurately predicting the battery degradation from performance demands reduces the unexpected rates of degradation. As the

unexpected degradation rates decrease, so too will the size of the battery. Such a reduction in battery size holds significant financial benefits to original equipment manufacturers (OEMs) due to the high cost of the battery with respect to the other components in electric or hybrid powertrains.

Chapter 3
Battery Testing

3.1 Introduction

Batteries must be tested to determine their performance capabilities and lifetime for a given application. Given a fresh cell, characterization tests provide a picture of how well the battery operates in a specified application. Degradation tests stress the battery to generate aging within its components. Typically degradation tests stress the battery more so than the battery might expect in its actual application; however this shortens the testing period. Throughout the battery's lifetime, the characterization tests provide aging information to help monitor its state of health (SOH) until the battery degrades to its EOL. Post-mortem tests are sometimes conducted on a battery after it reaches its EOL to measure physical parameters in an attempt to elucidate the degradation mechanisms behind its aging. This section excludes post-mortem testing procedures as they fall outside the scope of this investigation. While the relevant test procedures are presented below, more detailed procedures are available in the Battery Test Manual for Plug-in Hybrid Electric Vehicles [4].

3.2 State of Charge Estimations

One important metric used to monitor the remaining energy stored within the battery is the battery state of charge (SOC). This metric draws much attention because there is no direct way to measure the SOC; so it must be estimated using other measurements. The most common and simplest SOC estimation method is based on the notion that one can count the coulombs entering and leaving the battery. Since current, I, can be expressed in coulombs per second, the integration of that current with respect to time, t, provides the total number of coulombs, N_c, transported into or out of the battery.

$$N_c = \int_{t_0}^{t} I dt \tag{3.1}$$

The total number of coulombs can be expressed as a capacity, Q, following a simple unit conversion.

$$Q = \int_{t_0}^{t} \frac{I}{3600} dt \tag{3.2}$$

Thus SOC can be estimated by considering the initial SOC, SOC_0, as well as the capacity processed during usage as a percentage of the maximum battery capacity, Q_{max}.

$$SOC = SOC_0 - \frac{Q}{Q_{max}} * 100\% \tag{3.3}$$

However, the limitation of this method is that it requires the initial SOC of the time period; which may be unavailable. Fortunately, current levels of vehicle technology, memory, and processing power make this form of SOC estimation an appropriate choice.

Some modifications can be applied to this SOC estimation method to account for a changing maximum battery capacity or limitations restricting the SOC from operating between 0% and 100% [12]. The maximum battery capacity could change according to battery temperature or battery degradation via capacity fade. Power fade could prevent a battery from fully charging or discharging, altering the SOC operating window. Battery SOC estimation is a useful way to normalize the characterization results to effectively compare battery performances for various conditions and lifetimes.

In vehicle applications, many automotive manufacturers will prevent the user from accessing the full battery energy. For example, the 2011 Volt contains a 16 kWh battery but only makes 10.4 kWh available to the user and still reports SOC between 0% and 100%. In this case, the Volt is reporting the useable SOC instead of the actual SOC. Herein, only actual SOC will be reported.

3.3 C-Rate

It is common to present the battery current as a normalized value with respect to the battery capacity. For example, a 1C discharge of a 20 Ah battery represents 20 A and will discharge the battery in an hour.

$$C - rate = \frac{I}{Q_{max}} \tag{3.4}$$

3.4 Maximum Capacity

The maximum capacity is often determined similarly across all battery testing procedures, and is presented below (Figure 3.1).

- The battery is charged according to the recommended charging procedure from the battery manufacturer or according to its application.
    - Typically, the charging procedure consists of a constant-current (CC) charge, until the upper voltage limit is reached, at which point the voltage is held constant until the lower current limit is reached. Such a procedure is called constant-current constant-voltage (CCCV) charging.
- A resting period allows the battery to reach a state of equilibrium before the test continues. A common resting period is defined either by time (*e.g.,* 1 hour) or by a lack of change in the measured open circuit potential (OCP).
- The battery is discharged under CC conditions at a current specified by the manufacturer or by the application. The CC discharge occurs until a cut-off potential is reached.
- A resting period similar to the previous one is used to allow the battery to reach equilibrium before further testing is conducted.

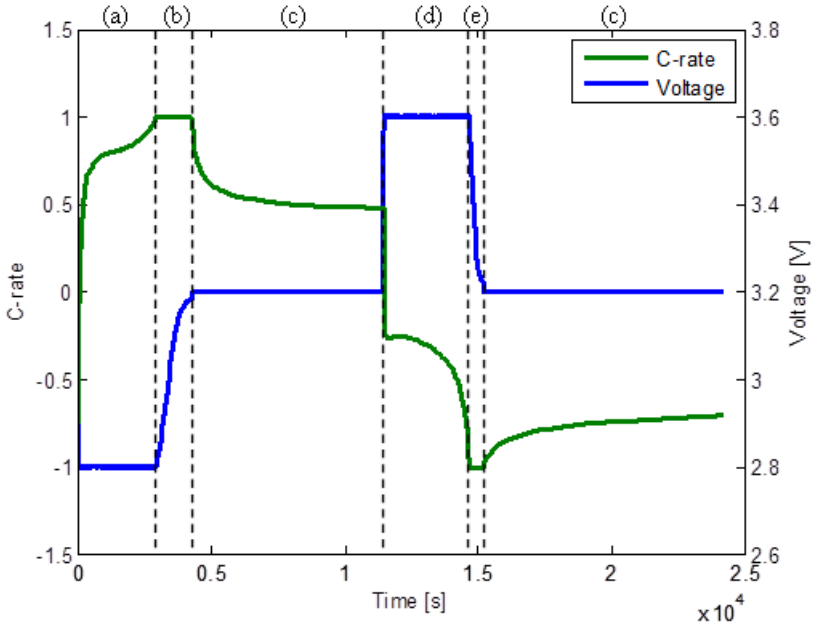

Figure 3.1 (a) CC charge, (b) CV charge, (c) rest, (d) CC discharge, and (e) CV discharge profiles for the maximum capacity test

The maximum capacity for charge or discharge conditions can be calculated from the current flow out of the cell over the duration of the CCCV charge or discharge.

$$Q_{max} = \int_{t_0}^{t} \frac{Idt}{3600} \tag{3.5}$$

This process can be repeated until a maximum capacity can be confidently determined; however it is best to reduce the number of tests to limit degradation.

It is important to understand that the maximum capacity depends on the C-rate as well as the battery temperature during testing (Figure 3.2). However, batteries in this work are tested at room temperature.

(a) (b)

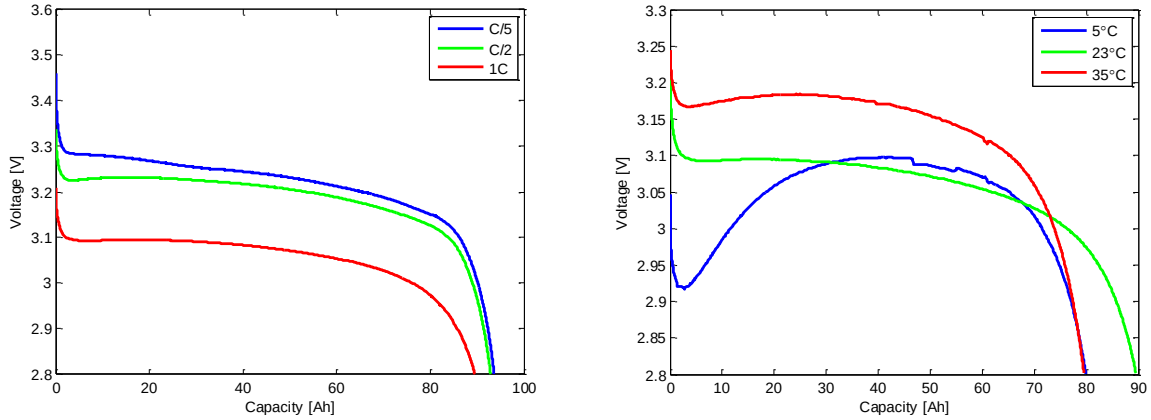

Figure 3.2 Effect of (a) C-rate at 23°C, and (b) battery temperature at 1C discharge, on maximum capacity

3.5 Coulombic Efficiency

The coulombic efficiency testing investigates the battery's capability to receive and produce an equivalent amount of capacity for a given current. Unfortunately, the transport of lithium ions throughout the cell is not completely reversible. There are irreversible side reactions that occur primarily at the graphite-electrolyte interface that reduce the cycleable lithium ions in the cell. Therefore, charging a cell will result in the consumption of a small amount of lithium ions and prevents them from cycling back to the cathode during a discharge. The loss in lithium ions is

represented by the coulombic efficiency, ε_c, according to the difference between the discharged capacity, Q_{dis}, and charged capacity, Q_{chg}, in the relationship below.

$$\varepsilon_c = \frac{Q_{dis}}{Q_{chg}} * 100\% \tag{3.6}$$

The test procedure for determining the coulombic efficiency is presented below (Figure 3.3).

- The battery is charged according to the standard procedure determined best for the battery.
- The battery is discharged under CC conditions at the standard C-rate until the upper potential limit is reached.
- A resting period brings the battery to a state of equilibrium before testing begins.
- The battery undergoes a CC discharge to the lower potential limit.
- A resting period brings the battery to a state of equilibrium before testing continues.
- A CC charge is applied to the battery until an upper potential limit is reached.
- A resting period brings the battery to a state of equilibrium before testing continues.

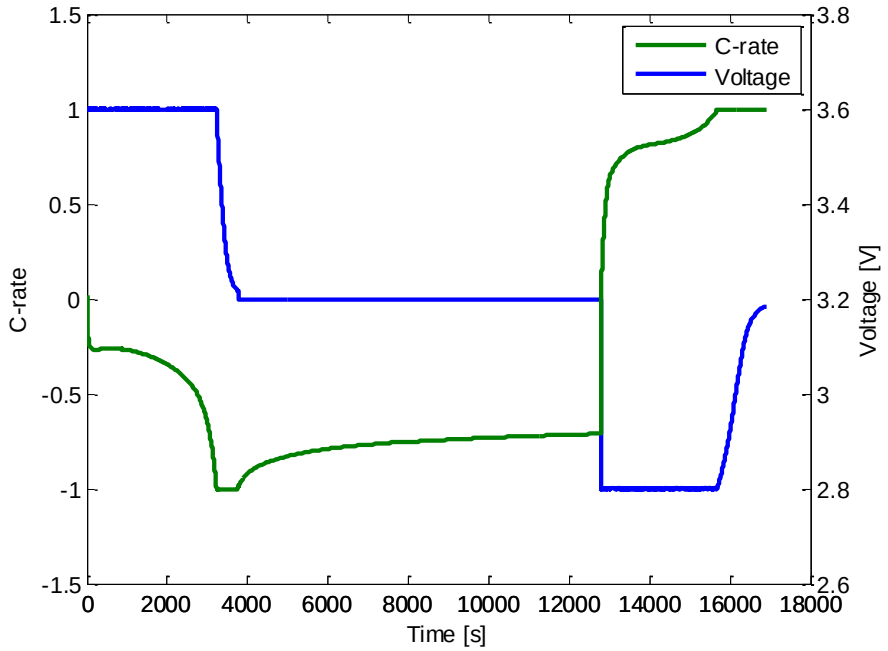

Figure 3.3 Coulombic efficiency test procedure for a 0-100% SOC operating window and 2 hour rest

The coulombic efficiency is typically dependent upon the battery temperature. Therefore the test procedure can be conducted at various temperatures that the battery is expected to perform in, according to its application.

3.6 Open Circuit Potential (OCP)

The battery OCP is often determined by measuring the voltage of a battery while at its equilibrium state for various SOC operating points. To do so, the following test procedure should be conducted.

- The battery is charged according to the standard charging procedure.
- The battery rests for a specified time period or until the rate of change of potential is acceptably low; at which point the OCP is recorded.
- The battery is discharged according to the standard discharging procedure until the new SOC operating point is reached.

- The rest, measurement, and discharge steps are repeated until all of the SOC operating points have been tested.

Although this is the most accurate way of measuring the OCP of a battery, it may not be the most detailed since it depends on the resolution of the SOC operating points selected. Therefore more SOC points are required to get a detailed OCP profile, which requires more resting periods; extending the test procedure duration. To combat this, it is proposed that the OCP profile is a mean between the voltage responses for a C/25 charge and discharge rate (Figure 3.4) [13]. By making the assumption that C/25 approximates the open-circuit condition, it allows for a high resolution OCP profile to be developed for a 0-100% SOC operating window.

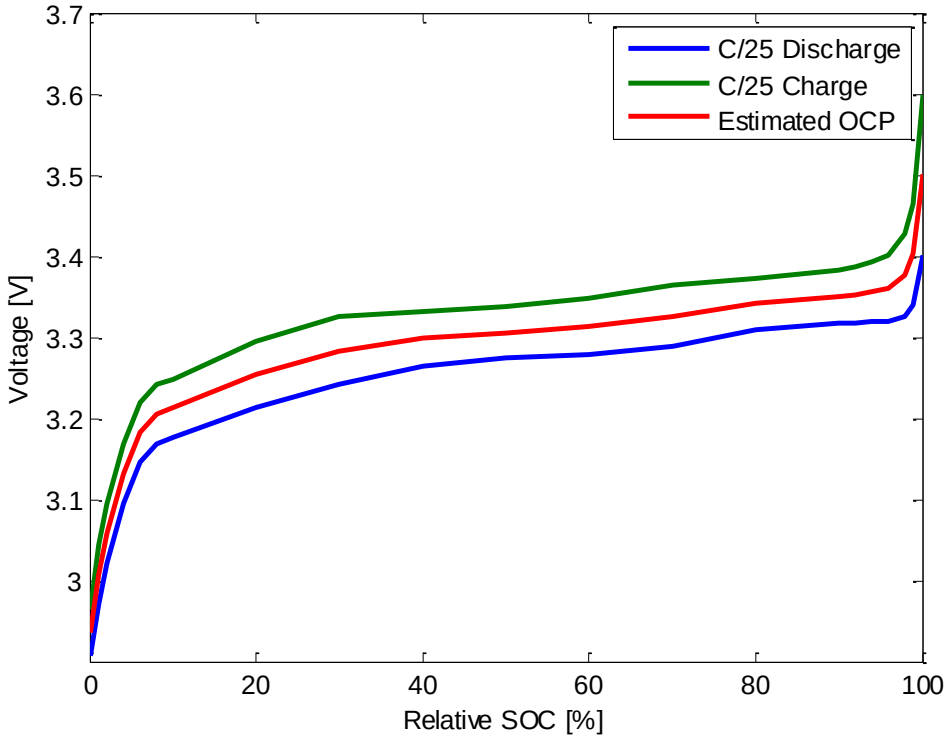

Figure 3.4 Estimated OCP profile using a C/25 charge and discharge rate

3.7 Battery Resistance

The resistance of a battery will affect the performance during its operation. The industry standard for determining the resistance is the hybrid power pulse characterization (HPPC) test, described below (Figure 3.5) [4]. The HPPC test can also be used to measure OCP concurrently with resistance.

- The battery is charged according to the standard charging procedure.
- The battery rests to reach a state of equilibrium to measure the OCP at 100% SOC.
- A 10 s discharge pulse at a specified current is applied to the battery, before a 40 s resting period, followed by a 10 s charge pulse at a slightly lower current.
- The battery is discharged according to the standard discharging procedure until the desired SOC is reached; according to the desired resolution.
- The process is repeated for all of the desired SOC operating points to develop the OCP and resistance profiles along the operational SOC window.

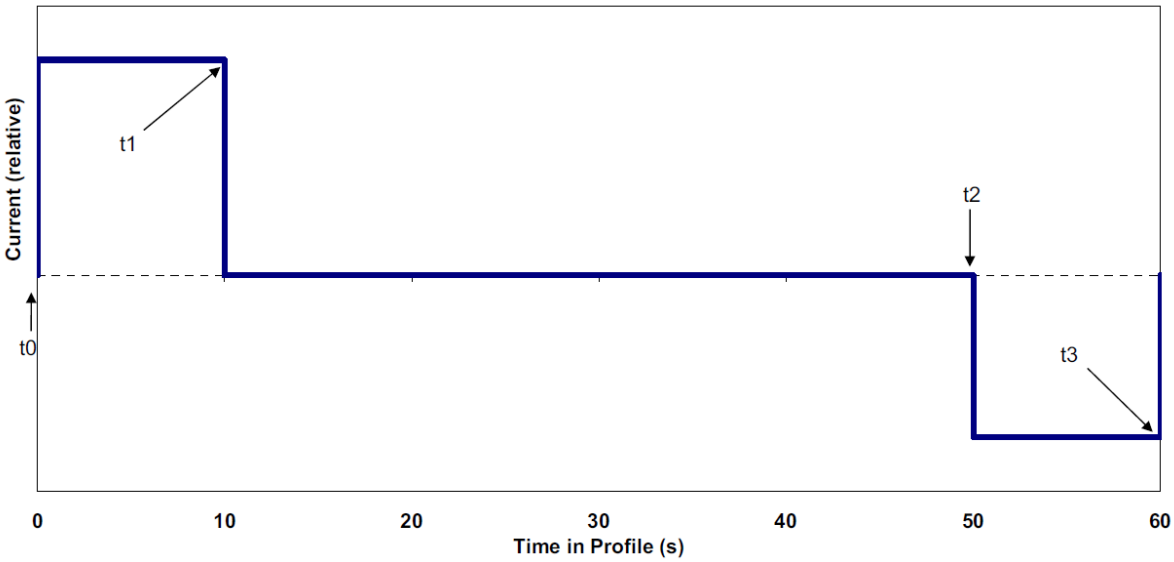

Figure 3.5 HPPC test procedure at each SOC point [4]

While the OCP profile is measured directly from the HPPC tests, the resistance must be calculated from the change in voltage response according to the applied current. The following equation represents the calculation of internal resistance, R_{int}, as a function of the voltage and current at the beginning of the test, V_0 and I_0 respectively, and at the ending of the test, V_{10} and I_{10} respectively [4].

$$R_{int} = \left|\frac{V_{10} - V_0}{I_{10} - I_0}\right| \tag{3.7}$$

Although this is the industry standard, some situations may prevent the use of the HPPC test procedure. For instance, the test equipment may not be able to support the required current to satisfy the HPPC test for a given cell. Alternatively, there may not be batteries to test and one must rely on the data presented by the battery manufacturer. In that case, equation (3.8) can be used to determine the battery resistance for a given current, $I_{c/d}$, assuming the OCP profile, U, and a CC charge or discharge voltage response, $V_{c/d}$, are known (Figure 3.6) [13].

$$R_{int} = \frac{U - V_{c/d}}{I_{c/d}} \tag{3.8}$$

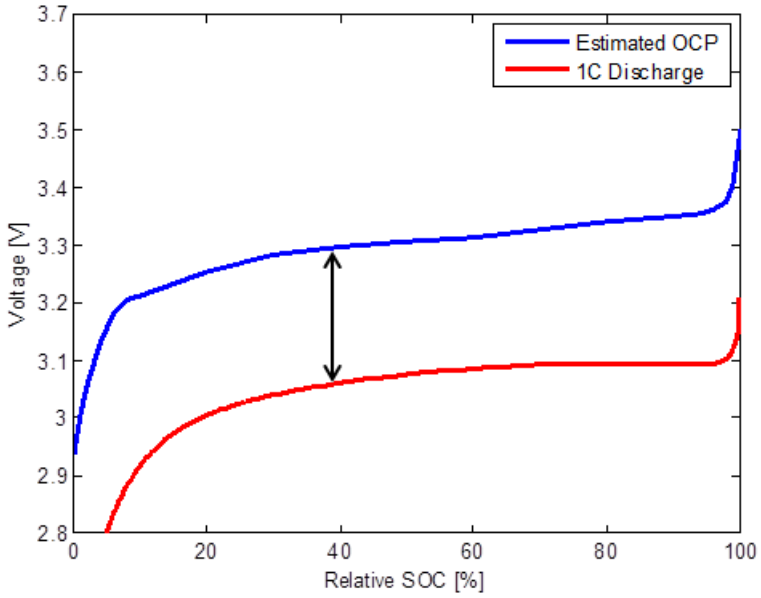

Figure 3.6 Required information for determining the resistance response for a 1C discharge

3.8 Battery Aging

Throughout the life of the battery there will be a slow decrease in cycleable lithium as well as an increase in internal resistance. However, the rate of degradation with respect to capacity and power fade is dependent upon how the battery is used. For the most part, automotive grade batteries are considered to be at their EOL when the capacity fade has reached a specified value; such as 20%

capacity loss. The EOL can also be defined as a 20% reducing in electric range, but it will be considered to be the same condition for the rest of this work. Thus, most of the battery aging tests are designed towards the measurement of capacity fade. The simplest battery aging test is presented below.

- The battery is charged according to the standard charging procedure.
- A resting period allows the battery to reach a state of equilibrium before testing begins.
- The battery is cycled at specified charge and discharge currents, such as 1C charge and 2C discharge, over the operational SOC window, such as 20-80%.
- The discharged capacity is measured at regular intervals over the aging test until the EOL capacity fade has been reached.

Although this test is simple to perform, the capacity fade is dependent upon the usage or operational history of the battery. Note that calendar aging is also an important mechanism that will affect the health of a battery. Essentially, the capacity fade will change for different charge and discharge currents or operating temperatures. The battery aging test can be tailored to represent application-specific operating conditions. Such a test is presented below.

- The battery is charged according to the standard charging procedure.
- A resting period allows the battery to reach a state of equilibrium before testing begins.
- The battery is cycled according to its application, such as a vehicle duty cycle within a SOC window.
- Reference performance tests (RPTs) are conducted at regular intervals over the aging test until the EOL capacity fade has been satisfied.
    - The battery is cycled according to the standard discharging and charging procedures, where the discharged capacity is recorded and used to monitor capacity fade.

The measured discharge capacities from the aging tests can be presented in a plot against time, cycles, or processed capacity (Figure 3.7). Each of the three plots is useful for different applications. Capacity fade over time is useful for determining how long a battery will last according to the cycling procedure. Capacity fade as the cycles increase determine how many times the battery can be operated before it has reached its EOL. Finally, capacity fade presented against the processed

capacity allows for a more standardized presentation of the degradation rate. This plot claims that the rate does not need to depend on time nor the number of cycles, but on the amount of battery usage.

(a) (b) (c)

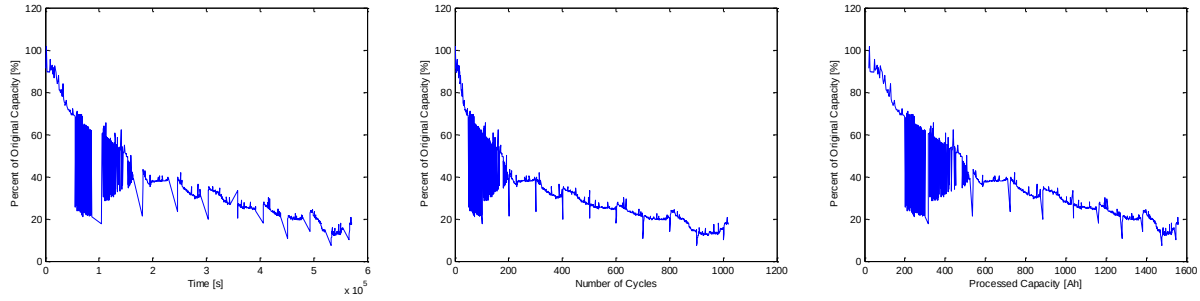

Figure 3.7 Capacity fade presented as a function of (a) time, (b) number of cycles, and (c) processed capacity

There are additional testing procedures available to accelerate the degradation and thus reduce the time required to perform the aging tests. High temperatures, high C-rates, or a combination of the two, are most frequently used in accelerated aging tests. One must be careful to account for the effects of these operating conditions to ensure they do not skew the degradation results.

Chapter 4
Battery Degradation Mechanisms

Although battery systems are already present onboard vehicles, LiBs are currently penetrating the automotive sector more aggressively due to the increasing CAFE standards. The CAFE standards aim to improve fuel economy of future vehicles. One way to satisfy those standards is to electrify part of the vehicle line-up. However, hybrid vehicles are complicated to design because they must satisfy existing performance requirements and last long enough for consumer acceptability. According to several sources, HEVs and PHEVs, and BEVs are expected to sustain performance capabilities for 15 years and 10 years, or 30000 cycles and 20000 cycles, respectively [14, 15]. A direct result of such expectations is the oversizing of LiB packs when designing ESSs onboard vehicles to account for the estimated degradation [16]. Oversizing the ESS can lead to increased vehicle weight, decreased vehicle storage space, and increased costs. Therefore, it is desirable to understand the mechanisms behind battery degradation and how they affect battery lifetime.

Battery lifetime represents the length of time the battery will satisfy performance requirements for a given application. Capacity fade, power fade are two common metrics used to evaluate the degree of battery degradation [16]. Capacity fade appears as a slow decrease in battery capacity available for discharge over the lifetime of a battery. The automotive lifetime for a battery is typically defined as a 20% fade in capacity, at which point the battery has reached its EOL [17]. Capacity fade is important because it represents the fade in available electric range of a hybrid or electric vehicle. Power fade is the slow increase of cell impedance over the lifetime of a battery that reduces its power capability [18, 19]. Although power fade is not typically used for defining EOL, it is important to vehicle applications because it defines how much power the battery can supply without limiting vehicle speed or activating an engine range/power extender. Capacity and power fade can be presented three different ways, depending on their usage. Calendar life is used to present capacity and power fade results for infrequent or low intensity usage such as calendar aging tests of batteries in storage [17]. Cycle life is used to present capacity and power fade results for frequent cycling at regular intervals such as rate capability tests [17]. An alternative to cycle life is to present the degradation against the processed capacity instead of the number of cycles. Processed capacity is often used for frequent but inconsistent usage as a way to compare between different usage profiles; such as drive cycles [17]. Capacity and power fade are metrics that represent the degree of battery degradation.

Batteries degrade according to different mechanisms and processes depending on the components and chemistry within them [18, 14]. Side reactions, structural modifications and changing chemical compositions all contribute to general degradation [14]. The main source of degradation comes from side reactions at the electrode/electrolyte interfaces that irreversibly consume cyclable lithium and create resistive layers of lithium oxides in the cell [18, 14, 19]. Loss of active material from film formation, structural disorder, metal dissolution, particle isolation, and electrode delamination is also a significant source of degradation [18, 14]. Another source of degradation is the increase of resistance from passive film formation of the lithium oxides and electrical disconnects between the electrode subcomponents [18, 14]. Further degradation can occur via binder and electrolyte decomposition as well as current collector and separator corrosion [20, 19]. With respect to calendar and cycling ageing, one would expect to see more aggressive aging from cycling. Side reactions occur within the battery due to thermodynamically unstable materials causing calendar aging [19]. Cycling the battery introduces kinetic effects that accelerate degradation compared to calendar aging rates [19]. As many of the degradation mechanisms are thermodynamically or kinetically dependent, it follows that degradation would depend on environmental and internal conditions.

Environmental and internal conditions of the battery will affect the intensity of the degradation mechanisms and change the rates of capacity and power fade [14]. Capacity fade depends on environmental conditions like temperature and pressure, as well as internal conditions like the processed capacity, power demand, DOD, average operating SOC, and the frequency of a full charge [17]. Factors that affect calendar aging in particular include high temperature, voltage, and SOC storage conditions [17, 14]. Although the factors effecting calendar aging also effect cycling aging, high charge and discharge rates can also accelerate the degradation rate [17, 14]. Details surrounding the degradation mechanisms and their dependence on storage and cycling conditions help elucidate methods for degradation prevention or limitation.

A comprehensive review of all the possible degradation mechanisms is available in Appendix A.

4.1 Negative Electrode Degradation

The negative electrode is considered to be the main component in LiB degradation and has many degradation mechanisms (Figure 4.1). The primary source of degradation at the negative electrode is the parasitic reaction at the electrode/electrolyte interface that develops a passivation film on the graphite active material surfaces [18, 16, 14, 15]. The passivation film offers a solid electrolyte

interface (SEI) between the liquid electrolyte and graphite. Formation of the SEI film irreversibly consumes lithium ions while growing in thickness leading to loss of cyclable lithium and increased impedance, respectively [18, 17, 20]. However it also produces a more stable interface between the electrode and electrolyte that limits further degradation by slowing intercalation kinetics [17, 16, 14, 19]. Calendar aging is primarily a result of SEI film formation. Cycling aging adds several degradation mechanisms by introducing new dynamics to the battery. Structural changes in the carbonaceous active material from intercalation/deintercalation of lithium ions introduce mechanical stress and can lead to physical damage [15]. Loss of contact between sub-components of the negative electrode can occur from non-active material degradation via side reactions or physical damage from mechanical stressors; both resulting in an increased impedance [15]. Finally, lithium plating on the surface of the graphite active material aggressively consumes lithium leading to capacity loss and can cause physical damage to surrounding sub-components leading to increased impedance [15]. It is important to highlight that many of the degradation mechanisms are related and all of them depend on operating conditions.

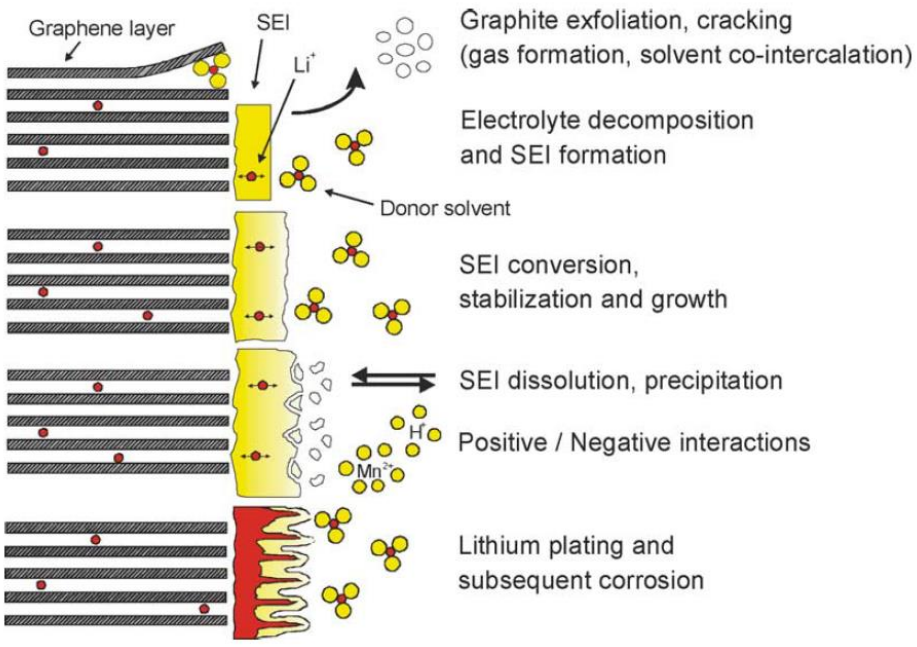

Figure 4.1 Degradation mechanisms for the negative electrode [15]

4.1.1 Degradation from SEI Growth

The majority of the SEI forms during the battery's first cycle followed by slow continuous growth for the remainder of the battery's lifetime [14]. During the first cycle, or formation period, reduction reactions of the electrolyte additives occur on the surface of the active material [15]. The reduction reaction for ethylene carbonate (EC) is presented below [21].

$$EC + 2e^- \rightarrow ethylene + {CO_3}^{2-} \tag{4.1}$$

or

$$EC + e^- \rightarrow EC^- \tag{4.2}$$

$$2EC^- \rightarrow ethylene + CH_2(OCO_2)^- CH_2(OCO_2)^- \tag{4.3}$$

$$CH_2(OCO_2)^- CH_2(OCO_2)^- + 2Li^+ \rightarrow CH_2(OCO_2Li)CH_2(OCO_2Li) \tag{4.4}$$

The reduction reaction for propylene carbonate (PC) is similar to that of EC and also produces a lithium alkyl carbonate [21].

$$PC + 2e^- \rightarrow propylene + {CO_3}^{2-} \tag{4.5}$$

or

$$PC + e^- \rightarrow PC^- \tag{4.6}$$

$$2PC^- \rightarrow propylene + CH_3CH({CO_3}^-)CH_2({CO_3}^-) \tag{4.7}$$

$$CH_3CH({CO_3}^-)CH_2({CO_3}^-) + 2Li^+ \rightarrow CH_3CH(OCO_2Li)CH_2(OCO_2Li) \tag{4.8}$$

The reduction reaction for dimethyl carbonate (DMC) differs slightly from EC and PC [21].

$$DMC + e^- + Li^+ \rightarrow CH_3OCO_2Li + CH_3^* \tag{4.9}$$

or

$$DMC + e^- + Li^+ \rightarrow CH_3OLi + CH_3OCO^* \tag{4.10}$$

Similarly, the reduction reaction for diethyl carbonate (DEC) is presented below [21].

$$DEC + 2e^- + Li^+ \rightarrow CH_3CH_2OCO_2Li + CH_3CH_2^* \tag{4.11}$$

or

$$DEC + 2e^- + 2Li^+ \rightarrow CH_3CH_2OLi + CH_3CH_2OCO^* \tag{4.12}$$

Furthermore, the lithium alkyl carbonate produced from the reduction reactions of the additives reacts in the presence of water according to the following equation [21].

$$2ROCO_2Li + H_2O \rightarrow 2ROH + CO_3 + Li_2CO_3 \tag{4.13}$$

The aforementioned parasitic reactions continue past the formation period, but at a much slower rate. Additionally, reduction reactions for other compounds within the electrolytes occur throughout the battery lifetime. Electrolytic salts such as $LiPF_6$, common to LiBs, can undergo a reduction reaction to form electronically insulating, unstable products according to the following mechanism [21, 20].

$$LiPF_6 \leftrightarrow LiF + PF_5 \tag{4.14}$$

$$PF_5 + H_2O \rightarrow 2HF + PF_3O \tag{4.15}$$

$$PF_5 + 2xe^- + 2xLi^+ \rightarrow xLiF + Li_xPF_{3-x} \tag{4.16}$$

$$PF_3O + 2xe^- + 2xLi^+ \rightarrow xLiF + Li_xPF_{3-x}O \tag{4.17}$$

Finally, if any contaminants are present in the electrolyte, they can undergo reduction reactions with lithium to form lithium oxides or carbonates and gaseous products. The following reduction reaction occurs in the presence of oxygen [21].

$$\frac{1}{2}O_2 + 2e^- + 2Li^+ \rightarrow Li_2O \tag{4.18}$$

The reduction reaction in the presence of water differs from the secondary reaction observed in (4.13) [21].

$$H_2O + e^- \rightarrow OH^- + \frac{1}{2}H_2 \tag{4.19}$$

$$Li^+ + OH^- \rightarrow LiOH \tag{4.20}$$

$$LiOH + e^- + Li^+ \rightarrow Li_3O + \frac{1}{2}H_2 \tag{4.21}$$

In the presence of carbon dioxide, the following reduction reaction occurs [21].

$$2CO_2 + 2e^- + 2Li^+ \rightarrow Li_2CO_3 + CO \tag{4.22}$$

or

$$CO_2 + e^- + Li^+ \rightarrow CO_2{}^-Li^+ \tag{4.23}$$

$$CO_2{}^-Li^+ + CO_2 \rightarrow OCOCO_2Li \tag{4.24}$$

$$OCOCO_2Li + e^- + Li^+ \rightarrow Li_2CO_3 + CO \tag{4.25}$$

The aforementioned mechanisms for SEI formation have one commonality. Each mechanism involves the consumption of lithium ions to produce a lithium-based solid that contributes to the SEI layer. The resulting SEI layer is permeable to lithium ions and other similarly sized species; preventing larger species from interacting with the anode [14, 15]. However, the SEI layer can impede intercalation kinetics at the electrode/electrolyte interface by limiting lithium ion transport and resisting volume changes within the graphitic layers of the negative electrode [20]. Such a volume change can crack the SEI layer, exposing the graphite active material to further reduction reactions [17, 20, 19]. Also, the inhibited transport of lithium ions will increase charge transfer resistance within the cell [20]. Furthermore, the consumption of electrolytic compounds decrease charge transfer capabilities and increase cell impedance. While SEI formation continues throughout the battery lifetime, its growth can be accelerated by various operating conditions.

The electrode/electrolyte interface is inherently unstable [17]. Thus any deviation from ideal operating conditions will affect the reduction reactions at the interface. The SEI formation can be

accelerated by high operating temperatures that drive the kinetics of the exothermic parasitic reaction [17]. Additionally, higher temperatures can transform the SEI into lithium salts less permeable to lithium ions [14]. Oppositely, low-temperature operation can limit SEI formation by reducing the excess lithium ions present at the interface from slower ion transport. Operating the battery at extreme SOCs (*i.e.*, >80% or <20%) will also accelerate SEI formation due to the increased potential gradient between the active material and the electrolyte [17, 14]. Similarly, high and low operating potentials can increase the rate of reaction [16]. Finally, high currents can accelerate SEI growth due to the excess electrons and lithium ions present at the interface used in the aforementioned reduction reactions.

Aside from operating conditions, there are physical properties that can affect SEI growth rates. Dissolution of the positive electrode active material (*e.g.*, Fe^{2+} from $LiFePO_4$ cathode) will accelerate SEI growth by catalyzing the parasitic reaction further [18]. That metallic ion can also deposit itself onto the surface of the graphite [20]. Increasing the negative electrode active surface area or lowering the particle density can increase SEI growth rates because there are more active sites available for the side reactions [20].

4.1.2 Degradation from Lithium Plating

Lithium plating is a degradation mechanism that deposits lithium metal onto the active material of the negative electrode. Lithium plating is possible according to two conditions. The first condition requires a high lithium ion concentration at the active material surface. The second condition requires a negative electrode potential low enough to enable lithium deposition [15]. Low temperature operation decreases lithium diffusion through the SEI layer causing an increased lithium ion concentration at the electrode/electrolyte interface [17, 14, 20, 19, 15]. High current charge rates also lead to lithium plating due to the high lithium ion concentration being intercalated into the negative electrode [17, 20, 19]. Overcharging the battery can cause lithium plating since lithium ions will be unable to intercalate into the filled graphene layers and will therefore deposit onto the surface of the electrode [20]. Additionally, lithium plating is possible when the two electrodes do not have a balanced capacity, or the positive electrode is physically larger than the negative electrode [20]. The former polarizes the negative electrode to low potentials promoting lithium plating [20]. The latter case causes lithium deposits to accumulate on the edges of the negative electrode. To avoid plating the edges, many negative electrodes are designed to have larger dimensions than the positive

electrodes [20]. Finally, the orientation of the graphite particles in the crystal lattice can lead to dendrite formations during the third and fourth intercalation stages [20]. Lithium plating and specifically dendrite formations are dangerous because they can incur physical damage to the cell. Dendrite growth can puncture the separator and connect with the positive electrode causing a short circuit and potential thermal runaway [20]. Fortunately, lithium plating is reversible since lithium oxidizes at a lower potential than the deintercalation process [20]. However, this oxidation causes overpotential within the cell during discharge [20]. Ultimately, lithium plating consumes a substantial amount of lithium ions to dramatically reduce the battery capacity [19].

4.1.3 Degradation from Physical Changes

There are two significant degradation mechanisms associated with physical changes within the negative electrode. The first mechanism describes the loss of contact between its sub-components. The second mechanism describes the structural changes of the graphite leading to physical damage. In both cases, the physical changes of the negative electrode lead to capacity and power fade.

Loss of contact between the separator, electrolyte, graphite, binder, and current collector will increase cell impedance and result in lithium loss [15]. Lithium dendrites formed at the interface can extend to the separator and isolate it from the electrolyte. Volumetric changes from intercalation/deintercalation processes can cause stress fracturing of the graphene layers and can isolate the graphite particles from the current collector [17, 20, 15]. The physical damage can be enhanced by gas formation and solvent co-intercalation within the graphene layers [17, 15]. At high operating temperatures and extreme SOCs, the binder can decompose and limit charge transfer between the graphite and current collector [17]. Eventually, binder decomposition can completely isolate graphite particles from the current collector causing loss of active material. Binders containing fluorine react with lithium ions to produce a solid that can also isolate the graphite from the current collector [15]. A reduction reaction of the electrolyte at the current collector can cause corrosion of the current collector and loss of contact between it and the active material [15]. The loss of contact will decrease electrical conductivity, consume lithium, and reduce the anode capacity for lithium ions.

As previously mentioned, electrode volume changes can lead to structural changes of the active material. Gas evolution, extensive lithium intercalation, solvent co-intercalation, and steep lithium ion gradients within the active material can lead to cracks or breaks in the graphene layers. Changes to the graphite lattice result in less oriented graphite particles within the negative electrode [20]. Less

particle orientation inhibits intercalation kinetics causing a steeper lithium ion gradient [20]. As such, the degradation mechanism can continue throughout the battery lifetime. Again, the physical damage to the graphite will reduce its capacity for lithium ions, offer new active material for SEI growth, and isolate the active material from the current collector. Thus, an increased impedance and decreased capacity will be observed after physical damage to the negative electrode occurs.

4.2 Positive Electrode Degradation – $LiFePO_4$

While a significant portion of negative electrode degradation is associated with SEI formation at the electrode/electrolyte interface, positive electrode degradation is often attributed to physical degradation of its components. However, several mechanisms are similar between the two electrodes (Figure 4.2). The ageing mechanisms surrounding the cathode differ depending on its chemistry since the physical nature of the cathode will differ according to its composition and structure [16, 15]. For this reason, degradation associated with $LiFePO_4$ active material is discussed in detail; though similar mechanisms can be applied to other oxides. Aside from physical degradation of the negative electrode, part of the overall degradation is associated with the formation of a thin SEI film at the electrode surface.

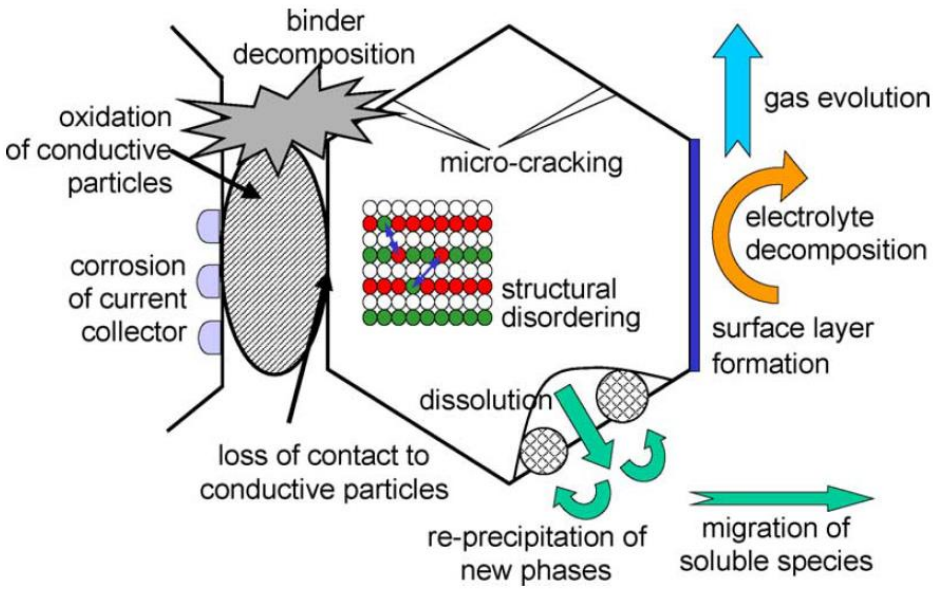

Figure 4.2 Degradation mechanisms for the positive electrode [15]

4.2.1 Degradation from SEI Growth

Similarly to the negative electrode, the electrolyte decomposes at the positive electrode/electrolyte interface [17, 15]. The compounds found in the electrolyte oxidize on the surface to produce a thin film depending on the operating conditions. Contaminants within the electrolyte can catalyze polymerizations or produce gaseous products that develop or damage the SEI film, respectively [19]. Gases can also cause damage to the active material. This SEI formation is difficult to detect because the positive electrode potential is much higher than that of the negative electrode [14]. The SEI formation depends on temperature, SOC, and voltage as with the negative electrode [20, 19]. For storage potentials greater than 3.6 V, the decomposition of the electrolyte is accelerated [20]. Furthermore, high temperature or high voltage storage can promote carbon dioxide evolution leading to mechanical stress on the positive electrode [19, 15]. Although the SEI formation consumes lithium ions and increases impedance, its overall effect on battery degradation is minimal.

4.2.2 Degradation from Physical Changes

A majority of the positive electrode degradation comes from the loss of active material [16, 15]. Physical degradation of the active material includes the structural disordering of the oxide, dissolution of the metallic ions, and surface modifications such as fracturing [16]. High temperatures and voltages promote dissolution of the oxide particles into the electrolyte; increasing impedance [18, 17]. The dissolved species can either precipitate into new phases on the positive electrode or migrate through the electrolyte to interact with the negative electrode SEI [16, 15]. Either way, the loss in active material reduces the positive electrode capacity, which can limit the cell capacity [19]. That phase change can put significant stress and strain on the crystal lattice of the oxide particles causing structural disordering [17, 15]. In addition with the volumetric changes from the insertion and extraction of lithium ions, the stress and strain on the active material can lead to micro-cracking [19, 15]. If the surface modifications of the active material are large enough, loss of contact between the oxide particles and the binder or between the active material in general and the current collector can occur [17, 19]. Loss of contact can also occur due to the degradation of the non-active material within the positive electrode. Binder decomposition, corrosion of the current collector, and degradation of the carbon-based conductive additives are capable of isolating positive electrode sub-components and increasing impedance of the cell [16, 15]. The extent to which such degradation occurs is dependent upon the operating conditions of the battery.

Chapter 5
Battery Modeling with Degradation

Battery degradation modeling is an attempt to predict the battery performance throughout its lifetime. The models aim to predict specific properties of the battery as it ages, such as its resistance, capacity, or power. However, there are several models that predict battery performance and lifetime according to various conditions and restrictions. In general, there are three significant approaches to ageing estimation: physics-based, mathematical, and fatigue modeling [22].

5.1 Physics-Based Modeling Approach

Physics-based degradation models typically use some form of performance or characteristic data in its development. Thus empirical models, empirical equivalent circuit models, and electrochemical models are all categorized within the physics-based modeling approach [22]. Since physical information is required to generate a model, the model's application is limited to the measurement conditions. Therefore, the model cannot be used to predict degradation under conditions that differ from those used to build the model.

5.1.1 Empirical Models

Empirical models are the fastest and simplest of the physics-based models to implement; however, they are also the least flexible [22]. Typically, empirical data is used to determine the battery degradation over a testing period for specific operating conditions. Assuming the operating conditions do not change over the life of the battery, the empirical model can be extrapolated to predict battery lifetime. However, if the operating conditions change, the battery must be tested again to develop a new empirical model to extrapolate. This is a fatal flaw for empirical models attempting to predict battery degradation on-board HEVs, PHEVs, and BEVs, because operating conditions are constantly in flux. Another disadvantage of the empirical models is that they cannot be associated with specific ageing phenomena like the other models can. In other words, there is no physical explanation of the degradation mechanisms occurring within the battery; just that degradation is taking place. Finally, accuracy can be insufficient for life prediction since the extrapolation process requires highly accurate test data and assumes that there is little variance in battery performance and degradation between multiple batteries [22]. Therefore, empirical models are not favorable for predicting battery degradation in vehicle applications.

Omar *et al.* conducted battery testing at various temperatures, DODs, and currents to predict the combined effect on battery life using simple empirical relationships in MATLAB Simulink to within 5.4% error [23].

5.1.2 Empirical Equivalent Circuit Models

Another type of physics-based degradation modeling is an empirical equivalent circuit model. An equivalent circuit is an electrical circuit where its components represent various phenomena within the battery during operation (Figure 5.1a). For instance, the R_1 represents the internal resistance of the cell while the resistor-capacitor (RC) components represent the impedance from each electrode. Equivalent circuit models can be made highly complex by including more electrical components with different circuit architectures [22]. The values of the equivalent circuit components are determined using electrochemical impedance spectroscopy (EIS) measurements. EIS is a test procedure that pulses the battery with sinusoidal voltage (galvinostatic) or current (potentiostatic) for a specified frequency range to measure the real and imaginary impedances and present the results in a Nyquist plot (Figure 5.1b). The equivalent circuit component values will change with operating conditions (*e.g.*, temperature, SOC, current) and as the battery ages [22]. Thus, EIS tests are required during performance and ageing tests to determine how they change under different operation and to determine their degradation trends. By doing so, it is possible to understand and predict which battery components (*e.g.*, electrolyte, anode, cathode) are degrading; and at what rate. Unfortunately, since these models are empirically-based, they share the same limitations presented for the empirical models [22]. The degradation trends derived from ageing tests are extrapolated into the future to predict battery lifetime. Ultimately, the models are only applicable for applications similar to the tests used to construct the model. Although the empirical equivalent circuit model is an improvement to the empirical model, and sufficiently predicts fresh cell performance, it is insufficient for battery lifetime prediction of vehicle battery packs.

(a) (b)

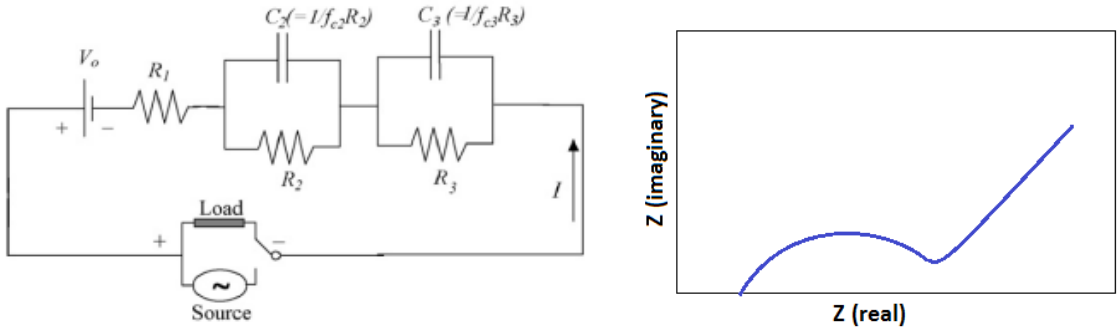

Figure 5.1 (a) Equivalent circuit model of a battery [22] and a (b) Nyquist plot resulting from EIS testing

Empirical models are less common now that computation power has allowed the application of more complicated models. However, one example of an empirical degradation model is that of Takei *et al.*, where linear models were fit to performance data and acceleration stress factors were determined from aging data; though error was as high as 40% [24].

5.1.3 Electrochemical Models

The most common type of physics-based modeling is electrochemical models [22]. These models use a combination of electrical and physical properties to express the physico-chemical processes occurring within the battery [22]. Electrochemical models often consist of several equations that relate the electrical and physical properties together; for which there can be many. The most common equations used in electrochemical models are those from Fick's (1) and Ohm's laws (2), and the Butler-Volmer (3) and Tafel (4) equations; however several more are frequently combined with those listed [22]. The number and complexity of equations can be adjusted according to the desired accuracy. Unfortunately, with more complex systems there are more physical parameters to measure (*e.g.*, diffusion coefficient, particle size, electrode thickness), and the computational time can increase dramatically [22]. Furthermore, the physical parameters being measured will change according to battery usage and as the battery ages; making it difficult to produce an accurate model [22]. This becomes an issue when attempting to apply an electrochemical degradation model to vehicle applications. To combat this, many researchers assume a single source of degradation, limit the dimensions of the equations, or otherwise simplify the systems to appropriate complexities to

diminish the experimental and computational costs [22]. Although there are limitations, electrochemical models are flexible and can be applied to several different systems because they are based on electrochemical and physical measurements instead of ageing tests [22]. Additionally, a single model can be used between different batteries as long as they have similar chemistries and ageing mechanisms. Therefore, a simplified electrochemical model of lithium ion batteries is recommended for lifetime prediction of a battery pack on-board a vehicle.

One type of electrochemical model common to battery modeling is the single particle (SP) model. The SP model considers the battery as two separate particles representing a typical particle on the anode and cathode. It is often preferred to the more complex pseudo-two-dimensional (P2D) models because of the lower computational times [25]. The particles do not interact with each other and the dynamics associated with the electrolyte are neglected. Zhang and White used a SP model to simulate battery degradation and discovered three likely stages of capacity fade for low cycling rates [26]. Safari *et al.* took advantage of the SP model to generate a degradation model and assess whether SEI growth was predominantly kinetic or diffusion limited [11]. Safari also used a SP model to determine the viability of the fatigue modeling approach; presented later in this section [27]. Prasad and Rahn used an SP model as a basis for constructing an equivalent circuit where its parameters are updated throughout the battery's lifetime [28, 29].

The 1D model is similar to the SP model but it accounts for the presence of the electrolyte in the cell. Ning *et al.* used a 1D model to assess the effect of various parameters on battery lifetime [30]. Prada *et al.* used a 1D degradation model that includes the electrolyte and assumes that the sole source of aging is SEI growth [31].

The P2D models offer more detailed simulation results but require more understanding of the battery. Farkhondeh and Delacourt use the P2D model to account for several particle sizes in the positive electrode active material and to introduce the idea of a variable solid-state diffusivity (VSSD) of lithium ions into the active material [32].

5.1.4 Semi-Empirical Electrochemical Models

In more recent works, electrochemical models use experimental data to empirically fit one or more of their parameters. Ramadass *et al.* empirically fits the decrease in SOC, increase in impedance, and the diffusion coefficient to satisfy experimental degradation data [33].

5.2 Mathematical Modeling Approach

Mathematical degradation models work to determine the relationships between input and output data such as operating conditions and SOH [22]. Artificial neural network (ANN) models are the primary type of models within the mathematical modeling approach [22]. ANN models learn from input and output data by altering internal relationships between them. The more input and output data available to teach the ANN, the better the predictability of the ANN [22]. In general, there are five distinct phases to developing an ANN. The first phase, as previously mentioned, is to collect as much input and output data as possible according to the information required to construct a model [22]. For example, input data could include temperature, SOC, and current, while the output data could include capacity, resistance, or SOH. The second phase is to process the data for input into the ANN [22]. The third phase uses the input and output data to develop the ANN by statistically minimizing the error [22]. The fourth phase is to validate the ANN predictability by comparing the ANN output results with the measured data [22]. The final phase is to implement the ANN into its application [22]. Unfortunately, it has been found that an excessive amount of data is required to build an accurate ANN model. Mellit [60] showed that 4 years of data collection provided an ANN capable of predicting performance one year into the future. Additionally, assuming an ANN was developed with the necessary amount of data, the degradation mechanisms would be unknown since the network is statistically arranged to reduce error. Thus, the ANN models do not hold physical meaning. Other mathematical approaches currently in use include fuzzy logic models, fuzzy neural networks, neuro-fuzzy based modeling, and adaptive algorithms; however all of the alternatives share in the ANN model's limitations [22]. Therefore, mathematical modeling is an illogical choice for developing a battery pack degradation model for vehicle applications.

5.3 Fatigue Modeling Approach

5.3.1 Wohler Models

Fatigue modeling considers the battery as a mechanical system that undergoes stress and strain throughout its lifetime. Certain events occur during battery usage that impact its lifetime in an incremental manner. Originally, the fatigue model was developed for metal fatigue of rail tracks by a man named August Wohler [22]. He discovered that the metal would fail after experiencing cyclic stress that accumulated over its lifetime and produced a useful plot showing the number of cyclic loads the metal could withstand depending on the applied stress [22]. With respect to battery

degradation, many use a similar curve to show the number of charge/discharge cycles a battery can withstand depending on the DOD, charging voltage, or temperature of that cycle [22]. Unfortunately, the Wohler fatigue model can only be used for cycles with a constant DOD. The Palmgren-Miner (PM) rule was developed to account for variation in the DOD throughout the battery lifetime and states that the damage from one cycle at a given DOD is cumulative with the damage from another cycle at a different DOD [22]. The cycles with similar DODs are grouped together as a type of event and impact the battery lifetime according to their frequency [22]. An issue with the Wohler method is that it assumes there is no interaction between the ageing events; only that they are cumulative with each other. Furthermore, it assumes constant impact from the events no matter how old the battery is. Finally, it does not account for the highly variable operating conditions a battery experiences on-board a vehicle. Therefore, the Wohler model is not applicable to battery degradation in automotive applications.

5.3.2 Weighted Ah Model

The weighted Ah model was developed as an improvement upon the Wohler method for use in vehicles. Unlike the Wohler method, the weight Ah model determines lifetime reduction based on the Ah throughput of the battery instead of the number of cycles it has experienced [22]. Since the severity of fatigue from the temperature, SOC, or current events will differ, weighting factors are applied to the events to accurately accumulate the effective Ah throughput. A battery is said to fail once the effective Ah throughput surpasses the total Ah throughput of the battery [22]. Another benefit of the weighted Ah model is that it can be developed without destructive testing; unlike the other models previously presented [22]. Ultimately, these differences add a level of complexity above the Wohler method that allows for its use in the automotive sector for battery lifetime prediction; however limitations still exist. One limitation is the constant weighting factors associated with the events throughout the lifetime of the battery. The electrochemical and empirical equivalent circuit model parameters are updated as the battery ages, but the weighted Ah throughput parameters are not. Another limitation is that the weighted Ah throughput model does not attribute fatigue when there is no current flow [22]. In other words, the model does not account for calendar ageing. Thus, a combination of multiple lifetime prediction models would be required for an automotive battery pack. Ultimately the weighted Ah model shows promise for automotive applications, but has not progressed far enough with respect to accurate lifetime prediction. Therefore it is not recommended as a battery degradation model for vehicles.

5.3.3 Significant Conclusion from Fatigue Modeling

The mechanical fatigue model proposed by Safari *et al.* is based on Wohler's fatigue model, which presents the number of cycles or time before a mechanical failure occurs according to the amplitude of an oscillatory tensile stress; known as a Wohler curve [27]. However, the Wohler curve is only applicable for oscillatory stress with constant amplitude [27]. Since drive cycles will impose variable amplitude oscillatory stresses on the battery, the Wohler fatigue model does not apply. The PM rule is used to account for variable amplitude oscillatory stresses.

For a given profile consisting of N events of type i, the PM rule states that the damage accumulated from one event of duration Δt_i will cumulate with previous damage of the same type until the damage reaches an EOL at t_i^f [27]. The EOL is defined according to the application and in the automotive industry the EOL is defined as a 20% loss in discharge capacity.

$$\sum_{i}^{N} \frac{\Delta t_i}{t_i^f} = 1 \tag{5.1}$$

Cycle counting methods such as level crossing and rain flow cycle counting determine the number of events for each type of stress within a variable load profile [27].

Although the PM rule is a common rule among mechanical fatigue modeling, it requires that the time until EOL is known and ultimately only offers the ability to predict the progression of fatigue over the battery lifetime; not the ability to predict future fatigue.

The concept of damage accumulation proposed by the PM rule is used to develop a predictive model for damage accumulation over time; where D is the total accumulated damage over N events at t_{i+1}, D_i is the accumulated damage at t_{i+1} for an event, i, with a constant magnitude of stress S_i and a duration of t_i to t_{i+1} [27].

$$D = \sum_{i}^{N} \left(\frac{\partial D_i}{\partial t}\right)_{S_i}\Bigg|_{(t_i+t_{i+1})/2} (t_{i+1} - t_i) \tag{5.2}$$

The damage accumulation equation is approximated below for aging times much longer than the period of the profile; where N_e is the number of events in a periodic motif, and Δt_m is the duration of the periodic motif [27].

$$D = \sum_{i}^{N_e} \frac{\Delta t_i}{\Delta t_m} D_i \tag{5.3}$$

Safari *et al.* conclude that the PM rule more accurately predicts the aging simulation results compared to the damage accumulation method; however both predict adequately [27]. Therefore, the damage accumulation method will be used to discretize a duty cycle into pulses and sum the degradation for each pulse over the entire duty cycle. The result will provide a significantly accurate estimate of the real degradation for that cycle.

Chapter 6
Automotive Industry

6.1 Current Vehicle Technologies

There are several vehicle technologies available to consumers including conventional vehicles, BEVs, HEVs, and PHEVs. The most prevalent type of vehicle available is the conventional vehicle, which uses a gasoline engine to provide mechanical power to the wheels through the transmission (Figure 6.1). The conventional powertrain will dominate the market less as the annual increase in CAFE standards push for better fuel economies. Automotive manufacturers will shift from conventional powertrains to HEV, PHEV, and BEV powertrains to satisfy the CAFE standards; making these powertrains more accessible to consumers.

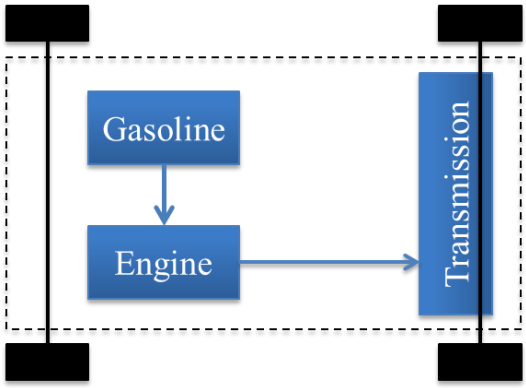

Figure 6.1 Conventional vehicle powertrain

A conventional vehicle's fuel efficiency can be substantially improved through electrification. Electrification is the evolution of a conventional vehicle into a purely electric vehicle. A HEV is one example that uses hybridization by combining two power sources to reduce fuel consumption and electrification by using a high voltage battery pack and electric motor as the second power source. However, there are several different hybridization technologies that are not electric such as flywheels and there are several different electrification technologies such as ultracapacitors or fuel cells. Herein, hybridization will inherently mean electrification through battery technology.

As the number of power sources increases, so too does the complexity associated with designing such a powertrain. For HEVs, there are three primary powertrain architectures: series, parallel, and power-split (Figure 6.2).

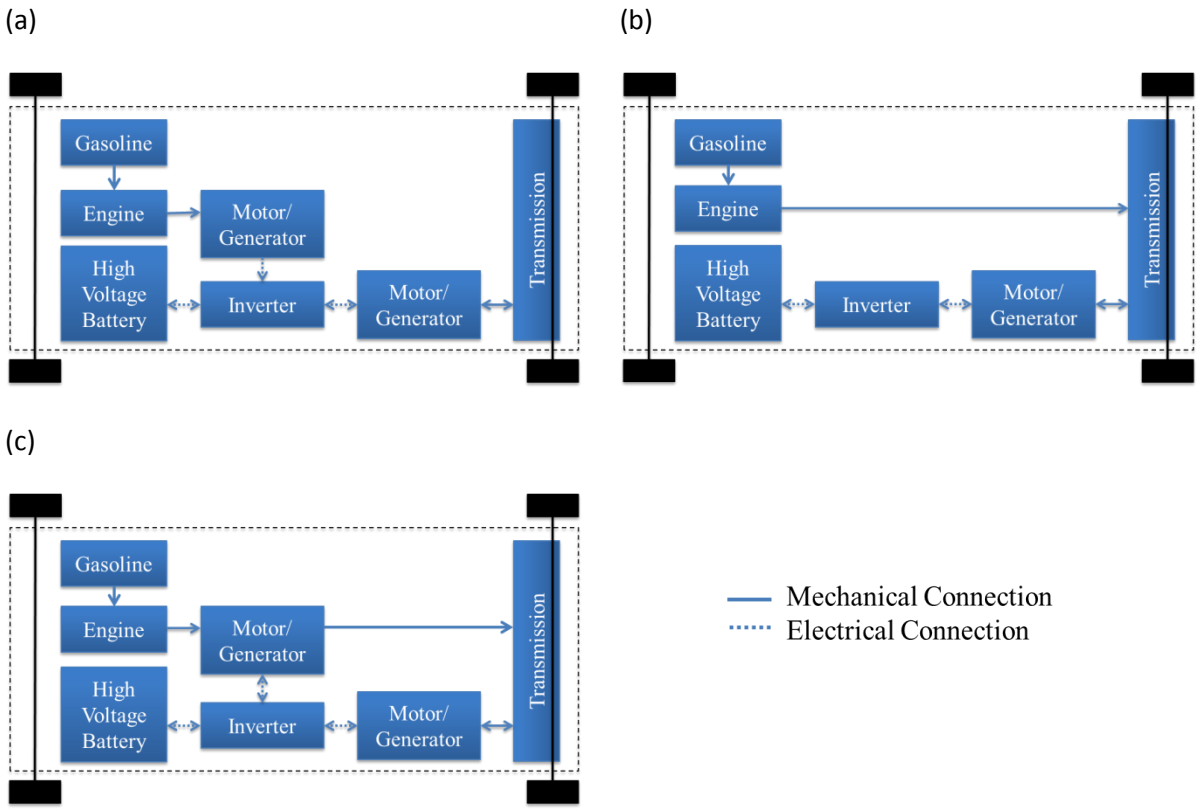

Figure 6.2 (a) Series, (b) parallel, and (c) power-split hybrid vehicle powertrain architectures

The series hybrid architecture removes the direct mechanical connection between the engine and transmission. By isolating the engine from the transmission, it follows that the engine can operate in its maximum efficiency range while the battery balances any power transients in the system [34, 35]. Also, the transmission does not require a gearbox since the motor connected to the driveshaft has an ideal torque-speed profile [35]. Thus, the series architecture simplifies the transmission greatly. A disadvantage of this architecture is the increased efficiency losses by converting mechanical power from the engine into electrical power and back to mechanical power to propel the vehicle [34, 35]. However, these inefficiencies are typically small and the benefits of this architecture outweigh the limitations.

The parallel hybrid architecture contains a direct mechanical connection between the engine and transmission and an electrical-mechanical connection between the battery and transmission. The direct mechanical connection eliminates the need to convert engine power between forms before it reaches the wheels, which increases efficiency [35]. While the direct mechanical connection will

result in engine speed transients, the battery-motor connection will balance any torque transients [34]. Ultimately, the parallel architecture lowers vehicle mass by replacing the motor/generator with a gearbox, but increases the complexity of powertrain control [35].

The power-split hybrid architecture is essentially the combination of the series and parallel architectures. There is an opportunity for the engine to directly turn the wheels or for it to interact with the electrical system within the powertrain. While efficiency and performance of the powertrain are improved from its predecessors, the added components required for this architecture significantly increase the vehicle mass and the complexity involved in its power management [34].

The series, parallel, and power-split HEV architectures also apply to PHEVs. Since both HEVs and PHEVs involve the combination of the gasoline engine with a high voltage battery pack, the aforementioned architectures are also used to build PHEVs. While the components remain the same between the two vehicle types, the control strategies differ greatly. Fundamentally, HEVs supplement the engine power with battery power to satisfy the vehicle power demands. By doing so, the engine can be slightly downsized depending on the battery size. However, PHEVs rely on the battery pack as the primary power source until its SOC is depleted to a lower operating limit; at which point the engine turns on and the vehicle operates as an HEV (Figure 6.3). At the end of a trip, the driver can connect the vehicle to the electrical grid to charge the battery; hence the name of this vehicle type.

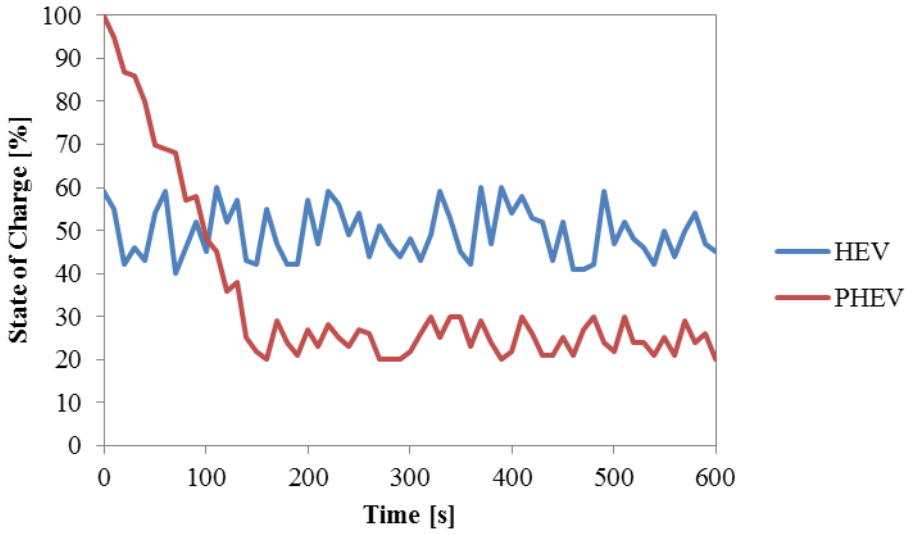

Figure 6.3 The differing power management control strategies between HEVs and PHEVs

Powertrains increase in complexity as the number of power sources, components, or the level of control increases. The conventional and BEV powertrains are simplest to model since they have a single power source and limited control requirements. The HEV and PHEV powertrains are more complex because they have multiple power sources, and require more components and controls to combine those power sources in an efficient manner. In a BEV the ICE is replaced by a battery pack and electric motor and the gearbox is removed leaving only the final drive gear. The BEV captures otherwise lost energy from regenerative breaking. The efficiency of the BEV, ca. 70%, is also much higher than that for conventional vehicles, ca. 18% [36]. The primary limitation of BEVs that is not a concern for conventional or hybrid vehicles is the available driving range of the vehicle. Since the BEV relies on stored energy in the battery pack, it follows that the battery will eventually deplete its energy; thus limiting range. For this reason alone, many argue that the range of BEVs is not yet large enough for most consumers and that hybrid vehicles offer an ideal balance between range and fuel efficiency.

6.2 Vehicle Modeling

6.2.1 Model Based Design

The principles of model-based design (MBD) are essential for vehicle modeling. MBD includes the development of plant and control models incorporated into a vehicle model that can be simulated offline before deployment. Plant models represent the physical systems onboard a vehicle such as the engine, wheels, or chassis. Control models represent the controllers and control system onboard a vehicle like the high-level powertrain controller or the low-level engine controller. Combined, the plant and control models represent a working vehicle that can be simulated offline instead of having to build and physically test that vehicle. In general, any component can be changed via the plant or control models to generate a vehicle prototype. Ultimately, MBD offers offline simulation of multiple vehicle prototypes in 3% of the time per simulation, with immense financial savings.

6.2.2 Software

The MBD procedure has been simplified by Autonomie; vital software produced by Argonne National Laboratory and funded by the U.S. Department of Energy. Autonomie offers a step-by-step graphical user interface (GUI) into the MBD process, allowing for fast and simple vehicle design and simulation. Included in the software is a comprehensive database of existing plant, control,

powertrain, and vehicle models that accelerate the first few steps of the MBD process. Simulation results are saved and presented to the user to provide insight into component and vehicle performances.

It is important to recognize that Autonomie is based upon and relies on MATLAB Simulink to function. MATLAB Simulink is visual computational software used by Autonomie's GUI to generate vehicle models by virtually connecting the plant and control models. In other words, Autonomie offers the interface for the user to interact with the vehicle models generated by MATLAB Simulink. The vehicle models in MATLAB Simulink are considered to be causal models because a desired vehicle speed is fed into the model and controllers demand the necessary power to meet that desired vehicle speed. An example of a non-causal model would be if the desired vehicle speed was specified as the actual vehicle speed and the necessary power was back-calculated.

6.2.3 Level 1 Vehicle Model Development

The 2011 Chevrolet Equinox LS has been selected for MBD to satisfy the interests of this investigation into battery degradation modeling as well as those of WatCAR who purchased a retro-fitted BEV prototype. This section summarizes the modeling efforts for investigating the benefits of powertrain electrification using battery technology.

The conventional model represents the base 2011 Chevrolet Equinox LS that utilizes an internal combustion engine as its sole power source. The conventional powertrain that Autonomie generates (Figure 6.4) will require refinement to correctly represent the 2011 Equinox. Such a refinement can be conducted using the component specifications of the 2011 Equinox (Table 6.1). Although Table 6.1 presents a summary of the specifications, a full specification sheet is provided in Appendix B [37].

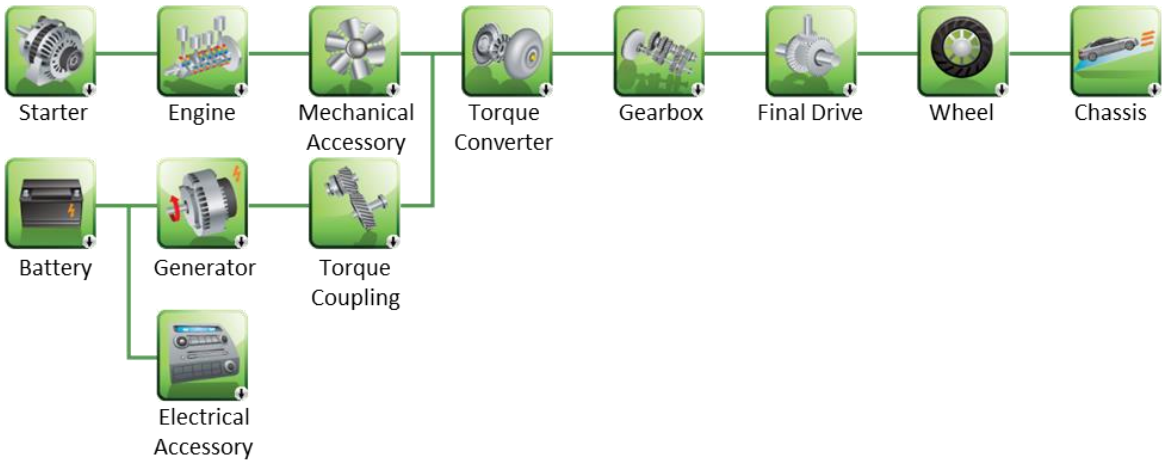

Figure 6.4 Autonomie generated conventional powertrain model components

Table 6.1 Chevrolet Equinox specifications used to generate a conventional vehicle model

Component	Specification	Value	Units
Engine	Displacement	2384	cm^3
	Maximum Power	136	kW
	Speed at Maximum Power	702	rad s^{-1}
	Maximum Torque	233	Nm
	Speed at Maximum Torque	513	rad s^{-1}
Transmission	First Gear Ratio	4.58	
	Second Gear Ratio	2.96	
	Third Gear Ratio	1.91	
	Fourth Gear Ratio	1.44	
	Fifth Gear Ratio	1.00	
	Sixth Gear Ratio	0.74	
	Final Drive Ratio	3.23	
Tires	Tread Width	0.225	m
	Aspect Ratio	65	%
	Diameter	0.432	m
Chassis	Overall Width	1.842	m
	Overall Height	1.684	m
	Minimum Ground Clearance	0.199	m
	Vehicle Mass with 80 kg Driver	2150	kg
	Weight Distribution (Front/Rear)	58/42	%/%

In addition to the vehicle component specifications, the engine plant model in particular needs to be further refined to ensure that the correct amount of fuel is consumed during operation. This process requires a maximum torque curve and a fuel consumption rate look-up-table (LUT) (Figure 6.5) [38].

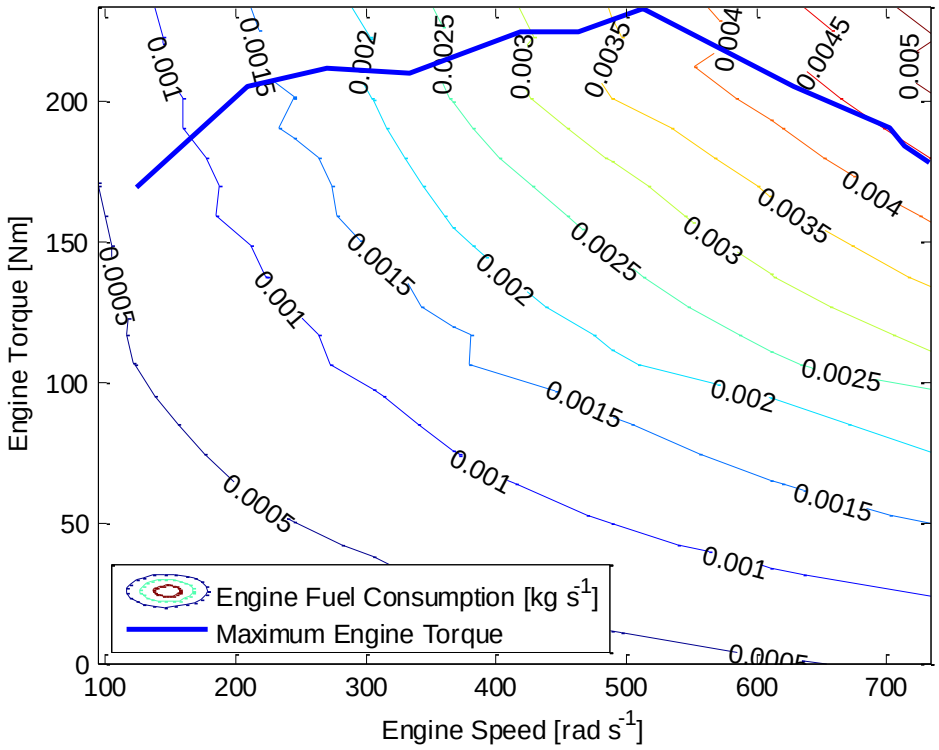

Figure 6.5 2011 Equinox engine fuel consumption rate LUT and maximum torque curve

The maximum torque curve has been visually converted into a digital format from specification sheets provided in Appendix C. Additionally, the fuel consumption rate LUT has been manually altered to consume the correct amount of fuel according to the U.S. EPA 5-cycle testing procedure (Figure 6.6) [39]. Three bags are used to collect emissions during the federal test procedure. Additionally, the city and highway sections of the US06 drive cycle are split. While only four cycles are presented below, the federal test procedure is tested again with air conditioning on.

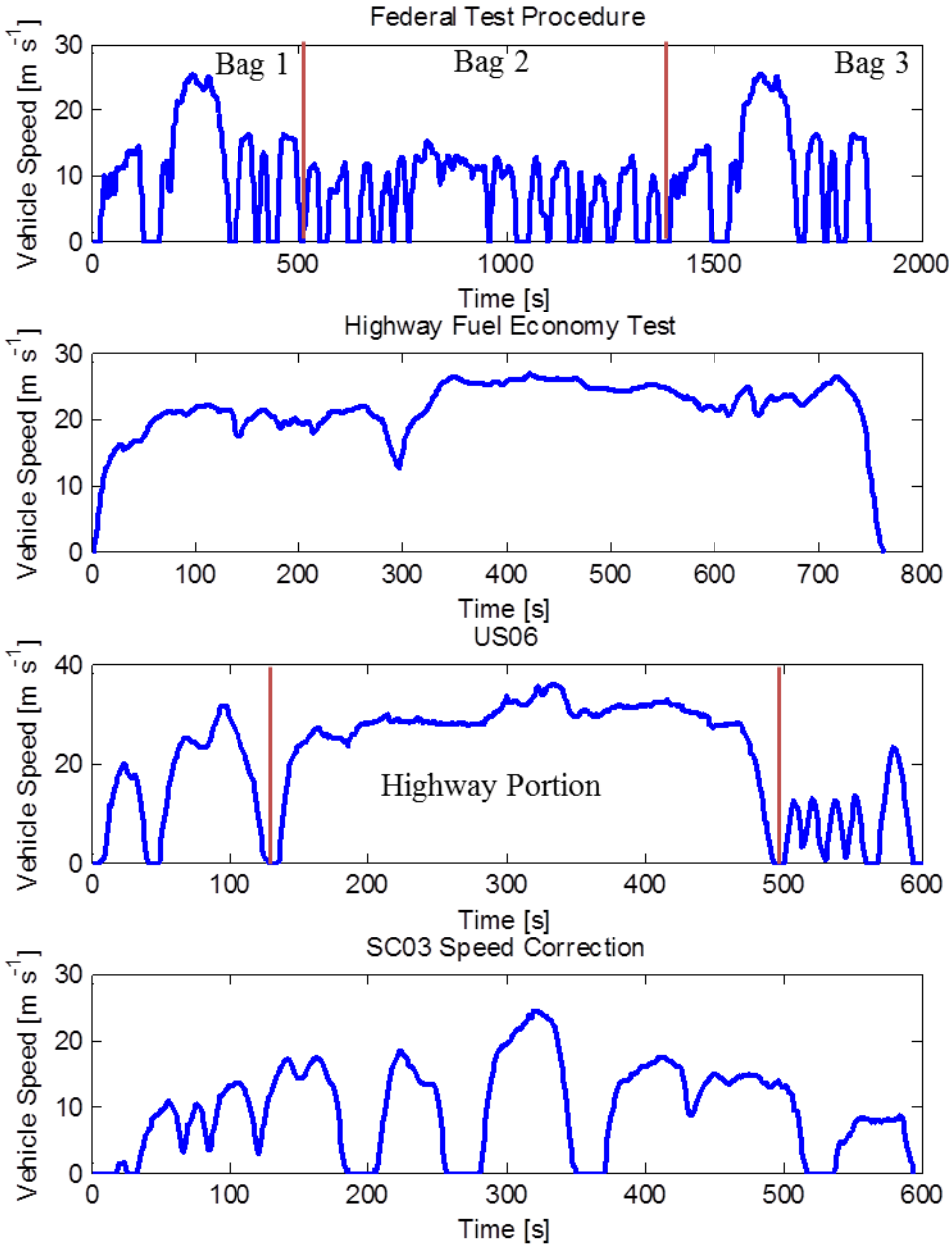

Figure 6.6 EPA 5-cycle test procedure drive schedules

After integrating the powertrain component specifications and altering the engine fuel rate consumption LUT, the vehicle model is simulated on the five EPA test cycles to validate that the model accurately predicts dynamometer driving conditions. The 5-cycle test procedure is used to calculate the city and highway fuel economies according to the Code of Federal Regulations 40 CFR 600.114-08 [40]. The 5-cycle test procedure includes hot and cold engine testing, but the simulations do not consider engine temperature. This introduces error to the model, but for the purpose of this work, having a vehicle model that depends on temperature is not necessary.

Simulations of the vehicle model produced city, highway, and combined fuel economies of 22 MPG, 32 MPG, and 26 MPG respectively. These fuel economies are equivalent to those published for the 2011 Chevrolet Equinox LS [37]. The combined fuel economy, F_{comb}, is not determined from a duty cycle like the city, F_{city}, and highway, F_{hwy}, fuel economies; but is calculated based on their results [41].

$$F_{comb} = \frac{1}{\frac{0.55}{F_{city}} + \frac{0.45}{F_{hwy}}} \tag{6.1}$$

Thus, the completed conventional vehicle model of a 2011 Chevrolet Equinox LS acts as a basis for evaluating the benefits of electrification.

6.2.4 Level 2 Vehicle Model Development

The first step in MBD of the 2011 Chevrolet Equinox Retrofit EV is to develop a component-based BEV powertrain (Figure 6.7) without accounting for real world driving effects. Ultimately the simulation results from such a model would roughly represent dynamometer results for the conventional model. However, the results will be presented in mile per gallon equivalent (MPG_e) since a BEV only consumes electrical energy during operation.

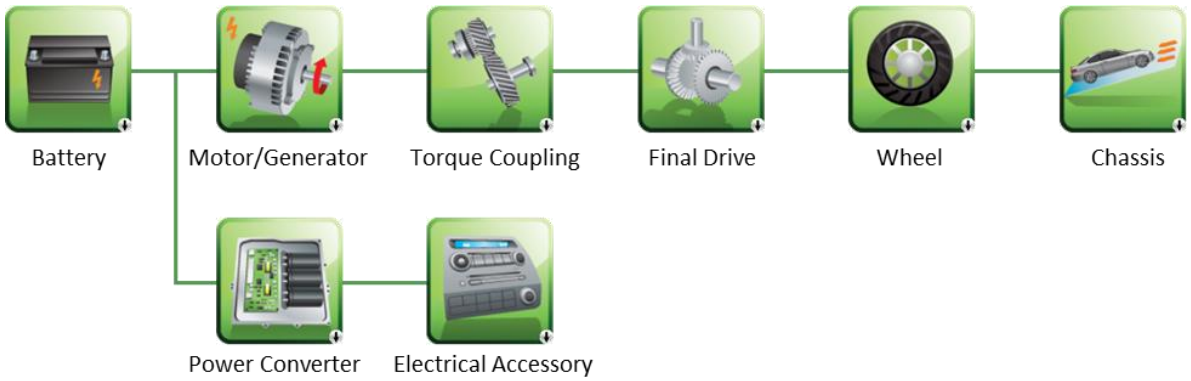

Figure 6.7 Autonomie generated BEV powertrain model components

Similar to the conventional model, the generic Autonomie BEV model needs to be refined using component specifications (Table 6.2) to accurately represent and predict the performance of the purchased Equinox Retrofit EV.

Table 6.2 2011 Chevrolet Equinox Retrofit EV specifications used to generate a BEV model

Component	Specification	Value	Units
Battery	Cell Capacity	100	Ah
	Nominal Voltage	3.2	V
	Configuration	1P108S	
Motor/Generator	Maximum Peak Torque	223	Nm
	Maximum Continuous Torque	128	Nm
	Maximum Speed	1257	rad s^{-1}
	Maximum Peak Power	61	kW
	Maximum Continuous Power	41	kW
Transmission	Final Drive Ratio	8	
Wheels	Effective Radius	0.351	m
Chassis	Overall Width	1.842	m
	Overall Height	1.684	m
	Ground Clearance	0.648	m
	Vehicle Mass with Driver and Passenger	2043	kg
	Weight Distribution (Front/Rear)	58/42	%/%

The aforementioned specifications used to refine the generic BEV model were supplemented with battery and motor performance data. The battery model relies on OCP (Figure 6.8) and resistance LUTs (Figure 6.9) to predict performance, while the motor requires an efficiency LUT (Figure 6.10).

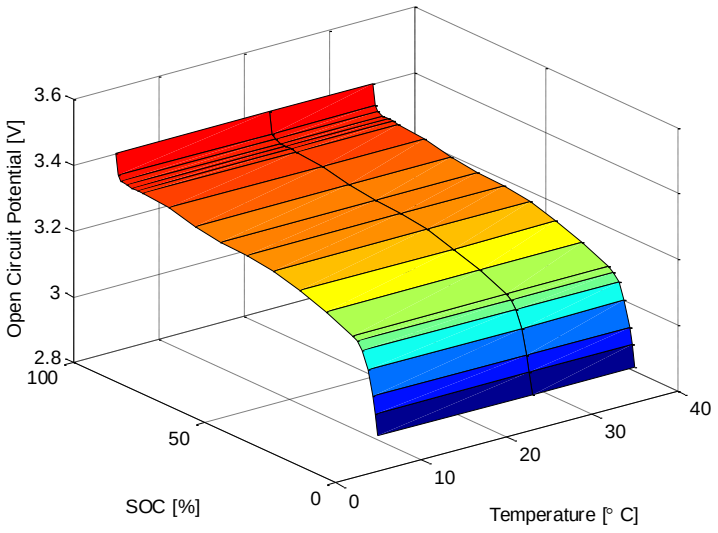

Figure 6.8 2011 Equinox Retrofit EV battery pack OCP LUT

(a) (b)

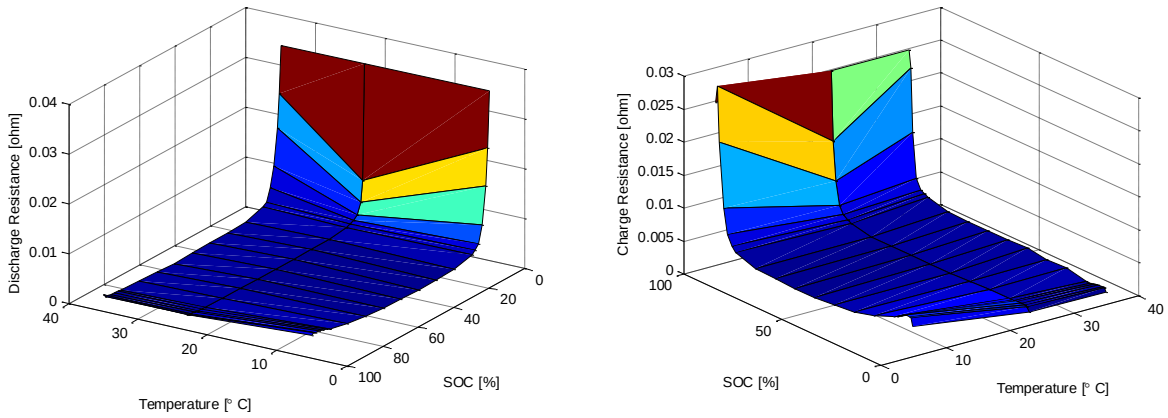

Figure 6.9 2011 Equinox Retrofit EV battery pack (a) discharge and (b) charge resistance LUTs

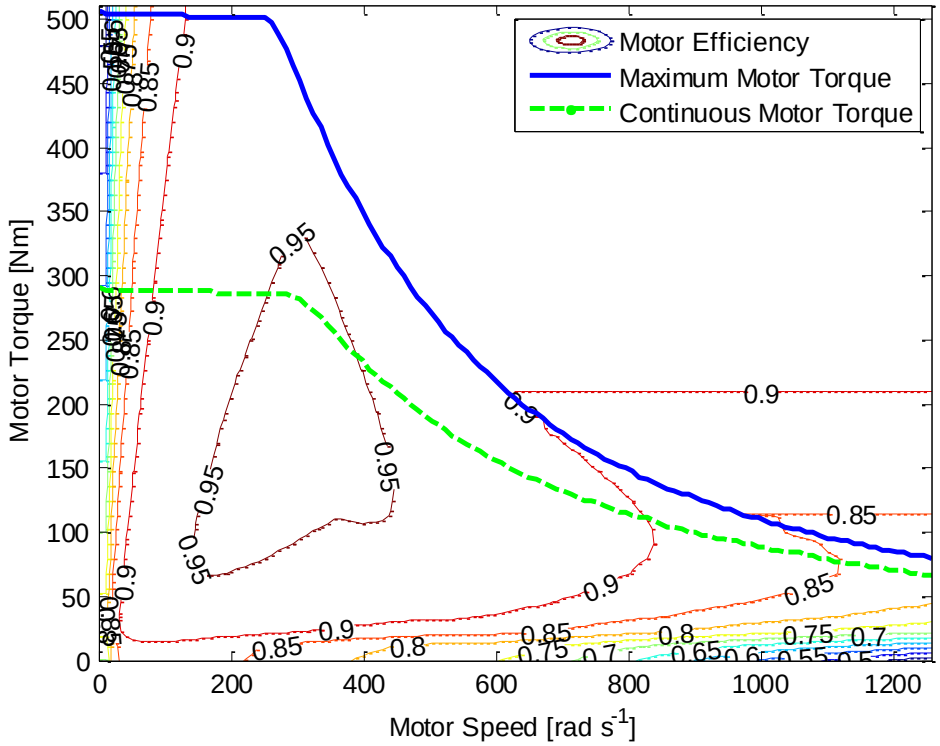

Figure 6.10 2011 Equinox Retrofit EV motor efficiency, maximum torque and continuous torque LUTs

The simulation results of the 2011 Chevrolet Equinox Retrofit EV model must be converted from electrical energy consumption to fuel consumption to determine the MPG_e; where D is the trip distance, E is the energy consumed during the trip, τ is a conversion factor between electrical energy and fuel volume (33.70 kWh gal^{-1}) [42], σ is the correction for the change in SOC during the trip, ΔSOC is the change in SOC, V_{nom} is the nominal voltage, N_{series} is the number of cells in series, and $N_{parallel}$ is the number of cells in parallel.

$$MPG_e = \frac{D\tau}{E + \sigma} \tag{6.2}$$

$$\sigma = |\Delta SOC| Q_{max} V_{nom} N_{series} N_{parallel} \tag{6.3}$$

For an EV, the consumed electrical energy must be replaced. Thus, the MPG_e calculation should account for the energy used to recharge the battery to its starting SOC. A performance-based

comparison between the conventional vehicle and the retrofitted vehicle is presented below in Table 6.3, along with the MPG_e calculation without the SOC correction. This introduces one pitfall associated with fuel economy ratings for EVs is that the published ratings do not account for this change in SOC; making EVs seem more fuel efficient than in reality. Nonetheless, the retrofitted EV displaces a significant amount of fuel.

Table 6.3 Fuel economy results for the conventional and retrofitted 2011 Equinox models

Vehicle Model	FTP	FTP $\sigma = 0$	HWFET	HWFET $\sigma = 0$	Combined	Combined $\sigma = 0$
Conventional	22 MPG		32 MPG		26 MPG	
Retrofitted EV	62 MPG_e	127 MPG_e	47 MPG_e	96 MPG_e	54 MGP_e	111 MPG_e

6.2.5 Level 3 Vehicle Model Development

Level 3 vehicle models improve the Level 2 vehicle model by adjusting the LUTs according to real-world drive cycle data. The component signals on the controller area network (CAN) bus are logged using a C5 data logger from CrossChasm Technologies through the on-board diagnostic (OBD) II port. The modified LUTs then represent real-world vehicle performance as opposed to ideal simulation results. While Level 3 model development was attempted for this vehicle, the small data set and missing signals on the vehicle-side were insufficient to produce a model.

Chapter 7
Experimental

7.1 Equipment

7.1.1 Battery

The A123 AMP20 (Appendix D), 20 Ah pouch battery was selected for testing and modeling for three reasons. First of all, the AMP20 is a commercial battery. Secondly, the AMP20 is readily available in the laboratory. Finally, the AMP20 is used on-board the University of Waterloo Alternative Fuels Team (UWAFT) vehicle entered in the EcoCar 2 Challenge. Additionally, electrochemical models for the AMP20's $LiFePO_4$ chemistry have already been proposed and analyzed [43]. Thus, incorporating a degradation model into the existing models will reduce complexity and time requirements.

7.1.2 Maccor 4200 Series

The Maccor 4200 Series (Appendix E) was selected to conduct the characterization and reference performance testing of the AMP20 pouch batteries. The Maccor 4200 Series was selected due to its availability in the laboratory and its precision.

7.1.3 Hybrid Test Bench

Since the Maccor is a precise instrument, it is in high demand and unavailable for long-term degradation testing of the AMP20 batteries. Therefore, another test station was required to age the AMP20s. Fortunately, a Hybrid Test Bench (HTB) was developed in 2005 to experiment on battery and fuel cell technology for hybrid vehicle applications. While the bench is old and the resistance in the wiring has increased, it was determined that the HTB would satisfy the requirements of the degradation tests. Originally, the LabVIEW code controlling the HTB was designed to age the batteries on constant current charging and discharging profiles. Thus, the LabVIEW code was modified to test the batteries on drive cycles. The communication and sample times in LabVIEW were reduced to 150 ms in an attempt to match the drive cycle sample time of 100 ms. The communication time between LabVIEW and the devices are limited to about 130 ms, though error is more probable until the interval is increased to 150 ms; hence its selection. A full review of the LabVIEW code is available in Appendix F.

7.2 Characterization Test Procedure

The AMP20 is characterized on the Maccor 4200 Series battery cycler at its beginning of life (BOL) and EOL states according to the following test procedure:

1. Four channels are connected in parallel to increase current capability to 60 A while maintaining a voltage capability of 5 V.
2. The AMP20 experiences a CC 1C charge until a voltage of 3.6 V, at which point the AMP20 experiences a CV charge until a current of 2 A.
3. The AMP20 then rests for an hour to reach a state of equilibrium before the testing continues.
4. The AMP20 experiences a CCCV discharge at C/20 until a voltage of 2.0 V and current of 2 A is satisfied.
5. The AMP20 then rests for an hour to reach a state of equilibrium before the testing continues.
6. The AMP20 experiences a CCCV charge at C/20 until a voltage of 3.6 V and current of 2A is satisfied.
7. The AMP20 then rests for an hour to reach a state of equilibrium before the testing continues.
8. Steps 4 through 7 are repeated for charge and discharge rates of C/10, C/5, C/2, 1C, 2C, and 3C.

The OCP curve, maximum capacities, coulombic efficiencies and resistances are determined according to the calculations presented in Chapter 3.

During the degradation testing on the HBT, the battery is transferred to the Maccor after 50 cycles for reference performance testing according to the aforementioned procedure with the exception that the only current rates tested are C/5, C/2, 1C, and 2C.

7.3 Degradation Test Procedure

The degradation test is designed to determine the rate of degradation from driving the UDDS drive cycle (Figure 7.1a). However, the UDDS drive cycle is presented in vehicle speed and not in current. The UDDS duty cycle is determined by simulating the UWAFT EcoCar 2 vehicle on the UDDS with a battery pack of AMP20 pouch batteries (Figure 7.1b). The UWAFT EcoCar 2 vehicle previously modeled by Lo has been updated to reduce current requirements by increasing the number of cells in

parallel and reducing the percent regeneration capability [44]. Current requirements were reduced to satisfy the HTB current limitations.

(a) (b)

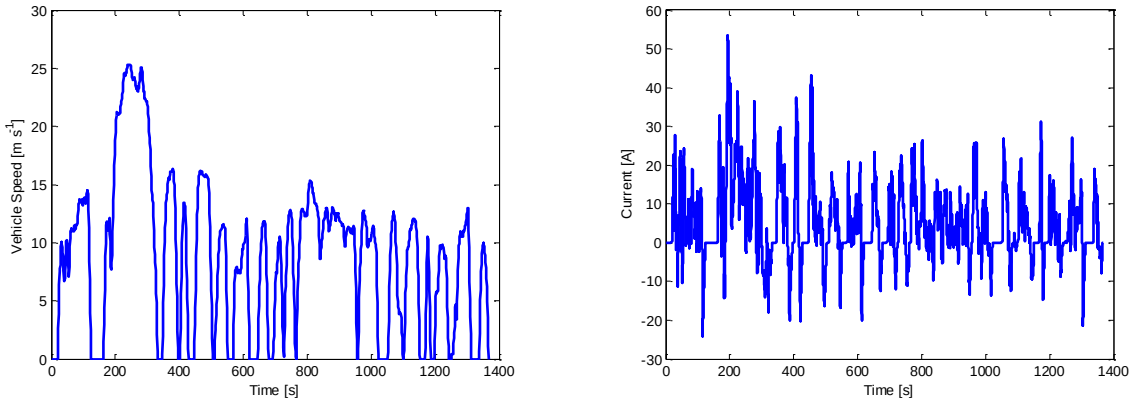

Figure 7.1 UDDS (a) drive cycle and (b) duty cycle

The AMP20 is degraded on the HTB according to the following test procedure:

1. The AMP20 is connected after testing from the Maccor.
2. The AMP20 is tested on the UDDS duty cycle until a voltage of 2.1 V.
    a. 2.1 V was selected as the lower limit since there is typically a 600 ms delay before the cycle switches to the next step, and therefore the voltage may drop below 2.1 V temporarily. It would be damaging if the battery voltage dropped below 2.0 V.
3. The AMP20 rests for 30 minutes to reach a state of equilibrium before the testing continues.
4. The AMP20 experiences a CC charge at 1C until a voltage of 3.6 V.
5. The AMP20 rests for 30 minutes to reach a state of equilibrium before the testing continues.
6. Steps 2 through 5 are repeated 49 times.

After the 50 cycles are completed, the AMP20 is disconnected from the HTB and connected to the Maccor for reference performance testing. The entire procedure is repeated until the battery reaches its EOL state or until the investigation ends.

7.4 Degradation Simulation Procedures

The semi-empirical SP degradation model is simulated on the duty cycles logged by the four Nissan Leafs according to the following test procedure:

1. The battery model undergoes a CC discharge at 1C from its initial, charged, state until the simulated battery voltage reaches a lower limit of 2 V.
2. The battery model undergoes a CC charge at 1C until the simulated battery voltage reaches an upper limit of 3.6 V.
3. The battery model undergoes a CC discharge at 1C until a simulated battery voltage of 2 V to determine the rated discharge capacity at 1C.
4. The battery model SOC is then charged to the SOC logged by the vehicle using a CC rate of 1C.
5. The battery model is simulated on one of the four selected duty cycles.
6. The battery model undergoes a CC charge at 1C until a simulated battery voltage of 3.6 V.
7. The battery model undergoes a CC discharge at 1C until a simulated battery voltage of 2 V.
8. The degradation results are normalized and extrapolated to predict annual degradation.
9. Steps 2 and 3 are repeated to measure the simulated battery capacity fade.
10. Steps 4 through 9 are repeated seven times to predict degradation over eight years.

Since the Nissan Leaf uses a battery pack rated at 66.2 Ah, the logged current signal is converted to a C-rate signal, then converted back to a current signal for the AMP20 rated capacity of 20 Ah. Therefore, the degradation results are assuming a pack of AMP20 pouch batteries were onboard the Nissan Leaf. These results do not represent degradation of the Nissan Leaf battery pack.

Chapter 8
Battery Degradation Model Development

8.1 Single Particle Degradation Model

8.1.1 Introduction

The SP model is one of the simplest representations of an electrochemical cell (Figure 8.1). The SP model's geometry is determined from the assumption that the electrodes are an accumulation of perfectly spherical particles.

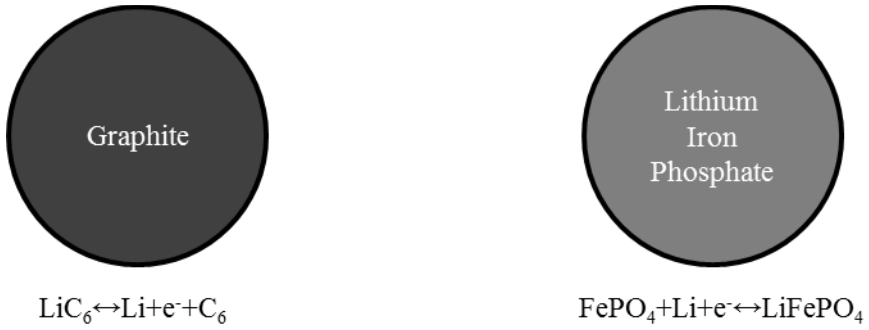

Figure 8.1 SP model of a graphite/$LiFePO_4$ battery; reactions from left to right for battery discharge

The particles in the SP model do not interact directly, as they would in the other more sophisticated models such as the P2D model. In models like the P2D model, the entire system must be solved simultaneously; however the individual electrodes can be modeled separately in the SP model.

At first, it may not seem beneficial to be able to separate the electrode models since they need to be solved simultaneously to predict battery voltage in the following equation; where V_{cell} is the cell potential, V_{LFP} is the LFP electrode potential, and V_G is the graphite electrode potential.

$$V_{cell} = V_{LFP} - V_G \tag{8.1}$$

Nonetheless, it might be beneficial to separate the electrode models from the SP model for predicting degradation in vehicle battery packs. First of all, the most significant degradation is attributed to SEI growth at the interface between the negative electrode material and electrolyte. Secondly, electric powertrains use a high voltage battery pack composed of a graphite negative electrode and an

unknown positive electrode material. Ultimately, the SP model of the graphite negative electrode and the degradation equations for that electrode should be able to predict battery aging without knowing the positive electrode material. Therefore, the SP degradation model of an automotive-grade graphite electrode should be applicable to all battery packs onboard vehicles today. It must be noted, however, that the less sophisticated SP model will not elucidate the inner processes of the battery as a more complex P2D model would.

8.1.2 Governing Equations

As it was previously state, the SP model does not model the interactions between electrode active material particles. In other words, the SP model does not consider ion transport limitations in the electrolyte or ohmic drop across the solid-phase material in the electrodes [45]. In addition to these exclusions, the two-phase nature of LFP is neglected and assumed to follow conventional solid-state diffusion equations [45]. The governing equations for the SP model used in this investigation were developed by Safari *et al.* in separate papers, but have been compiled into an SP degradation model [27, 45, 46].

The current density in the active material particles is related to the rate of lithium intercalation through the Butler-Volmer equation; where n/p is either the negative or positive electrode, $i_{n/p}^{int}$ is the intercalation current density with respect to the total surface area of the particles, F is Faraday's constant (96487 C mol^{-1}), $k_{n/p}^{0}$ is the electrochemical reaction rate constant of the intercalation process, c_e is the electrolyte concentration, $c_{n/p}^{max}$ is the maximum concentration of lithium in the particles, x_s (y_s for positive electrode) is the dimensionless solid-state lithium surface concentration of the negative electrode particles, β is the charge-transfer coefficient, R is the gas constant (8.314 J mol^{-1} K^{-1}), T is the absolute temperature, and $\eta_{n/p}$ is the surface overpotential.

$$i_{n/p}^{int} = F k_{n/p}^{0} c_e^{1-\beta} c_{n/p}^{max} (1 - x_s)^{1-\beta} x_s^{\beta} \left[\exp\left(\frac{(1-\beta)F}{RT} \eta_{n/p} \right) - \exp\left(-\frac{\beta F}{RT} \eta_{n/p} \right) \right] \quad (8.2)$$

The surface overpotential for the negative electrode is present below, where Φ_n is the solid-phase potential, U_n is the open circuit potential, R_{SEI} is the SEI film resistance, and i_n^t is the total current density of the negative electrode.

$$\eta_n = \Phi_n - U_n - R_{SEI} i_n^t \quad (8.3)$$

The surface overpotential for the positive electrode is slightly different, where R_p is the reactive resistance of the positive electrode particles.

$$\eta_p = \Phi_p - U_p - R_p i_p^{int} \tag{8.4}$$

As is evident in equations (8.2) through (8.4), the intercalation current density for the positive electrode represents the entirety of current flowing through the electrode while the intercalation current density of the negative electrode is different. The difference is described by a parasitic reaction consuming some of the overall current; where i_s is the parasitic current density over the total surface area of the negative electrode particles.

$$i_n^t = i_n^{int} + i_s \tag{8.5}$$

The parasitic reaction kinetics are described by the Tafel equation for the negative electrode, where n is the number of electrons in the parasitic reaction, k_{fs}^{app} is the apparent rate constant of the side reaction, and β_s is the charge-transfer coefficient of the side reaction.

$$i_s = -nFk_{fs}^{app}\exp\left(\frac{-n\beta_s F}{RT}(\Phi_n - R_{SEI} i_n^t)\right) \tag{8.6}$$

The SEI thickness and resistance are updated according to the following two equations; where δ_{SEI} is the SEI film thickness, V_{SEI} is the molar volume of the SEI film, R_{SEI}^0 is the initial resistance of the SEI film, and κ_{SEI} is the ionic conductivity of the SEI film.

$$\frac{d\delta_{SEI}}{dt} + \frac{V_{SEI} i_s}{nF} = 0 \tag{8.7}$$

$$R_{SEI} - R_{SEI}^0 - \frac{\delta_{SEI}}{\kappa_{SEI}} \tag{8.8}$$

Battery current is oppositely related to the electrodes, where $L_{n/p}$ is the electrode thickness, and $a_{n/p}$ is the specific interfacial area per unit volume of electrode.

$$I = L_n a_n i_n^t \tag{8.9}$$

$$I = -L_p a_p i_p^{int} \tag{8.10}$$

The Butler-Volmer equation describing the intercalation kinetics within the electrodes also depends on the lithium concentration within the particles. A three-parameter, fourth-order polynomial approximation of Fick's law for the lithium diffusion into a spherical particle was proposed by Subramanian *et al*. [47]. The first equation describes the mean lithium concentration in the particle; where $\bar{x}$ (or $\bar{y}$ for the positive electrode) is the dimensionless mean solid-state lithium concentration inside the particles, t is time, and $r_{n/p}$ is the particle radius.

$$\frac{d\bar{x}}{dt} + \frac{3i_{n/p}^{int}}{Fr_{n/p}c_{n/p}^{max}} = 0 \tag{8.11}$$

The second equation describes the flux of lithium within the particle; where $\bar{q}_{n/p}$ is the dimensionless volume-averaged flux of lithium concentration in the particle, and $D_{n/p}$ is the solid-state lithium diffusion coefficient in the particle.

$$\frac{d\bar{q}_{n/p}}{dt} + \frac{30D_{n/p}\bar{q}_{n/p}}{{r_{n/p}}^2} + \frac{45i_{n/p}^{int}}{2Fr_{n/p}c_{n/p}^{max}} = 0 \tag{8.12}$$

While this equation holds for the negative electrode, the diffusion coefficient is concentration-dependent in the positive electrode according to the following relationship; where D_p^0 is the solid-state diffusion coefficient at a completely delithiated state, and m and p are empirically fit constants.

$$D_p = \frac{D_p^0}{(1 - m\bar{y})^p} \tag{8.13}$$

The final approximation relates the first two equations with the particle surface concentration.

$$35(x_s - \bar{x}) - 8\bar{q}_{n/p} + \frac{r_{n/p}}{FD_{n/p}c_{n/p}^{max}} = 0 \tag{8.14}$$

A summary of the governing equations is presented below in Table 8.1.

Table 8.1 SP degradation model governing equations for graphite and LFP electrodes

Graphite Electrode		LFP Electrode	
$i_n^{int} = Fk_n^0 c_e^{1-\beta} c_n^{max}(1 - x_s)^{1-\beta} x_s^{\beta} \left[\exp\left(\frac{(1-\beta)F}{RT}\eta_n\right) - \exp\left(-\frac{\beta F}{RT}\eta_n\right)\right]$	(8.2)	$i_p^{int} = Fk_p^0 c_e^{1-\beta} c_p^{max}(1 - y_s)^{1-\beta} y_s^{\beta} \left[\exp\left(\frac{(1-\beta)F}{RT}\eta_p\right) - \exp\left(-\frac{\beta F}{RT}\eta_p\right)\right]$	(8.2)
$\eta_n = \Phi_n - U_n - R_{SEI} i_n^t$	(8.3)	$\eta_p = \Phi_p - U_p - R_p i_p^{int}$	(8.4)
$I = L_n a_n i_n^t$	(8.9)	$I = -L_p a_p i_p^{int}$	(8.10)
$\frac{d\bar{x}}{dt} + \frac{3 i_n^{int}}{F r_n c_n^{max}} = 0$	(8.11)	$\frac{d\bar{y}}{dt} + \frac{3 i_p^{int}}{F r_p c_p^{max}} = 0$	(8.11)
$\frac{d\bar{q}_n}{dt} + \frac{30 D_n \bar{q}_n}{{r_n}^2} + \frac{45 i_n^{int}}{2F r_n c_n^{max}} = 0$	(8.12)	$\frac{d\bar{q}_p}{dt} + \frac{30 D_p \bar{q}_p}{{r_p}^2} + \frac{45 i_p^{int}}{2F r_p c_p^{max}} = 0$	(8.12)
		$D_p = \frac{D_p^0}{(1 - m\bar{y})^p}$	(8.13)
$35(x_s - \bar{x}) - 8\bar{q}_n + \frac{r_n}{F D_n c_n^{max}} = 0$	(8.14)	$35(y_s - y) - 8\bar{q}_p + \frac{r_p}{F D_p c_p^{max}} = 0$	(8.14)

Degradation Equations of the Graphite Electrode	
$i_s = -nFk_{fs}^{app} \exp\left(\frac{-n\beta_s F}{RT}(\Phi_n - R_{SEI} i_n^t)\right)$	(8.6)
$\frac{d\delta_{SEI}}{dt} + \frac{V_{SEI} i_s}{nF} = 0$	(8.7)
$R_{SEI} - R_{SEI}^0 - \frac{\delta_{SEI}}{\kappa_{SEI}}$	(8.8)
$i_n^t = i_n^{int} + i_s$	(8.5)

8.1.3 Simulink SP Degradation Model

Although Safari *et al.* used MATLAB's *fsolve* function to solve the set of equations in Table 8.1, the simulation time was too long. Therefore the set of equations were designed into a Simulink model that runs significantly faster.

A high level review of the model (Figure 8.2) contains the input block referencing the time and current variables in the MATLAB workspace. The time and current are then fed into the negative electrode and positive electrode blocks. Furthermore, the time and current input is used to determine the discharge capacity. The potential outputs from the electrode blocks are used to calculate the battery voltage. If the battery voltage exceeds 3.6 V or drops below 2 V, the simulation is stopped.

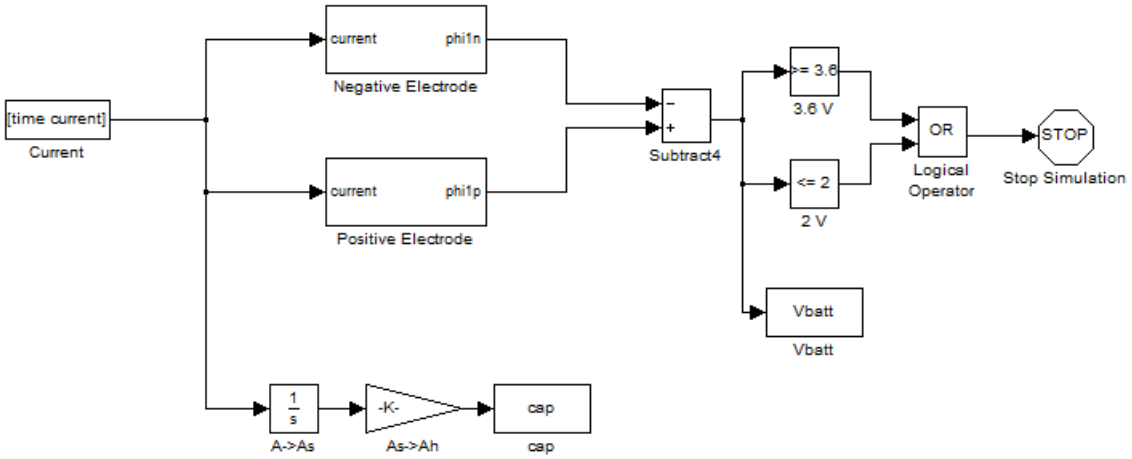

Figure 8.2 High level view of the SP degradation model in MATLAB Simulink

Within the negative electrode block (Figure 8.3), the equations defined in Table 8.1 are virtually arranged and connected in an algebraic loop that MATLAB Simulink will solve for each time step.

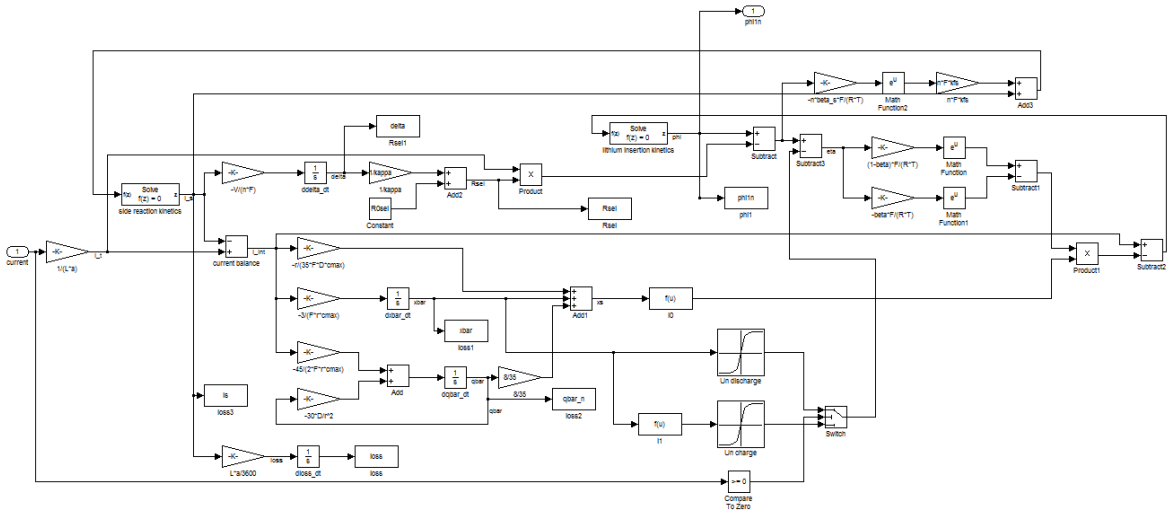

Figure 8.3 Negative electrode calculation block

The positive electrode block is nearly the same with a few discrepancies surrounding the LFP particle resistances (Figure 8.4).

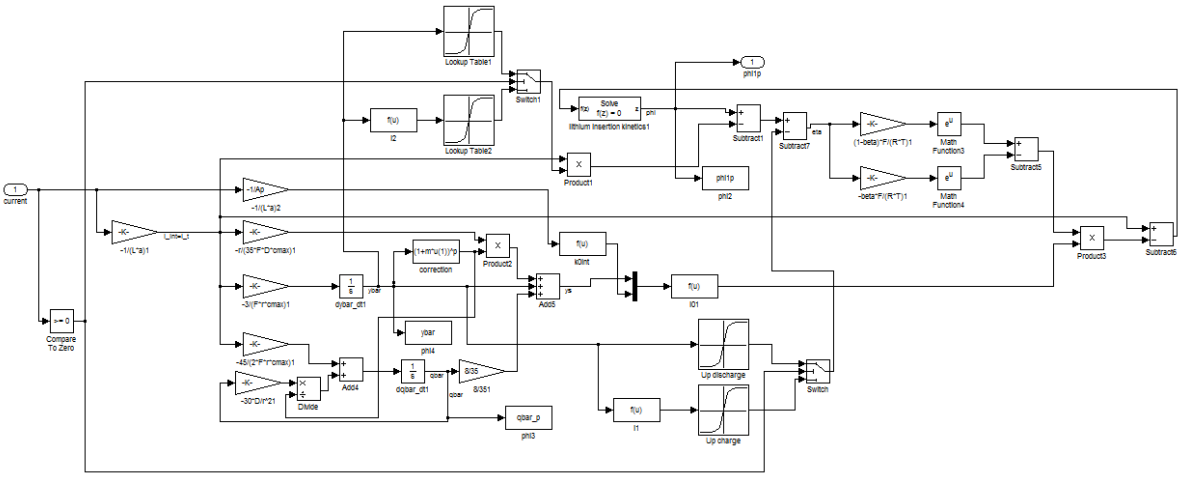

Figure 8.4 Positive electrode calculation block

8.2 SP Degradation Model Parameter Fitting

8.2.1 Open Circuit Potential

The OCP curves used in the SP degradation model are fit to C/50 galvanostatic charge and discharge test data from graphite/Li and LFP/Li half-cell coin cells constructed from A123 AMP20 pouch

batteries. It is assumed that a current rate of C/50 is too small to impart a significant disturbance from the OCP of the battery. The charge and discharge data is kept separate due to the hysteresis the A123 cells experience between charging and discharging (Figure 8.5).

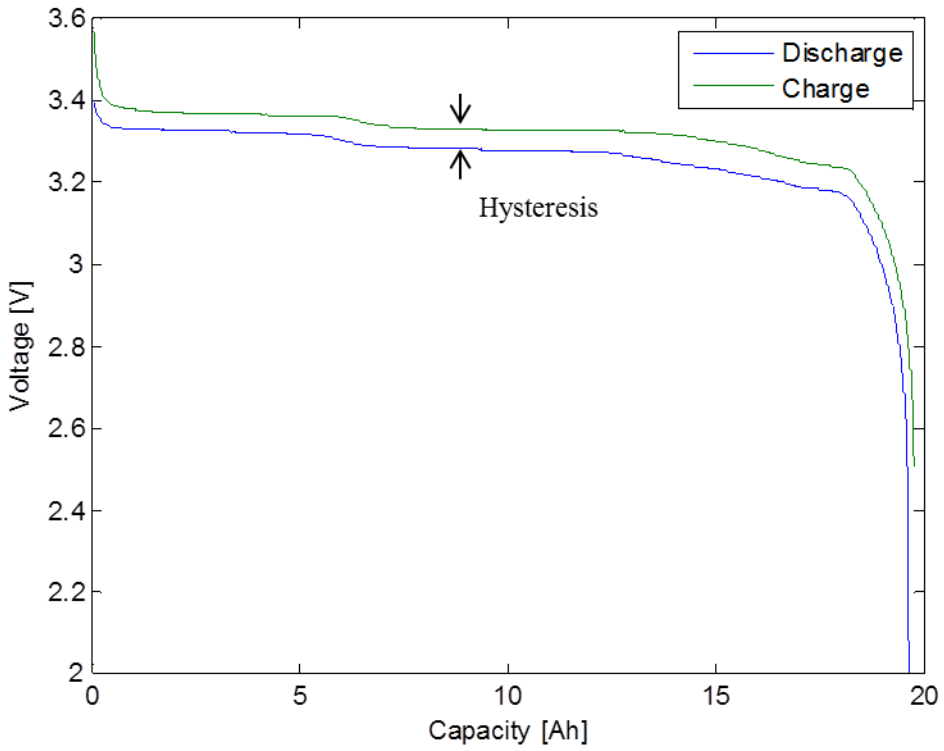

Figure 8.5 A123 AMP20 hysteresis for a current rate of C/50

Instead of fitting the OCP data to the models defined by Safari and Delacourt, the data was formatted into a Simulink LUT to increase accuracy and reduce simulation time (Figure 8.6) [45]. The OCP models were originally fit to the data; however the model failed to fit the final deintercalation stage of the graphite electrode.

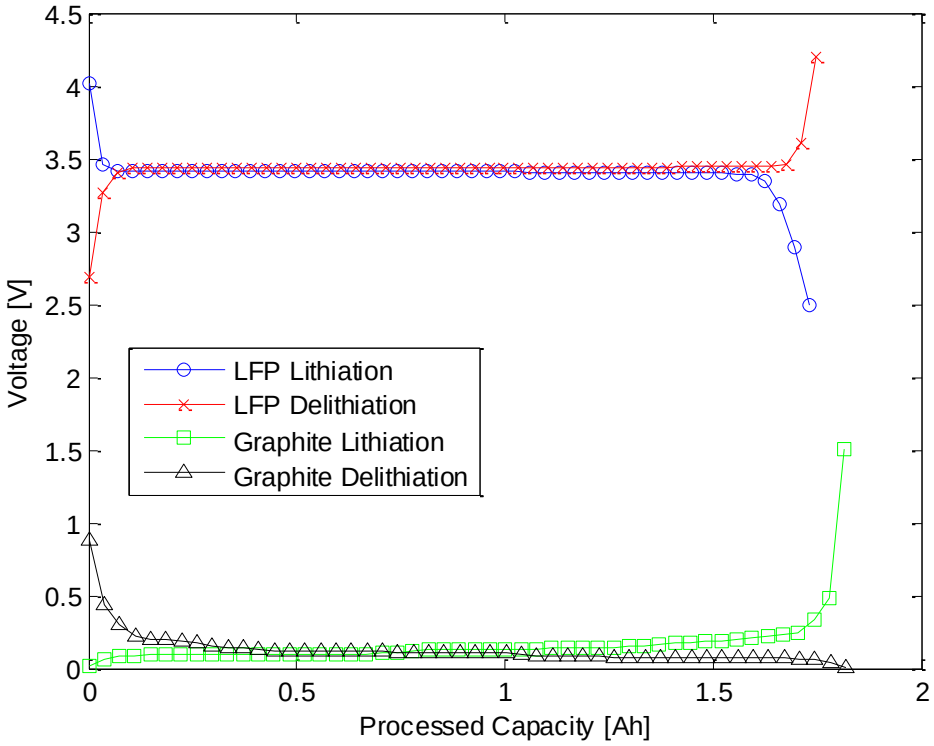

Figure 8.6 Charge and discharge electrode OCP data

The OCP operating ranges of the electrodes must be determined to fit the OCP data of the AMP20 pouch battery. The operating range for each electrode is determined using dV/dQ plots. Essentially, any changes in the voltage profile during charge or discharge will yield a peak in the dV/dQ plot. The LFP/Li half-cell and graphite/Li half-cell dV/dQ curves are plotted against the pouch battery dV/dQ curve to determine the operating ranges for a CC discharge (Figure 8.7).

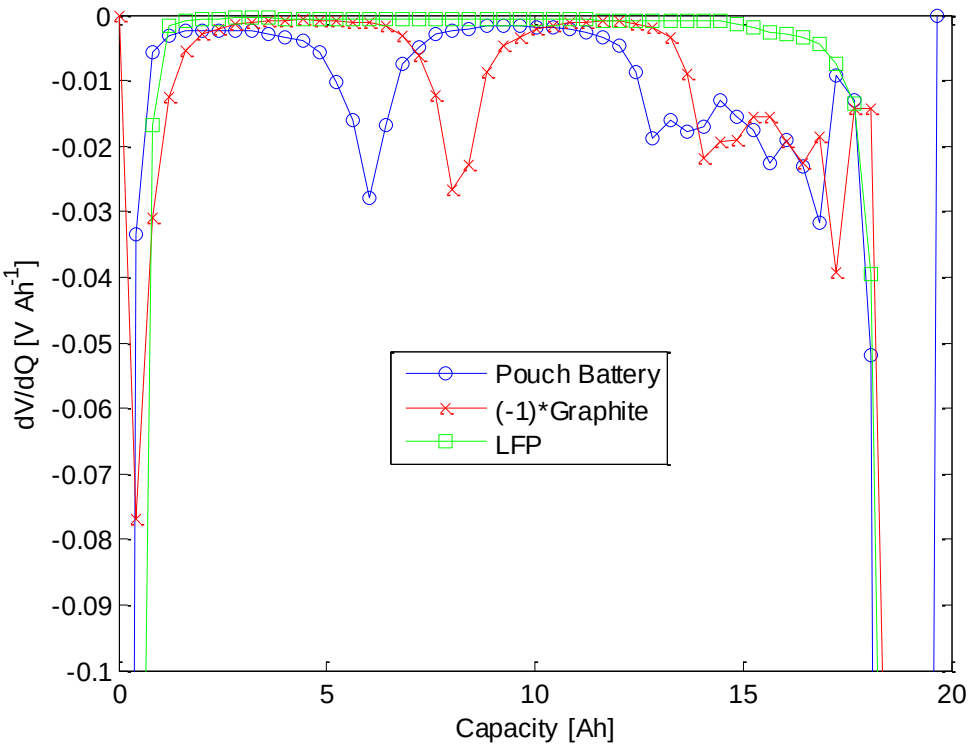

Figure 8.7 dV/dQ plot for a discharging battery

It is evident that the deintercalation peaks of the pouch battery are attributed to the graphite/Li half-cell; or the negative electrode. The graphite/Li dV/dQ curve can thus be shifted and stretched to satisfy those peaks. Although it is more difficult to see, the LFP/Li half-cell is attributed to the initial slope of the pouch battery dV/dQ curve. The LFP/Li dV/dQ curve is also shifted and stretched until the calculated dV/dQ curve matches that of the pouch battery (Figure 8.8).

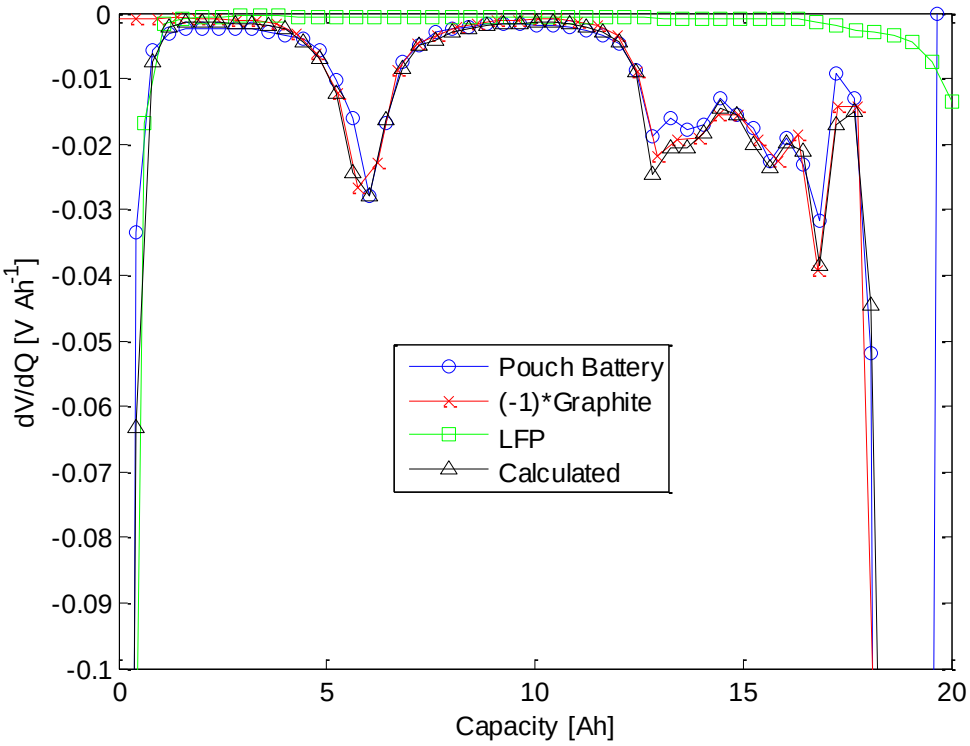

Figure 8.8 A fitted dV/dQ plot for a discharging battery

This fitting method is easy to implement and provides accurate results when comparing the voltage responses for a given charge or discharge (Figure 8.9).

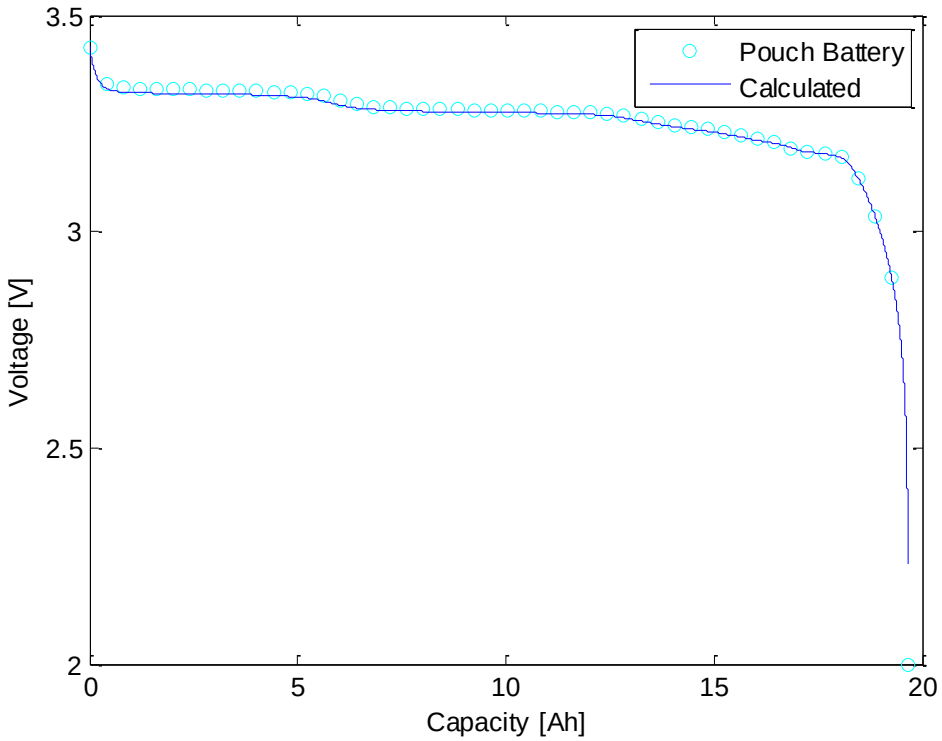

Figure 8.9 Voltage responses for a discharging battery

The difference between the measured cell voltage response and the calculated voltage response can be attributed to the fact that the calculated voltage is determined from 2mAh half-cell coin cell data while the cell voltage is measured from a 20Ah pouch battery. These results indicate that the low-current results of the coin cells can be adequately scaled to estimate pouch battery performance.

The process presented for discharging a cell is also applied to charging a cell with similar results (Figure 8.10, Figure 8.11). Once the OCP curves are fitted, the model parameters can be determined to simulate battery performance under various loads.

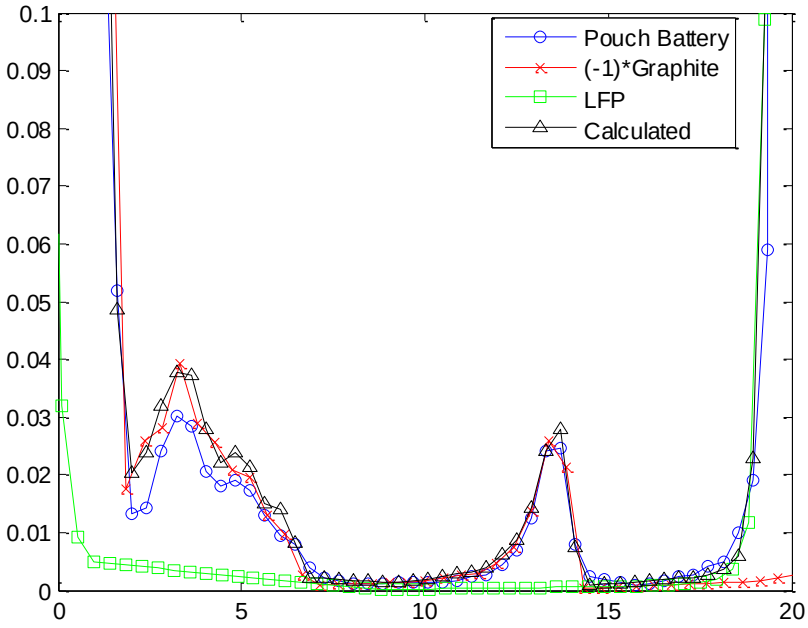

Figure 8.10 A fitted dV/dQ plot for a charging battery

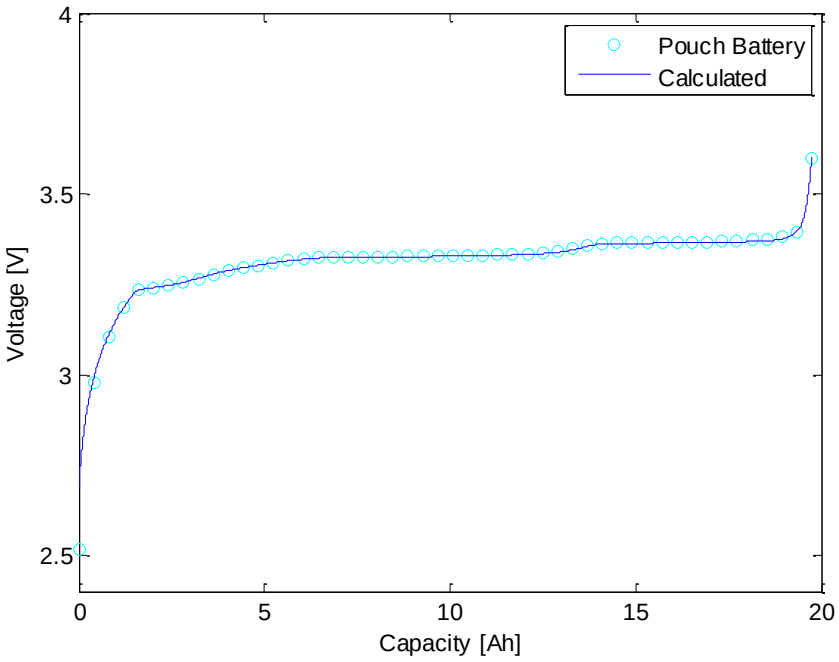

Figure 8.11 Voltage responses for a charging battery

8.2.2 Single-Particle Model Parameters

The single-particle model presented previously, developed for LiFePO4 chemistry based on work by Safari and Delacourt [45], was used to represent the A123 AMP20 pouch batteries. The model parameters have been altered to more accurately predict the AMP20's performance according to the current being applied to the battery. The fitted model parameters are presented below (Table 8.2) along with the simulated results compared to the experimental data (Figure 8.12, Figure 8.13). It is evident that a good fit has been achieved.

Table 8.2 Fitted single-particle model parameters for each electrode

	Graphite Electrode		**LFP Electrode**	
Parameter	**Symbol**	**Value**	**Symbol**	**Value**
Thickness [m]	L_n	34×10^{-6} [a]	L_p	70×10^{-6} [a]
Area [m^2]	A_n	1.4602 [m]	A_p	1.3996 [m]
Volume fraction	ε_n	0.56 [a]	ε_p	0.435 [a]
Particle radius [m]	r_n	3.5×10^{-6} [a]	r_p	36.5×10^{-9} [a]
Maximum solid-phase lithium concentration [mol m^{-3}]	$C_{max,n}$	31900 [f]	$C_{max,p}$	19998 [f]
Charge transfer coefficient	β_n	0.5 [a]	β_p	0.5 [a]
Solid-state lithium diffusion coefficient	D_n^0	2×10^{-14} [a]	D_p	1.18×10^{-18} [a]
Intercalation rate constant [$m^{2.5}$ $mol^{-0.5}$ s^{-1}]	K_n^0	8.19×10^{-12} [a]	K_p^0	5×10^{-12} [a]
Salt concentration in the liquid phase [mol m^{-3}]	C_e	1000 [a]	C_e	1000 [a]
SEI film resistance [Ω m^2]	R_{sei}	0.0047 [f]		
	Empirical Parameters			
	m	**p**	**$R_{p,c}$**	**$R_{p,d}$**
Values	1 [a]	1.6 [a]	See Figure 8.14 [f]	

*a = according to [45], m = measured, f = fitted

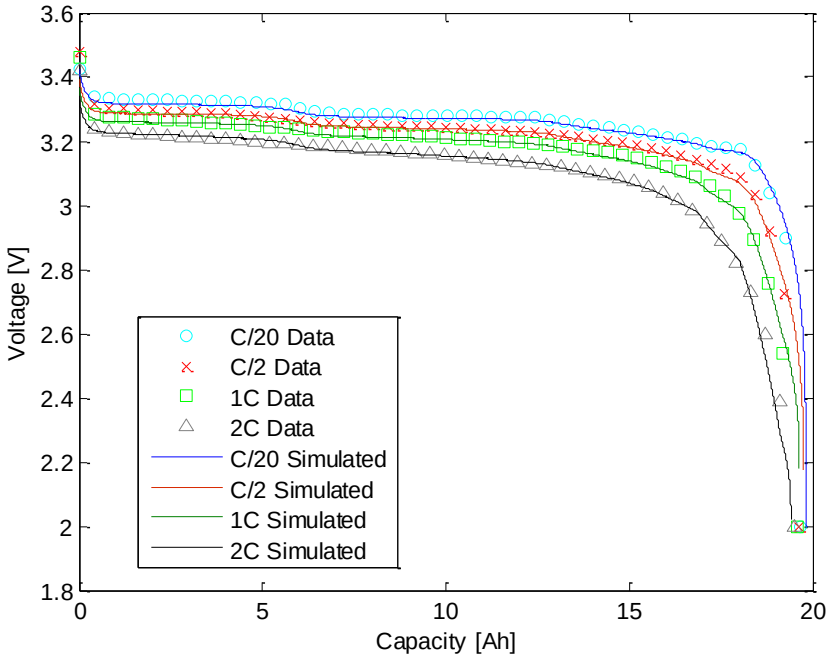

Figure 8.12 Fitted SP model of AMP20 compared to experimental discharge data

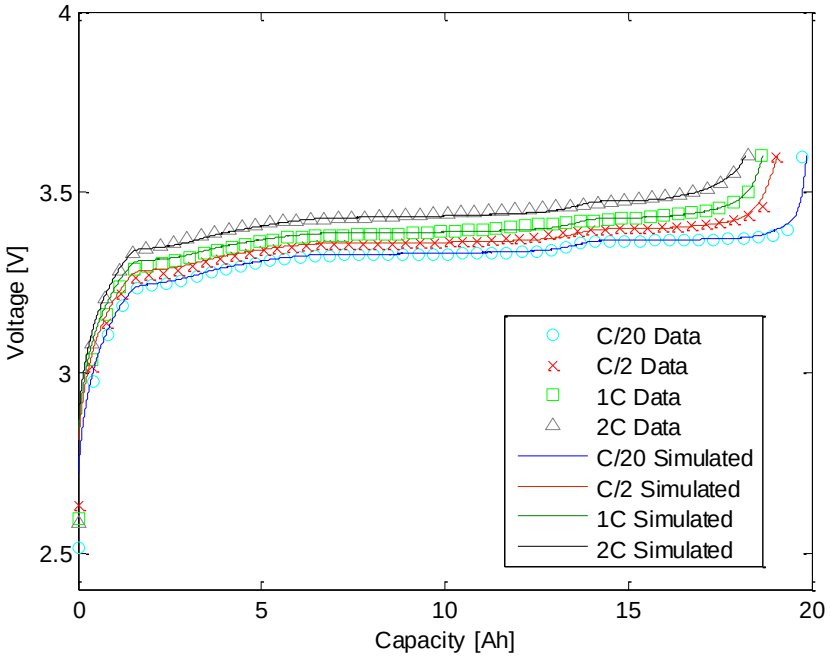

Figure 8.13 Fitted SP model of AMP20 compared to experimental charge data

The SP model in this work differs from the one presented by Safari and Delacourt [45]. Safari and Delacourt account for multiple LFP particle groups on the positive electrode by determining the particle size distribution and the resistances associated with each particle group. The model presented in this work assumes one LFP particle group when considering the governing equations. To account for the changing resistance of the particles since several particle groups do exist in reality, the LFP particle resistance is assumed to change with its level of lithiation. Such a resistance change was empirically fit and it was determined that the resistance was different for charging and discharging currents but did not depend on the magnitude of the current (Figure 8.14).

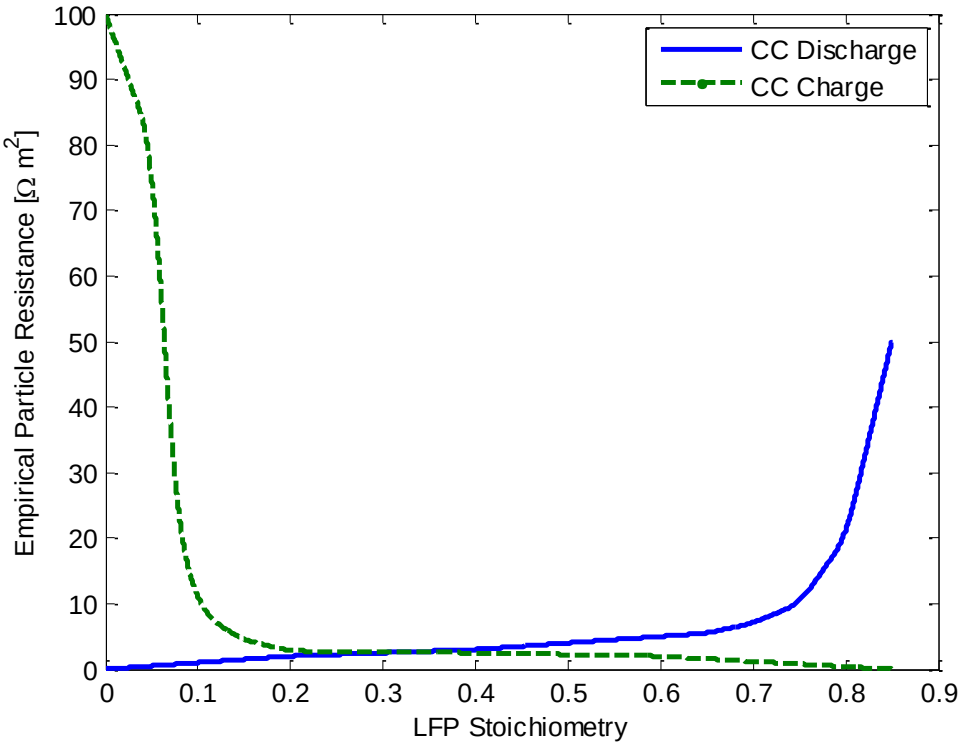

Figure 8.14 Empirically fit LFP particle resistance according to the level of lithiation

Using an empirically fit LFP particle resistance LUT in the model improves the accuracy of the SP model for the AMP20 pouch battery in particular; however such an empirical fit reduces the robustness of the model. Therefore, this model can likely be used on other AMP20 pouch batteries with limited parameter alterations; however this model should not be used on other $LiFePO_4$ without caution or refitting of the parameters.

8.2.3 Degradation Model Parameters

It was determined during the degradation parameter fitting process that the fitted model of galvinostatic data did not fit the duty cycle data as well. To adjust accordingly, the discharge LFP particle resistance values (Figure 8.14) were increased by 3 Ω m^2. It was also discovered that the hysteresis was insignificant during the degradation cycling and to adjust to fit the data, the LFP charging OCP data was empirically lowered by 50 mV. Finally, the resulting LFP OCP curve was also empirically lowered by 50 mV. These changes provided a model that fit the variable current conditions well. Therefore, the model previously presented is used for galvanostatic cycling while these adjustments are used in the degradation cycling.

The battery degradation model parameters were fit to the experimental data Table 8.3). Degradation data from cycling the AMP20 on the UDDS duty cycle is used since the US06 duty cycle data is insufficiently dense enough to generate a fit. The resulting degradation prediction is presented in Figure 8.15 for capacity fade and impedance rise.

Table 8.3 Fitted battery degradation parameters at the graphite electrode

Parameters	Symbol	Values
SEI molar volume [m^3 mol^{-1}]	V_{sei}	$5x10^{-5}$ [a]
SEI ionic conductivity [S m^{-1}]	κ_{sei}	$5.2x10^{-7}$ [f]
SEI charge transfer coefficient	β_s	0.5 [a]
Parasitic rate constant [mol m^{-2} s^{-1}]	K_{fs}^0	$4.3x10^{-10}$ [f]

*a = according to [45], m = measured, f = fitted

(a)

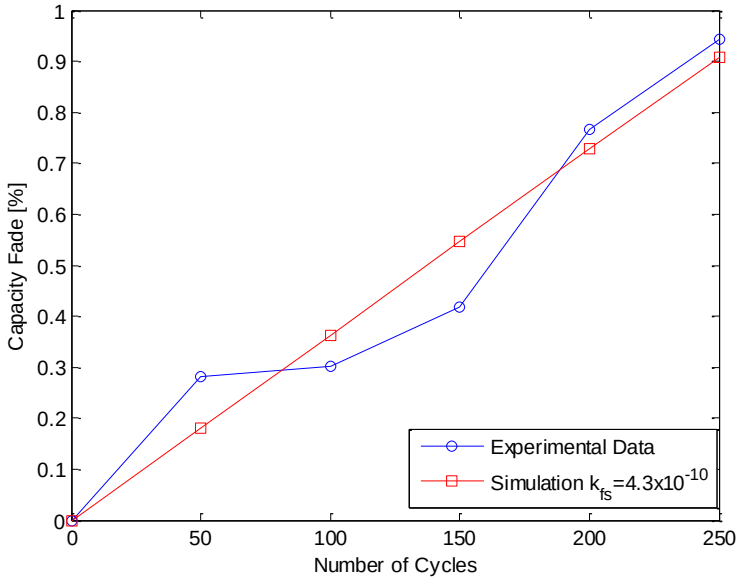

(b)

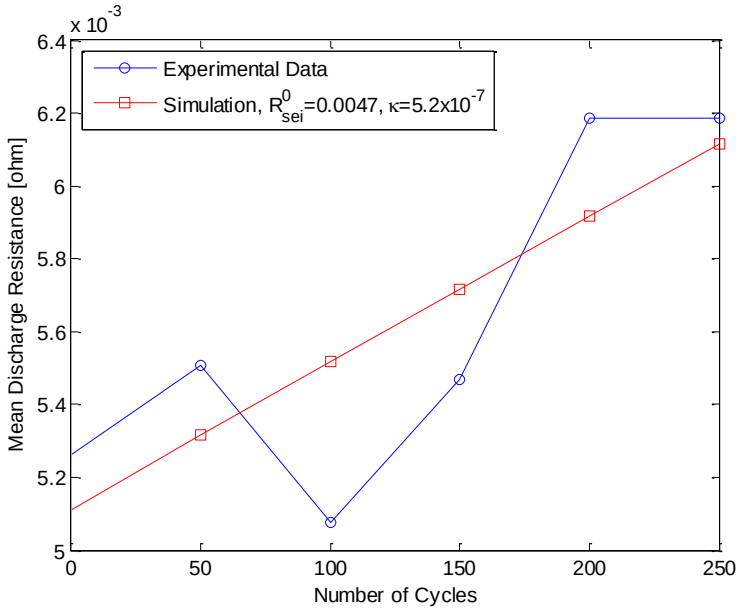

Figure 8.15 Simulated (a) capacity fade and (b) impedance rise compared to experimental data

The experimental capacity loss data does not appear linear, yet there is a linear fit from the SP degradation model. It is possible that the first 50 cycles is a formation period, followed by a 50 cycle plateau before degrading further. It is unlikely that this is the case due to the 5-cycle preconditioning and having run 90 duty cycles while tuning of the HTB. Thus, the formation period is likely to have been completed and the variability in experimental data is random. These assumptions could be confirmed with more test data in future work. Now that the semi-empirical SP degradation model has been successfully fit to the experimental data, it can be used to analyze how battery degradation changes with drive cycle and driver behaviour. It can also be integrated into a vehicle model to predict real-time degradation in future work.

Chapter 9
Analysis and Discussion

9.1 Sensitivity Analysis

The parasitic reaction of the SEI film formation is represented by the Tafel equation, presented again below.

$$i_s = -nFk_{fs}^{app}\exp\left(\frac{-n\beta_s F}{RT}(\Phi_n - R_{SEI}i_n^t)\right) \tag{8.6}$$

The parasitic current density, i_s, is a function of the negative electrode potential, Φ_n, the SEI film resistance, R_{SEI}, and the total negative electrode current density, i_n^t. With respect to a duty cycle, the negative electrode potential depends on the SOC, the SEI film resistance represents the battery history or age, and the negative electrode current density is the battery current of the duty cycle. These variables can be assessed further by determining their partial derivatives while holding the other variables constant.

$$\left.\frac{\partial i_s}{\partial \Phi_n}\right|_{R_{SEI},i_n^t} = \frac{F^2\beta_s k_{fs}^{app} n^2}{RT} exp\left(\frac{-n\beta_s F}{RT}(\Phi_n - R_{SEI}i_n^t)\right) \tag{9.1}$$

$$\left.\frac{\partial i_s}{\partial \mathrm{R}_{SEI}}\right|_{\Phi_n,i_n^t} = -\frac{F^2\beta_s k_{fs}^{app} n^2 i_n^t}{RT} exp\left(\frac{-n\beta_s F}{RT}(\Phi_n - R_{SEI}i_n^t)\right) \tag{9.2}$$

$$\left.\frac{\partial i_s}{\partial i_n^t}\right|_{\Phi_n,R_{SEI}} = -\frac{F^2\beta_s k_{fs}^{app} n^2 R_{SEI}}{RT} exp\left(\frac{-n\beta_s F}{RT}(\Phi_n - R_{SEI}i_n^t)\right) \tag{9.3}$$

The interpretation of these equations is to say that a positive change in negative electrode potential yields a positive change in the parasitic current density, a positive change in the SEI film resistance yields a negative change in the parasitic current density, and a positive change in the negative electrode current density yields a negative change in the parasitic current density. These changes also depend on the present state of the system, which can impact their effects on the parasitic current density. The partial derivatives can be compared to each other to determine which variables cause the most significant changes in parasitic current density.

$$\left.\frac{\partial i_s}{\partial \Phi_n}\right|_{R_{SEI},i_n^t} = -\frac{1}{i_n^t}\left.\frac{\partial i_s}{\partial \mathrm{R}_{SEI}}\right|_{\Phi_n,i_n^t} = -\frac{1}{R_{SEI}}\left.\frac{\partial i_s}{\partial i_n^t}\right|_{\Phi_n,R_{SEI}} \tag{9.4}$$

The following conditions are possible for the system.

1. If $\left|-\frac{1}{i_n^t}\right| < 1$, or $|-i_n^t| > 1$, then $\left.\frac{\partial i_s}{\partial \Phi_n}\right|_{R_{SEI},i_n^t} < \left.\frac{\partial i_s}{\partial \mathrm{R}_{SEI}}\right|_{\Phi_n,i_n^t}$
2. If $\left|-\frac{1}{R_{SEI}}\right| < 1$, or $|-R_{SEI}| > 1$, then $\left.\frac{\partial i_s}{\partial \Phi_n}\right|_{R_{SEI},i_n^t} < \left.\frac{\partial i_s}{\partial i_n^t}\right|_{\Phi_n,R_{SEI}}$
3. If $\left|-\frac{1}{i_n^t}\right| < \left|-\frac{1}{R_{SEI}}\right|$, or $|-i_n^t| > |-R_{SEI}|$, then $\left.\frac{\partial i_s}{\partial \mathrm{R}_{SEI}}\right|_{\Phi_n,i_n^t} > \left.\frac{\partial i_s}{\partial i_n^t}\right|_{\Phi_n,R_{SEI}}$

The first condition states that if the magnitude of the negative electrode current density is greater than 1 A m^{-3} (*c.a.* 24 A), then a change in negative electrode potential has less impact than a change in SEI resistance. The second condition states that if the magnitude of the SEI resistance is greater than 1 Ω m^2 , then a change in negative electrode potential has less impact than a change in negative electrode current density. The third condition states that if the magnitude of the negative electrode current density is greater than the magnitude of the SEI resistance, then a change in SEI resistance has more impact than a change in the negative electrode current density. These conclusions can be categorized into a set of operating conditions.

For low current operation at the BOL, a change in potential or SOC will impact the degradation rate the most, seconded by a change in age, followed by a change in current.

$$\left.\frac{\partial i_s}{\partial \Phi_n}\right|_{R_{SEI},i_n^t} > \left.\frac{\partial i_s}{\partial \mathrm{R}_{SEI}}\right|_{\Phi_n,i_n^t} > \left.\frac{\partial i_s}{\partial i_n^t}\right|_{\Phi_n,R_{SEI}} \tag{9.5}$$

For high current operation at the BOL, a change in SEI resistance will impact the degradation rate the most, seconded by a change in SOC, followed by a change in current.

$$\left.\frac{\partial i_s}{\partial \mathrm{R}_{SEI}}\right|_{\Phi_n,i_n^t} > \left.\frac{\partial i_s}{\partial \Phi_n}\right|_{R_{SEI},i_n^t} > \left.\frac{\partial i_s}{\partial i_n^t}\right|_{\Phi_n,R_{SEI}} \tag{9.6}$$

For low current operation at the EOL, a change in SOC will impact the degradation rate the most, seconded by a change in current, followed by a change in age.

$$\left.\frac{\partial i_s}{\partial \Phi_n}\right|_{R_{SEI},i_n^t} > \left.\frac{\partial i_s}{\partial i_n^t}\right|_{\Phi_n,R_{SEI}} > \left.\frac{\partial i_s}{\partial \mathrm{R}_{SEI}}\right|_{\Phi_n,i_n^t} \tag{9.7}$$

Finally, for high current operation at the EOL, a change in current will impact the degradation rate the most, seconded by a change in the age, followed by a change in the SOC.

$$\left.\frac{\partial i_s}{\partial i_n^t}\right|_{\Phi_n,R_{SEI}} > \left.\frac{\partial i_s}{\partial \mathrm{R}_{SEI}}\right|_{\Phi_n,i_n^t} > \left.\frac{\partial i_s}{\partial \Phi_n}\right|_{R_{SEI},i_n^t} \tag{9.8}$$

The effects of current, initial SOC, DOD, and SEI resistance are presented below (Figure 9.1) by applying a negative current to the battery followed by an equivalent positive current to ensure the overall change in SOC is zero. The results are plotted against the processed capacity, which is the total number of coulombs into and out of the battery. Thus, 2 Ah processed capacity means 1 Ah of charging followed by 1 Ah of discharging for a 5% DOD on a 20 Ah battery.

(a)

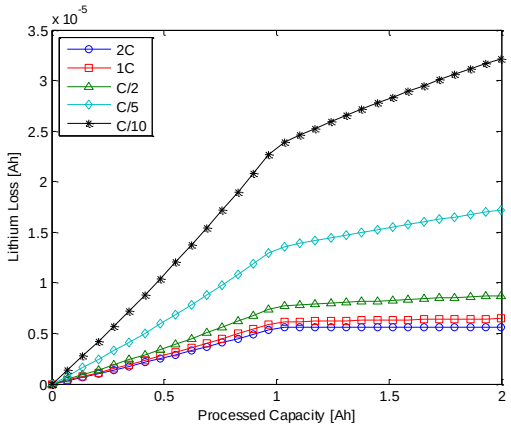

(b)

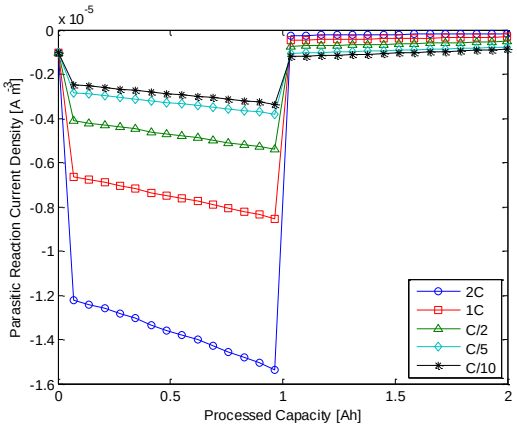

(c)

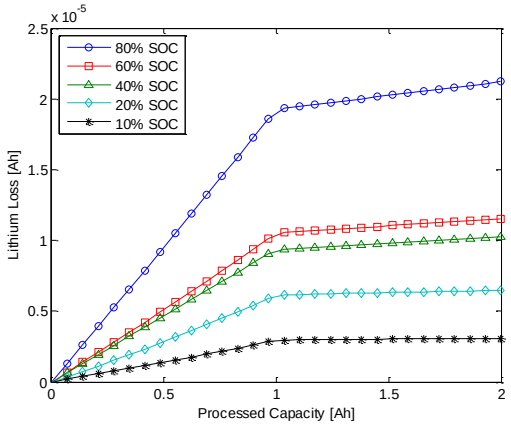

(d)

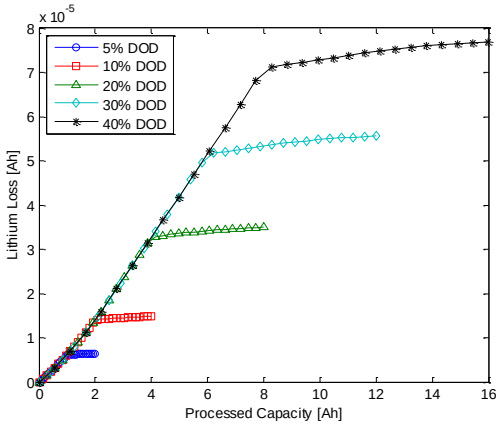

Figure 9.1 Sensitivity analysis of degradation from (a)-(b) various currents at 20% initial SOC, 5% DOD, and 4.7x10^{-3} Ω m^2; (c) various initial SOCs at 20 A, 5% DOD, and 4.7x10^{-3} Ω m^2; and (d) various DODs at 20% initial SOC, and 4.7x10^{-3} Ω m^2

The lithium loss in Figure 9.1(a) appears higher for lower currents. However, from the Tafel equation, it is known that a higher negative electrode current density will generate higher parasitic current density. Figure 9.1(b) confirms this earlier assessment that a higher current rate will result in a more aggressive side reaction. The reason lithium loss is higher for lower currents in Figure 9.1(a), is because lithium loss is defined as the integral of the parasitic current density over time and it takes a longer time for the lower currents to reach the same processed capacity compared to the higher

currents. Essentially, lower currents degrade the battery more because they degrade the battery for a longer period of time. Thus, the charging time is another factor to consider when analyzing degradation.

The other results observed from the sensitivity analysis provide a clear dependence on the operational SOC and DOD (Figure 9.1(c)-(d)). As expected, the lithium loss decreases with the initial SOC. The parasitic current density decreases with a positive change in negative electrode potential, or a negative change in operation SOC. The lithium loss increases with DOD because the battery usage increases as well, exposing the battery to more degradation. The sensitivity analysis did not identify any relationship between the parasitic current density and the SEI resistance.

9.2 Battery Degradation and Duty Cycles

The most significant assumption made throughout this work is that the degradation rate of a LiB depends upon its duty cycle. To confirm this assumption, the fitted battery degradation model was simulated on the UDDS, US06, and HWFET duty cycles with initial SOCs of 80%, 50% and 20% (Figure 9.2). Cycleable lithium loss is used to assess real-time degradation rates of the duty cycles.

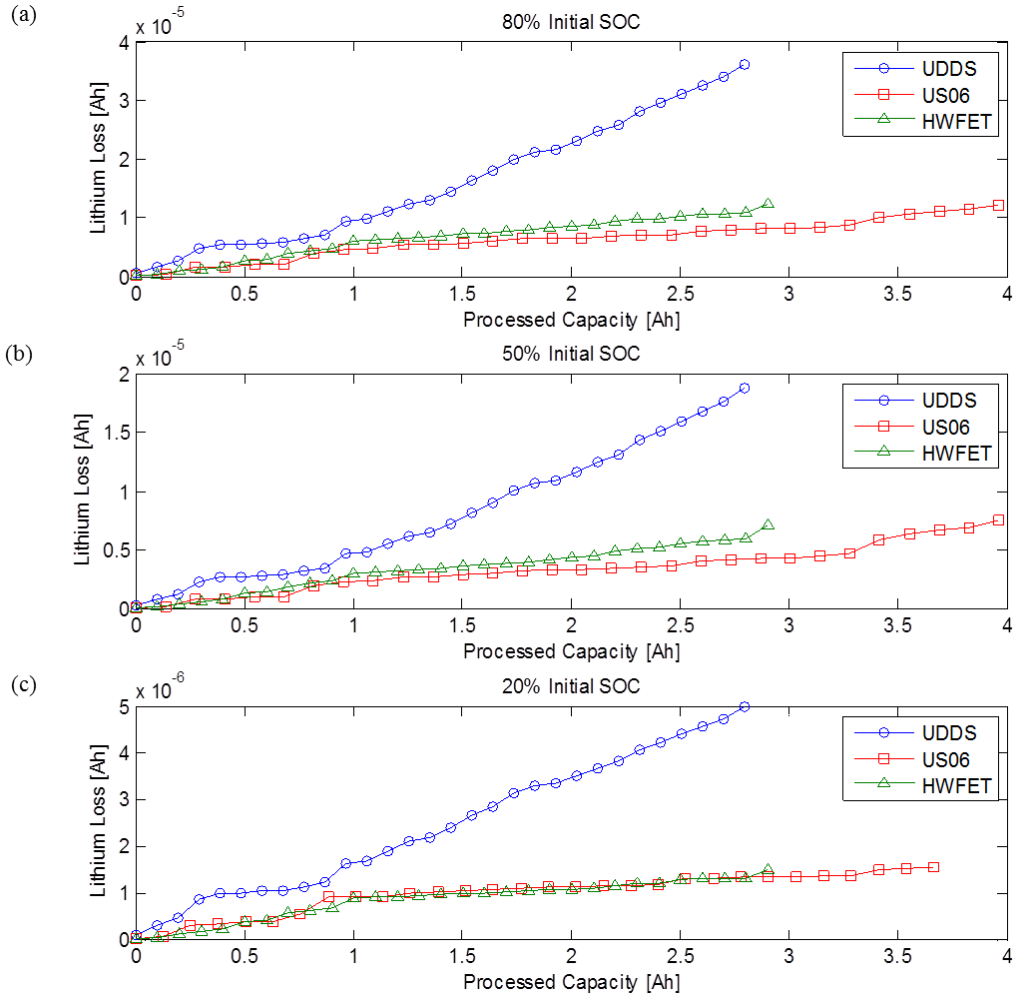

Figure 9.2 Simulated degradation rates of a fresh AMP20 pouch battery for the UDDS, US06, and HWFET duty cycles for (a) 80% initial SOC, (b) 50% initial SOC, (c) 20% initial SOC

The simulation results confirm the assumption that the degradation rate depends on the duty cycle, regardless of the initial SOC. The UDDS duty cycle consumes the most amount of lithium at the highest rate compared to the US06 and HWFET duty cycles. The HWFET duty cycle degrades the battery at a slightly higher rate than the US06 duty cycle.

Considering the typical associations with the three drive cycles, the UDDS drive cycle represents typical city driving, the US06 drive cycle represents aggressive city driving, and the HWFET drive cycle represents highway driving. These associations would typically suggest that the degradation rate would be highest for the US06 drive cycle, followed by the UDDS drive cycle and the HWFET drive

cycle. However, the simulation results disagree with convention since the UDDS drive cycle degrades the battery capacity at a significantly higher rate compared to the other drive cycles. This can be explained by considering the side reaction kinetics involved.

Since the UDDS, US06, and HWFET duty cycles were simulated at the same initial SOC and state of health (SEI resistance), the primary difference between the duty cycles is their current demands, charging times, and DODs. Based on the sensitivity analysis, duty cycles with longer charging times, at higher currents, and larger DODs, should yield higher degradation rates. Reviewing the duty cycle statistics provides insight into why the UDDS duty cycle degraded the battery more than the other two cycles (Table 9.1).

Table 9.1 Comparison of aggressiveness between duty cycles

Parameter	UDDS	US06	HWFET
Maximum Discharge Current [A]	53.47	136.51	42.60
Maximum Charge Current [A]	24.20	39.93	32.11
Mean Discharge Current [A]	6.02	21.21	12.91
Mean Charge Current [A]	1.34	2.56	0.77
Charging Time [s]	361.55	133.92	89.39
DOD [%]	11.45	17.68	13.70

The duty cycle statistics reveal insights into the reasoning behind the UDDS duty cycle's higher degradation rate. The UDDS duty cycle has the highest degradation rate due to the amount of time spent charging the battery compared to the US06 and HWFET duty cycles. This appears to be the most significant factor when assessing duty cycle impact on degradation since the UDDS duty cycle does not have the most severe current statistics and does not have the largest DOD. The US06 duty cycle has the most severe current statistics and the largest DOD but does not degrade the battery significantly more than the HWFET duty cycle. The large DOD of the US06 duty cycle is also representative of the operational SOC of the duty cycle, and a large DOD means a lower operational SOC throughout the cycle. Therefore, the interaction between the severe current statistics and longer charging time with the lower operational SOC of the US06 duty cycle is limiting lithium loss to a

similar rate as the HWFET duty cycle. Regardless, the larger DOD should cause higher degradation rates for the US06 duty cycle, but does not because the effect of the duty cycle DOD is not accounted for in these simulations.

To account for the impact of DOD on the degradation rate, the simulations were conducted again; this time with a 1C charging period following the duty cycle. The notion is that a larger DOD will require more charging to return the battery SOC to its initial value. Thus, a larger DOD will increase the amount of time spent charging the battery and increase the lithium loss associated with that duty cycle. The simulation results represent the round-trip degradation associated with each duty cycle at various initial SOCs (Figure 9.3).

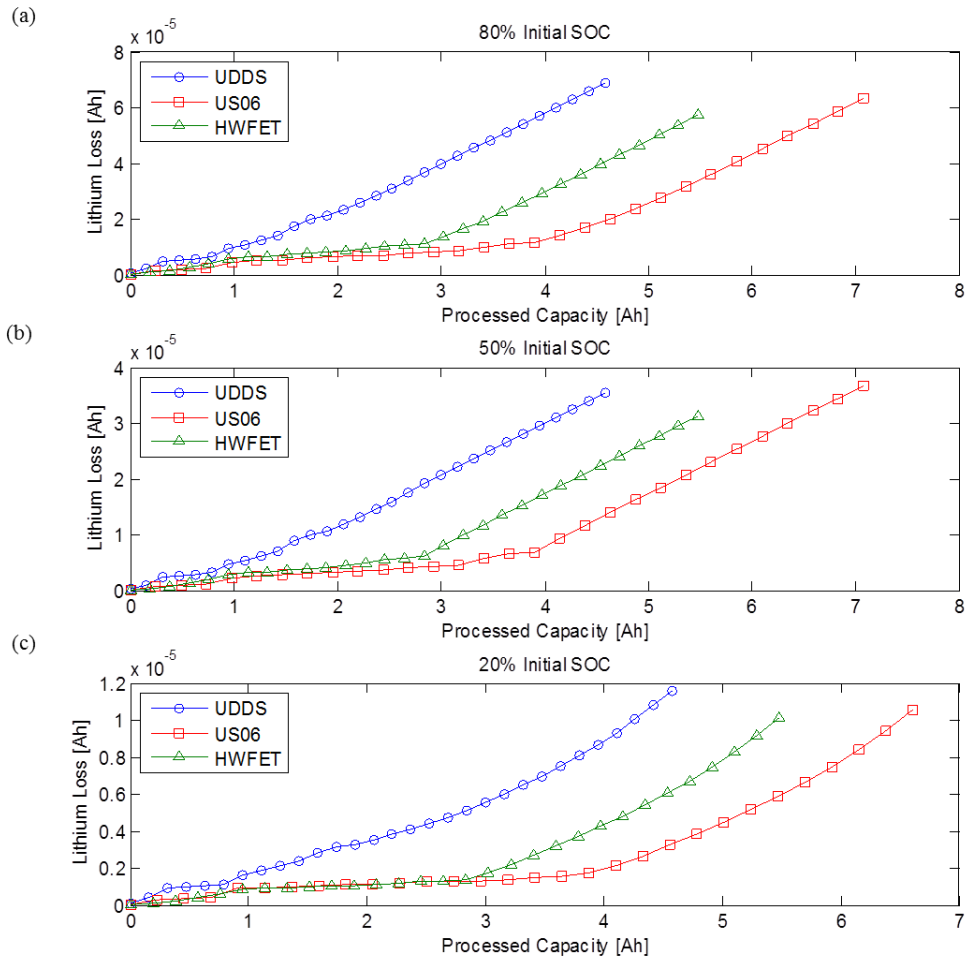

Figure 9.3 Simulated round-trip degradation rates of a fresh AMP20 battery for the UDDS, US06, and HWFET duty cycles for (a) 80%, (b) 50%, and (c) 20% initial SOCs

The newest set of simulation results provides confirmation that the DOD is an important factor when considering the duty cycle effects on battery degradation. Without considering the DODs of the duty cycles, the UDDS cycle consumed at least 2.5 times more lithium ions than the US06 and HWFET cycles. After accounting for the various DODs, the round-trip degradation rates of the three duty cycles were comparable. The US06, HWFET, and UDDS duty cycles received the highest to lowest increase in lithium loss as a direct result of including duty cycle DOD. These results validate the conclusions from the sensitivity analysis that increasing the DOD will increase degradation rates because more charging is required to return the battery SOC to its initial value.

Overall, the degradation analysis on the EPA drive cycles has revealed that the degradation rate of a vehicle-grade battery pack depends strongly upon the duty cycle. Longer charging times at higher currents, higher operational SOCs, and larger DODs, lead to higher degradation rates. One limitation of the simulation results thus far is that the experiments have been limited to the EPA drive cycles. These cycles are often considered to be weak representations of real-world driving behaviour. Therefore, logged vehicle data from FleetCarma's database is used to simulate battery degradation on real-world driving data to validate the results obtained from the EPA drive cycles.

9.3 Real-World Degradation Analysis

Four sets of Nissan Leaf data were selected from the FleetCarma database to verify the conclusions made from the simulations on the EPA drive cycles. The four data sets have distinct driving patterns to ensure the conclusions made from this study are robust (Figure 9.4). The objective of this study is to confirm that the charging time, the operational SOC, the DOD, and the current demands are significant factors that affect battery degradation on real-world usage profiles.

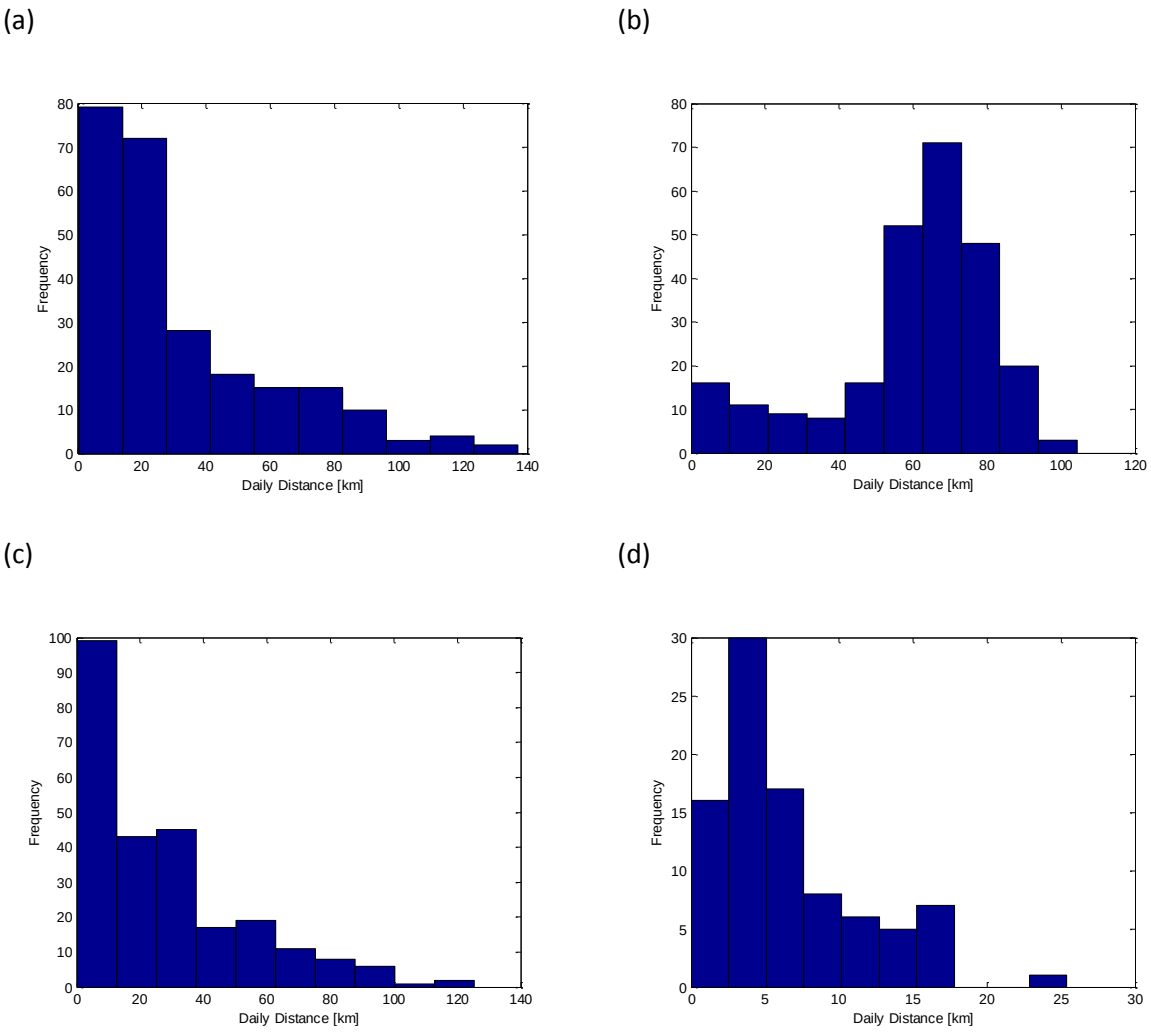

Figure 9.4 Daily distance histograms for the four Nissan Leaf data sets, (a) Driver 1, (b) Driver 2, (c) Driver 3, and (d) Driver 4

The statistics on the four sets of Nissan Leaf data can identify differences before the degradation simulations are conducted (Table 9.2). The previous findings of the sensitivity analysis and EPA duty cycle simulations have shown strong evidence that the degradation rate will directly depend on the duty cycle statistics. More specifically, the charging time, the operational SOC, the DOD, and the current demands will determine which driver degrades the battery more aggressively.

Table 9.2 Summary of duty cycle statistics for the selected driver types

Parameter	Driver 1	Driver 2	Driver 3	Driver 4
Maximum Current [A]	89.12	75.98	77.04	81.76
Minimum Current [A]	85.80	33.94	35.33	34.59
Mean Discharge Current [A]	7.22	4.06	4.57	7.43
Mean Charge Current [A]	2.30	3.84	2.82	4.00
Charging Time [hours]	122.91	59.20	84.33	13.75
Mean Operational SOC [%]	73.28	60.22	69.24	81.26
Mean DOD [%]	4.34	4.03	3.74	6.50

Based on the duty cycle statistics, Driver 1, Driver 3, Driver 2, and Driver 4 are expected to have the highest to lowest degradation rates. Driver 1 is expected to have the highest degradation rate because it contains the longest charging time with aggressive current demands and the second highest mean DOD. Driver 3 is expected to follow Driver 1 because it contains the second longest charging time. While Driver 3 has a lower mean operational SOC, its current demands and DOD are less aggressive than Driver 1's. Driver 4 has more aggressive current demands, and a larger DOD, when compared to Driver 2, but Driver 2 is expected to degrade the battery more than Driver 4. This is primarily because the charging time for Driver 4 is significantly less than Driver 2. Additionally, Driver 4 has a high operational SOC that will reduce its degradation rate.

The four drivers' duty cycles were simulated to predict capacity fade over a span of eight years (Figure 9.5). To reduce simulation time, and because the time between trips is unavailable, the simulations do not include calendar aging. The degradation rates observed are solely a result of the duty cycle and the 1C charging procedure used to transition the SOCs between trips.

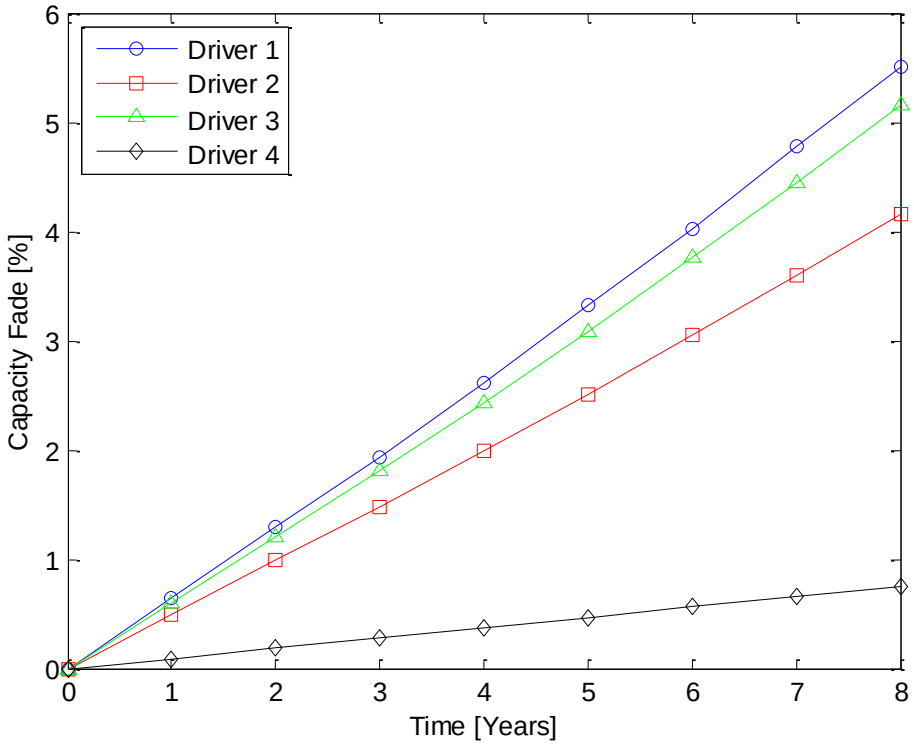

Figure 9.5 Capacity fade over eight years of driving

The simulation results are in agreement with the hypothesized order of degradation based on the information accumulated from the sensitivity analysis and EPA duty cycle study. Driver 1, Driver 3, Driver 2, and Driver 4 experienced 5.51%, 5.17%, 4.16%, and 0.75% capacity fade, respectively. The factor with the largest impact is the charging time experienced by the battery for a given duty cycle. The extremity of the current demands, the DOD, and the operational SOC are secondary factors that would distinguish two duty cycles with similar charging times.

The key result of this study is the confirmation that the degradation rate of real-world data is heavily dependent upon the duty cycle.

9.4 Degradation Reduction Methods

Based on these results, battery degradation could be reduced by limiting the amount of regenerative braking, or maintaining a low battery SOC for the duration of the battery's lifetime. The purpose of regenerative braking is to capture the energy that would otherwise be lost with mechanical braking

and to use that energy to propel the vehicle at a later time. It does not make logical sense to limit such an efficient system to reduce battery degradation; especially since the aforementioned degradation rates are so slow. However, it is more reasonable to maintain a lower battery SOC. BEVs such as the Nissan Leaf cannot be controlled to maintain a low SOC, and thus the driver should only charge the battery to an SOC required to satisfy the next day's required range. PHEVs and HEVs can be controlled to operate the battery at a relatively low SOC to reduce the degradation rate; which is already a common practice in the automotive industry.

9.5 Pack Design Considerations

Considering battery pack design and sizing, the maximum capacity loss simulated over eight years was 5.51%; however, the lowest degradation was 0.75%. The current definition of EOL, mentioned previously, is when the battery capacity degrades to 80% of its rated capacity or the battery power degrades to 80% of the power rating at 80% DOD. Thus, battery packs are sized to last through 20% degradation. The simulation results suggest that such pack design leads to gross oversizing; reducing efficiencies and increasing costs and GHG emissions. It should be noted that the simulated results do not account for calendar aging and temperature effects that would increase the degradation predictions.

Oversizing can be prevented in two ways: using data to specify pack size or generating multiple pack sizes. In the first scenario, the combination of real-world battery data and physics-based models can be used to determine the optimal battery size to satisfy range requirements over the lifetime of the vehicle instead of assuming 20% degradation. The second scenario is to understand that there may be several classes of drivers and that some drivers will degrade the batteries faster than others. Real-world driving data can be used by those drivers to identify which battery pack, from a selection of sizes, is right for them. For example, the Tesla Model S comes in two battery pack sizes. The driver can use their personal degradation prediction to identify which pack will meet their range requirements at the vehicle's EOL.

The system requirements to use the second scenario are already possible through CrossChasm's FleetCarma system. The system consists of vehicle monitoring data as well as vehicle models, which can be used to determine driver behaviour, monitor driving statistics, predict fuel consumption and costs, and more. Unfortunately the system does not include a metric for battery degradation. Thus, the

integration of the battery degradation model into a vehicle model would make the second scenario a reality.

9.6 Model Limitations & Future Work

It was previously noted that the empirically-fit variables of the SP degradation model restrict it's applications from being applied to other batteries. Therefore, the simulation results are applicable to the AMP20 battery that was tested. While these results could potentially be applied to other AMP20 batteries, variations in manufacturing the batteries may alter their performance and degradation properties. Therefore future work should aim to improve the fit of the SP degradation model by removing the empirically-fit LFP particle resistance. Also, several AMP20 batteries should be characterized to understand the distribution of their physical properties such as capacity or particle sizes. Such an analysis would provide useful statistical information on the accuracy of future predictions.

Another limitation of the current work is the assumption that battery temperature and calendar aging do not impact battery degradation. These assumptions were used to minimize the complexity of the model and simulation work. The objective was to determine how duty cycles affect degradation, so the temperature and storage conditions were removed from consideration. However, these two factors are known to have an impact on battery degradation. Therefore, future work should include the research and experimentation of these effects on degradation so a robust degradation model can be generated.

The battery degradation testing and simulation procedures used a 1C charging rate, but the charging rate experienced by a pack like the Nissan Leaf is less than C/4. The simulation results also indicated that the charging procedure was causing degradation on a similar scale as the duty cycle. This impacted the ability to isolate the effect of the duty cycle when performing the 8 year lifetime prediction. Future work should involve testing and simulating the battery in a similar way to this study, but with lower charging rates.

Finally, the SP degradation model is an independent system; external from a vehicle model. The drive cycle a vehicle experiences must either be logged or modeled to generate a duty cycle to pass into the degradation model. That degradation model can then be run to predict the growth of an SEI film on the negative electrode surface. The capacity loss is measured by cycling the battery model at 1C to determine its discharge capacity and compare it to the rated capacity. Although such a

procedure is useful in predicting battery degradation for CrossChasm consulting, it is not useful and cannot be integrated into the FleetCarma product line. Integrating the battery degradation equations into a vehicle model would provide FleetCarma with the capability of assessing per-trip degradation results as well as degradation predictions into the future. Therefore, it is recommended that future work include the integration of the degradation model into a vehicle model.

Chapter 10
Conclusions & Recommendations

10.1 Conclusions

Lithium ion battery degradation depends on the duty cycle being performed. For an automotive battery such as the A123 AMP20 battery selected for this study, the degradation depends on the drive cycle. Degradation simulations on the UDDS, US06, and HWFET U.S. Environmental Protection Agency (EPA) drive cycles yielded respective degradation rates of 17.41, 3.08, and 4.64 (μAh Li^+)(Ah Processed)$^{-1}$ at 80% initial state-of-charge (SOC), 7.04, 1.79, and 2.14 (μAh Li^+)(Ah Processed)$^{-1}$ at 50% initial SOC, and 1.85, 0.46, and 0.54 (μAh Li^+)(Ah Processed)$^{-1}$ at 20% initial SOC.

A sensitivity analysis on the degradation model identified a dependence on the negative electrode potential, the solid electrolyte interface (SEI) impedance, and the negative electrode current density. Thus, battery degradation depends upon the operational battery SOC and the depth-of-discharge (DOD), the history of the battery usage, and the instantaneous usage of the battery. Thus, a higher SOC, a larger DOD, a more aggressive usage history, and aggressive current demands would theoretically lead to higher degradation rates. However, there was no discernible effect from the SEI resistance on the degradation rates.

DOD is important to consider when discussing degradation for automotive applications. The battery will need to be charged at the end of a trip depending on how much it was discharged during the trip. Therefore, trips with larger DODs will lead to additional degradation from the recharging process. The UDDS, US06, and HWFET duty cycles were simulated with charging at 80%, 50%, and 20% initial SOC. It was observed that the recharging process accounted for between 47% and 86% of the total lithium loss.

Four Nissan Leaf data sets were extracted from the FleetCarma database to determine if the simulation results from the sensitivity analysis and the EPA duty cycle study were applicable to real-world driving data. It was predicted that Driver 1, Driver 3, Driver 2, and Driver 4 would yield the highest to lowest capacity fade over an eight year simulation based on the charging time, the current demand, the mean operational SOC, and the mean DOD of the duty cycles. The hypothesis was correct with 5.51%, 5.17%, 4.16%, and 0.75% capacity fade for Driver 1, Driver 3, Driver 2, and

Driver 4. This confirms that battery degradation is a function of the duty cycle. More specifically, the charging time, the current demand, the operational SOC, and the DOD of a duty cycle are all vital factors that impact how the battery ages.

The following milestones were completed to reach the aforementioned conclusions:

- Rate capability characterization tests were conducted on an A123 AMP20 battery.
- An existing hybrid test bench was repurposed to cycle the AMP20 battery on duty cycles for battery degradation experiments.
- An electrochemical battery model was combined with a kinetic-limited degradation model into a single-particle battery degradation model in Simulink.
- 2 mAh galvanostatic cycling data was used to fit the model parameters while the rate capability data was used to fit a positive electrode particle resistance look-up-table.
- Hybrid test bench degradation results were used to fit the degradation parameters in the battery model.

The simulation results and observations presented in this work are limited to the particular A123 AMP20 battery selected for testing and modeling. The model generated for the battery requires an empirically-fit positive electrode resistance look-up-table that is specific to that battery. The results are also limited to room temperature conditions and to the assumption that there is no calendar aging. Regardless of the limitations, the results and observations provided evidence to support further investigation into duty cycle dependent battery degradation.

Ultimately, the main conclusion of this work is that battery degradation is a function of the duty cycle. Therefore, each driver will degrade the battery differently over the lifetime of the vehicle. Duty cycle factors that increase the degradation rate are long charging times, aggressive current demands, high operational SOC, and large DOD.

10.2 Recommendations

1. It is recommended that an investigation be conducted to determine the best lifetime prediction model for $LiFePO_4$ batteries used in vehicle applications. This investigation should include a dimensional analysis to improve the knowledge gained from the sensitivity analysis in this work. A proposed model improvement is to use the variable solid-state diffusivity model

presented in Appendix J for its superior accuracy in galvanostatic conditions. Other models should be considered.

2. To improve the robustness of the model, it is recommended that more experiments be conducted to collect more data. Perform the experiments detailed in this work, but test for a longer period of time; reduce the charging rate to less than C/4 to isolate duty cycle degradation; test the US06, HWFET, and any other duty cycle to fit the degradation model to multiple data sets; and perform the tests a multiple ambient temperatures.
3. Conduct calendar aging experiments at various storage conditions to determine how vehicle storage impacts its lifetime.
4. The benefit to using the model proposed in this work is the ability to integrate it into a vehicle model since it is already built in Simulink. Thus, it is recommended to integrate the degradation model into a vehicle model to predict real-time degradation. Real-time degradation prediction would help in designing control strategies to mitigate harmful operating conditions. It would also work well in the FleetCarma system, providing the capability to monitor and predict battery degradation based on an individual's driving behaviours.

References

[1] B. Schoettle and M. Sivak, "A Comparison of CAFE Standards and Actual CAFE Performance of New Light-Duty Vehicles," University of Michigan Transportation Research Institute, Ann Arbor, Michigan, 2013.

[2] C. Shiau, C. Samaras, R. Hauffe and J. Michalek, "Impact of battery weight and charging patterns on the economic and environmental benefits of plug-in hybrid vehicles," *Energy Policy,* vol. 37, pp. 2653-2663, 2009.

[3] E. Wood, "Battery End-of-Life Considerations for Plug-In Hybrid Electric Vehicles," Colorado State University, Fort Collins, Colorado, 2011.

[4] Idaho National Laboratory, "Battery test manual for plug-in hybrid electric vehicles," Idaho National Laboratory, Idaho Falls, Idaho, 2008.

[5] M. Allen, "Driver Behavior & Your Fleet Budget," December 2013. [Online]. Available: https://www.fleetcarma.com/resources/driver-behavior/. [Accessed 04 July 2014].

[6] P. Simon and Y. Gogotsi, "Materials for electrochemical capacitors," *Nature Materials,* vol. 7, pp. 845-854, 2008.

[7] D. Linden and T. Reddy, Handbook of Batteries, Third Edition ed., New York: McGraw-Hill, 2001.

[8] G. Ehrlich, "Chapter 35: Lithium-Ion Batteries," in *Handbook of Batteries*, 3 ed., New York, McGraw-Hill, 2002, pp. 35.1-35.94.

[9] S. Chikkannanavar, D. Bernardi and L. Liu, "A review of blended cathode materials for use in Li-ion batteries," *Journal of Power Sources,* no. 248, pp. 91-100, 2014.

[10] J. Tarascon and M. Armand, "Issues and challenges facing rechargeable lithium batteries," *Nature,* vol. 414, pp. 359-367, 2001.

[11] M. Safari, M. Morcrette, A. Teyssot and C. Delacourt, "Multimodal physics-based aging model for life prediction of Li-ion batteries," *Journal of The Electrochemical Society,* vol. 156, no. 3, pp. A145-A153, 2009.

[12] K. S. Ng, C. S. Moo, Y. P. Chen and Y. C. Hsieh, "Enhanced coulomb counting method for estimating state-of-charge and state-of-health of lithium-ion batteries," *Applied Energy,* vol. 86, pp. 1506-1511, 2009.

[13] M. Dubarry, N. Vuillaume and B. Liaw, "From single cell model to battery pack simulation for li-ion batteries," *Journal of Power Sources,* vol. 186, pp. 500-507, 2009.

[14] A. Barré, B. Deguilhem, S. Grolleau, M. Gérard, F. Suard and D. Riu, "A review on lithium-ion battery ageing mechanisms and estimations for automotive applications," *Journal of Power Sources,* vol. 241, pp. 680-689, 2013.

[15] J. Vetter, P. Novák, M. Wagner, C. Veit, K.-C. Möller, J. O. Besenhard, M. Winter, M. Wohlfahrt-Mehrens, C. Vogler and A. Hammouche, "Ageing mechanisms in lithium-ion batteries," *Journal of Power Sources,* vol. 147, pp. 269-281, 2005.

[16] Q. Badey, G. Cherouvrier, Y. Reynier, J.-M. Duffault and S. Franger, "Ageing forecast of lithium-ion batteries for electric and hybrid vehicles," *Current Topics in Electrochemistry,* vol. 16, pp. 65-79, 2011.

[17] E. M. Krieger, *Effects of variability and rate on battery charge storage and lifespan,* Princeton: Princeton University, 2013.

[18] M. Kassem, J. Bernard, R. Revel, S. Pelissier, F. Duclaud and C. Delacourt, "Calendar aging of a graphite LiFePO4 cell," *Journal of Power Sources,* vol. 208, pp. 296-305, 2012.

[19] M. Broussely, P. Biensan, F. Bonhomme, P. Blanchard, S. Herreyre, K. Nechev and R. Staniewicz, "Main aging mechanisms in Li ion batteries," *Journal of Power Sources,* vol. 146, pp. 90-96, 2005.

[20] V. Agubra and J. Fergus, "Lithium ion battery anode aging mechanisms," *Materials,* vol. 6, pp. 1310-1325, 2013.

[21] P. Arora and R. White, "Capacity fade mechanisms and side reactions in lithium-ion batteries," *Journal of the Electrochemical Society,* vol. 145, no. 10, pp. 3647-3667, 1998.

[22] Q. Badey, G. Cherouvrier, Y. Reynier, J.-M. Duffault and S. Franger, "Ageing forecast of lithium-ion batteries for electric and hybrid vehicles," *Current Topics in Electrochemistry,* vol. 16, pp. 65-79, 2011.

[23] N. Omar, M. A. Monem, Y. Firouz, J. Salminen, J. Smekens, O. Hegazy, H. Gaulous, G. Mulder, P. Van den Bossche, T. Coosemans and J. Van Mierlo, "Lithium iron phosphate based battery - Assessment of the aging parameters and development of cycle life model," *Applied Energy,* vol. 113, pp. 1575-1585, 2014.

[24] K. Takei, K. Kumai, Y. Kobayashi, H. Miyashiro, N. Terada, T. Iwahori and T. Tanaka, "Cycle life estimation of lithium secondary battery by extrapolation method and accelerated aging test," *Journal of Power Sources,* Vols. 97-98, pp. 697-701, 2001.

[25] S. Santhanagopalan, Q. Guo, P. Ramadass and R. White, "Review of models for predicting the cycling performance of lithium ion batteries," *Journal of Power Sources,* vol. 156, pp. 620-628, 2006.

[26] Q. Zhang and R. White, "Capacity fade analysis of a lithium ion cell," *Journal of Power Sources,* vol. 179, pp. 793-798, 2008.

[27] M. Safari, M. Morcrette, A. Teyssot and C. Delacourt, "Life-prediction methods for lithium-ion batteries derived from a fatigue approach: I. Introduction: Capacity-loss prediction based on damage accumulation," *Journal of The Electrochemical Society,* vol. 157, no. 6, pp. A713-A720, 2010.

[28] G. Prasad and C. Rahn, "Model based identification of aging parameters in lithium ion batteries," *Journal of Power Sources,* vol. 232, pp. 79-85, 2013.

[29] G. Prasad and C. Rahn, "Development of a first principles equivalent circuit model for a lithium ion battery," in *ASME 2012 5th Annual Dynamic Systems and Control Conference joint with the JSME 2012 11th Motion and Vibration Conference*, For Lauderdale, Florida, 2012.

[30] G. Ning, R. White and B. Popov, "A generalized cycle life model of rechargeable Li-ion batteries," *Electrochimica Acta,* vol. 51, pp. 2012-2022, 2006.

[31] E. Prada, D. Domenico, Y. Creff, J. Bernard, V. Sauvant-Moynot and F. Huet, "A simplified electrochemical and thermal aging model of LiFePO4-Graphite Li-ion batteries: Power and capacity fade simulations," *Journal of The Electrochemical Society,* vol. 160, no. 4, pp. A616-A628, 2013.

[32] M. Farkhondeh and C. Delacourt, "Mathematical modeling of commercial LiFePO4 electrodes based on variable solid-state diffusivity," *Journal of The Electrochemical Society,* vol. 159, no. 2, pp. A177-A192, 2012.

[33] P. Ramadass, B. Haran, R. White and B. Popov, "Mathematical modeling of the capacity fade of Li-ion cells," *Journal of Power Sources,* vol. 123, pp. 230-240, 2003.

[34] C. Tóth-Nagy, *Linear engine development for series hybrid electric vehicles,* Morgantown: West Virginia University, 2004.

[35] M. Ehsani, Y. Gao and A. Emadi, "Modern electric, hybrid electric, and fuel cell vehicles: fundamentals, theory, and design," 2nd ed., Boca Raton, CRC Press, 2010, pp. 26-131.

[36] M. Ahman, "Primary energy efficiency of alternative powertrains in vehicles," *Energy,* vol. 26, pp. 973-989, 2001.

[37] General Motors, Chevrolet, "New: United States," 2011. [Online]. Available: http://media.gm.com/content/media/us/en/chevrolet/vehicles/Equinox/2011.tab1.html. [Accessed 6 June 2013].

[38] General Motors, "GM Powertrain: 2013 Powertrain Product Portfolio," 2013. [Online]. Available: http://gmpowertrain.com/VehicleEngines/PowertrainProducts.aspx. [Accessed 6 June 2013].

[39] Office of Transportation & Air Quality, "Detailed Test Information," U.S. Environmental Protection Agency, 10 July 2014. [Online]. Available: http://www.fueleconomy.gov/feg/fe_test_schedules.shtml. [Accessed 10 July 2014].

[40] U.S. Government Printing Office, "40 CFR 600.114-08: Vehicle-specific 5-cycle fuel economy and carbon-related exhaust emission calculations," 2008. [Online]. Available: http://www.law.cornell.edu/cfr/text/40/600.114-08. [Accessed 10 July 2014].

[41] Environmental Protection Agency & Department of Transportation, *Federal Register: Part II,* 129 ed., vol. 76, 2011.

[42] Energy Efficiency & Renewable Energy, U.S. Department of Energy, "Alternative Fuels Data Center - Fuel P{roperties Comparison," 27 2 2013. [Online]. Available: http://www.afdc.energy.gov/fuels/fuel_comparison_chart.pdf. [Accessed 24 06 2014].

[43] M. Farkhondeh, M. Safari, M. Pritzker, M. Fowler, T. Han, J. Wang and C. Delacourt, "Full-range simulation of a commercial LiFePO4 electrode accounting for bulk and surface effects: A comparative analysis," *Journal of The Electrochemical Society,* vol. 161, no. 3, pp. A201-A212, 2014.

[44] J. Lo, "Effect of temperature on lithium-iron phosphate battery performance and plug-in hybrid electric vehicle range," University of Waterloo, Waterloo, Ontario, 2013.

[45] M. Safari and C. Delacourt, "Modeling of a Commercial Graphite/LiFePO4 Cell," *Journal of Electrochemical Society,* vol. 158, no. 5, pp. A562-A571, 2011.

[46] M. Safari and C. Delacourt, "Mathematical modeling of lithium iron phosphate electrode: Galvanostatic charge/discharge and path dependence," *Journal of The Electrochemical Society,* vol. 158, no. 2, pp. A63-A73, 2011.

[47] V. Subramanian, V. Diwakar and D. Tapriyal, "Efficient macro-micro scale coupled modeling of batteries," *Journal of The Electrochemical Society,* vol. 152, no. 10, pp. A2002-A2008, 2005.

[48] A123 Systems, "Products: AMP20 Lithium Ion Prismatic Cell," 2012. [Online]. Available: http://www.a123systems.com/prismatic-cell-amp20.htm. [Accessed 15 July 2014].

[49] Maccor, "Products: Model 4200," January 2012. [Online]. Available: http://www.maccor.com/Products/Model4200.aspx. [Accessed 15 July 2014].

[50] TDK-Lambda Corporation, "Products: Programmable: ZUP-Series," [Online]. Available: http://www.tdk-lambda.com/products/sps/ps_adj/zup/indexe.html. [Accessed 19 July 2014].

[51] TDI Power, "XBL Series 800," [Online]. Available: http://www.tdipower.com/PDF/dynaload/xbl_800.pdf. [Accessed 19 July 2014].

[52] K. Kwon, C. Shin, T. Kang and C. Kim, "A two-dimensional modeling of a lithium-polymer battery," *Journal of Power Sources,* vol. 163, pp. 151-157, 2006.

[53] J. Newman and W. Tiedemann, "Potential and current distribution in electrochemical cells," *Journal of the Electrochemical Society,* vol. 140, no. 7, pp. 1961-1968, 1993.

[54] W. Tiedemann and J. Newman, "Current and potential distribution in lead-acid battery plates," in *Proceedings of the Symposium on Battery Design and Optimization*, Princeton, 1979.

[55] H. Gu, "Mathematical analysis of a Zn / NiOOH cell," *Journal of the Electrochemical Society,* vol. 130, no. 7, pp. 1459-1464, 1983.

[56] U. Kim, C. Shin and C. Kim, "Modeling for the scale-up of a lithium-ion polymer battery," *Journal of Power Sources,* vol. 189, pp. 841-846, 2009.

[57] J. Newman and K. Thomas-Alyea, Electrochemical Systems, Hoboken, New Jersey: John Wiley & Sons, Inc., 2004.

[58] T. Bradley and C. Quinn, "Analysis of plug-in hybrid electric vehicle utility factors," *Journal of Power Sources,* vol. 195, pp. 5399-5408, 2010.

Appendix A

Comprehensive Review of Battery Degradation Mechanisms

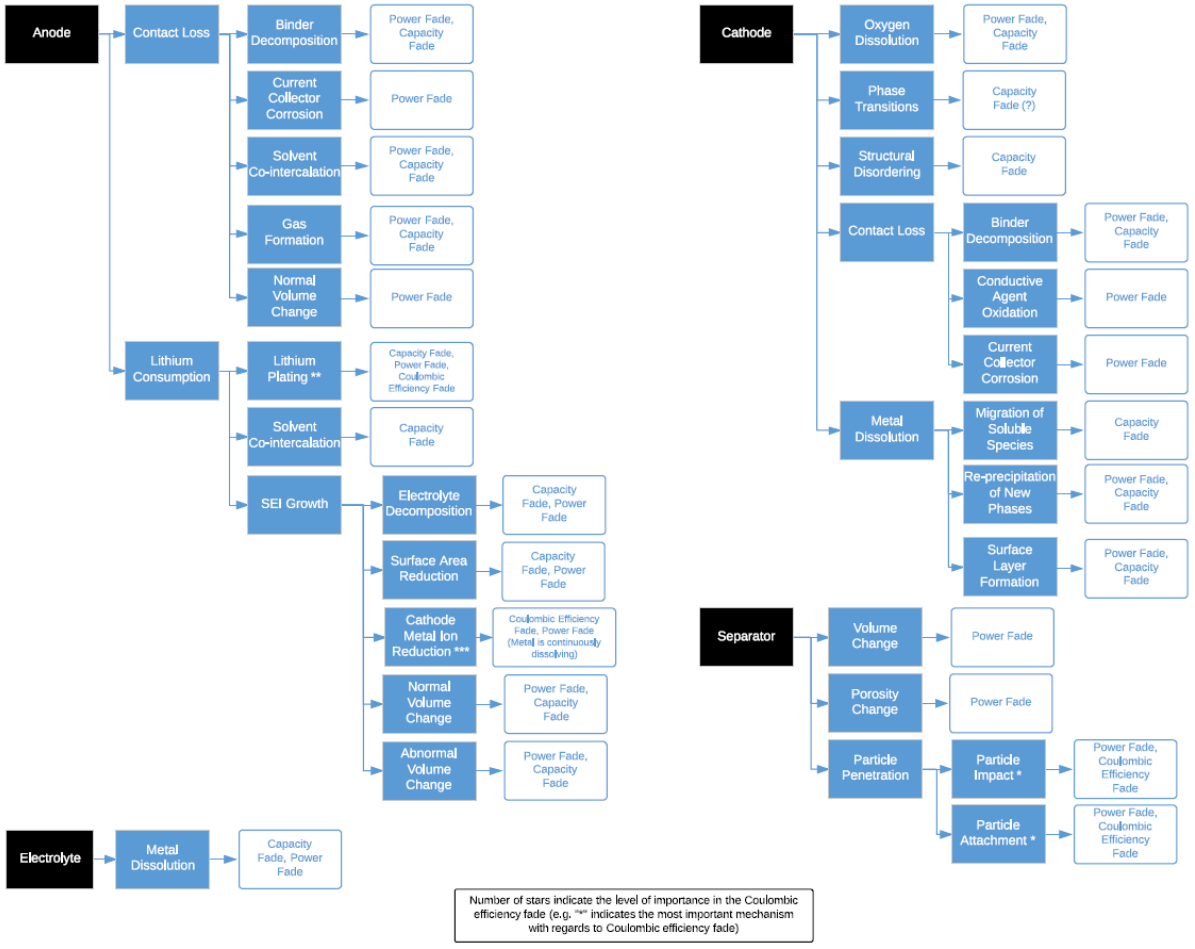

Appendix B

2011 Chevrolet Equinox Specifications

The 2011 Chevrolet Equinox specifications are presented below, taken directly from the General Motors product information webpage [37].

Overview		
Models:	2011 Chevrolet Equinox LS, LT and LTZ; FWD and AWD	
Body style / driveline:	five-passenger, four-door SUV, front-engine, front- or all-wheel drive	
Construction:	welded galvanized steel (except for hood and roof) monocoque	
EPA vehicle class:	compact sport utility vehicle	
Manufacturing location:	Ingersoll, Ontario, Canada (and Oshawa, Ontario, Canada interim 2011 MY)	
Key competitors:	Ford Escape, Kia Sorento, Honda CR-V, Hyundai Santa Fe and Toyota RAV4	
Engine		
Type:	2.4L DOHC I-4 DI	3.0L DOHC V-6 DI
Application:	std on LS, LT, LTZ	opt on LT, LTZ
Displacement (cu in / cc):	145 / 2384	183 / 2997
Bore & stroke (in / mm):	3.46 x 3.85 / 88 x 98	3.50 x 3.15 / 89 x 80.3
Block material:	cast aluminum	sand-cast aluminum with cast-in bore liners
Cylinder head material:	cast aluminum	cast aluminum
Valvetrain:	DOHC, four valves per cylinder; variable valve	DOHC, four valves per cylinder; variable valve

	timing	timing
Fuel delivery:	direct sequential fuel injection with electronic throttle control	direct sequential fuel injection with electronic throttle control
Compression ratio:	11.2:1	11.7:1
Horsepower (hp / kW @ rpm):	182 / 136 @ 6700*	264 / 197 @ 6950*
Torque (lb-ft / Nm @ rpm):	172 / 233 @ 4900*	222 / 301 @ 5100*
Recommended fuel:	regular unleaded	regular unleaded or E85 ethanol
Emissions controls:	close-coupled catalytic converters; Quick-Sync 24x ignition system; returnless fuel rail; fast-response O_2 sensor	close-coupled catalytic converters; Quick-Sync 24x ignition system; returnless fuel rail; fast-response O_2 sensor
EPA-estimated fuel economy (city / hwy):	22 / 32 (FWD) 20 / 29 (AWD)	17 / 24 (FWD) 16 / 23 (AWD)
Transmission		
Type:	Hydra-Matic 6T45 six-speed automatic electronically controlled with electronic range select	Hydra-Matic 6T70 six-speed automatic electronically controlled with electronic range select
Application:	std	opt w/ V-6
Gear ratios: (:1):		

First:	4.58	4.48
Second:	2.96	2.87
Third:	1.91	1.84
Fourth:	1.44	1.41
Fifth:	1.00	1.00
Sixth:	0.74	0.74
Reverse:	2.94	2.88
Final drive ratio:	3.23 (FWD) 3.53 (AWD)	2.77

Transmission / Suspension	
Front:	independent strut-type with tuned coil springs; direct-acting stabilizer bar; hydraulic ride bushings
Rear:	independent four-link with coil springs and trailing arm; stabilizer bar; hydraulic link bushings
Steering type:	rack-mounted electric power steering with 2.4L; hydraulic power rack-and-pinion with 3.0L
Steering ratio:	18.1:1 (2.4L) 17.4:1 (3.0L)
Steering wheel turns, lock-to-lock:	3.46 (2.4L) 2.90 (3.0L with 18-in wheels) 2.80 (3.0L with 19-in wheels)
Turning circle, curb-to-curb (ft / m):	40.0 / 12.2 (with 17- and 18-in wheels) 42.6 / 13 (with 19-in wheels

Brakes	
Type:	power front and rear vented discs, standard anti-lock brakes
Rotor diameter x thickness (in / mm):	front: 12.6 x 1.18 / 321 x 30 rear: 11.9 x 0.78 / 303 x 20
Total swept area (cu in / mm):	front: 20.7 / 526 rear: 15.3 / 390

Wheels / Tires	
Wheel size and type:	17-in painted aluminum (std. on all models) 18-in machine-face aluminum (avail. on LT and LTZ) 19-in chrome-clad aluminum (avail. on LTZ)
Tires:	P225/65R17 all-season steel-belted radial blackwall tires P235/55R18 all-season steel-belted radial blackwall tires P235/55R19 all-season steel-belted radial blackwall tires

Exterior Dimensions	
Wheelbase (in / mm):	112.5 / 2857
Overall length (in / mm):	187.8 / 4771
Overall width (in / mm):	72.5 / 1842
Overall height (in / mm):	66.3 / 1684
Track (in / mm):	front: 62.5 / 1587 rear: 61.8 / 1570
Approach angle (deg):	14.8
Departure angle (deg):	23.2

Breakover ramp angle (deg):	16.5
Minimum ground clearance (in / mm):	7.8 / 198.5
Ground to rear load floor (in / mm):	28.8 / 731.2
Curb weight, base (lb / kg):	3770 / 1710
Weight distribution (front / rear):	58 / 42
Interior Dimensions	
Seating capacity:	5
Headroom (in / mm):	front: 40.9 / 1040 rear: 39.2 / 995
Legroom (in / mm):	front: 41.2 / 1046 rear: 39.9 / 1015
Shoulder room (in / mm):	front: 55.8 / 1418 rear: 55.3 / 1405
Hip room (in / mm):	front: 51.1 / 1294 rear: 51.3 / 1304
Capacities	
EPA interior volume (cu ft / L):	130.5 / 3695
Passenger volume (cu ft / L):	99.7 / 2822
Cargo volume (cu ft / L): Maximum behind rear seat: Maximum behind front seat:	 31.4 / 889 63.7 / 1803
GVWR, standard (lb / kg):	FWD 2.4L: 3761 / 1710

	AWD 2.4L: 3929 / 1786
	FWD 3.0L: 3944 / 1793
	AWD 3.0L: 4101 / 1864
Payload, base (lb / kg):	1190 / 540
Trailer towing maximum (lb / kg):	1500 / 680 (2.4L) 3500 / 1588 (3.0L)
Fuel tank (gal / L):	18.8 / 71.1 (2.4L) 20.9 / 79.1 (3.0L)
Engine oil (qt / L):	5 / 4.7 (2.4L) 6 / 5.7 (3.0L)
Cooling system (qt / L):	8.9 / 8.5 (2.4L) 10 / 9.5 (3.0L)

Appendix C

Ecotec 2.4L Engine Torque Curve

The Ecotec 2.4L engine torque curve is presented below, taken directly from the General Motors powertrain product portfolio webpage [38].

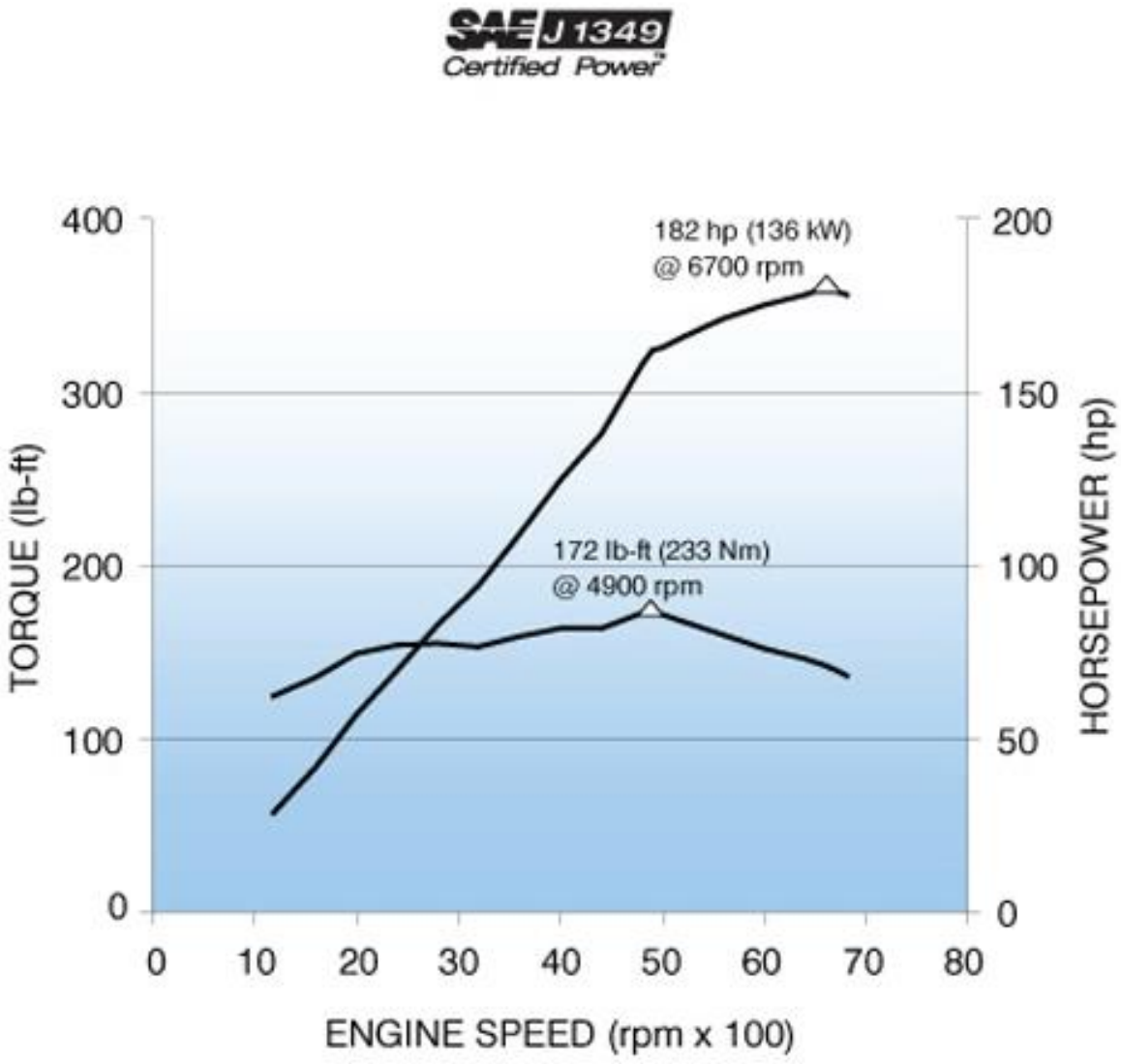

Appendix D

A123 AMP20 Specifications

The A123 AMP20 specifications are presented below, taken directly from the A123 Systems product webpage [48].

Nanophosphate® Lithium Ion Prismatic Pouch Cell

AMP20*m1*HD-A

KEY FEATURES AND BENEFITS

- High usable energy over a wide state of charge (SOC) range and very low cost per Watt-hour
- Excellent abuse tolerance and superior cycle life from A123's patented Nanophosphate® lithium ion chemistry
- High power with over 2,400 W/kg and 4,500 W/L

AMP20 Cell Specifications	
Cell Dimensions (mm)	7.25 x 160 x 227
Cell Weight (g)	496
Cell Capacity (minimum, Ah)	19.5
Energy Content (nominal, Wh)	65
Discharge Power (nominal, W)	1200
Voltage (nominal, V)	3.3
Specific Power (nominal, W/kg)	2400
Specific Energy (nominal, Wh/kg)	131
Energy Density (nominal, Wh/L)	247
Operating Temperature	-30°C to 55°C
Storage Temperature	-40°C to 60°C

Abuse Test	Test Result
Nail Penetration	Pass – EUCAR 3
Overcharge	Pass – EUCAR 3
Over-discharge	Pass – EUCAR 3
Thermal Stability	Pass – EUCAR 4
External Short	Pass – EUCAR 3
Crush	Pass – EUCAR 3

APPLICATIONS

PHEV and EV Passenger Vehicles

PHEV and EV Commercial Vehicles

Utility-scale Storage

A123 SYSTEMS

www.a123systems.com

Nanophosphate® Lithium Ion Prismatic Pouch Cell

AMP20*M1HD-A*

POWER

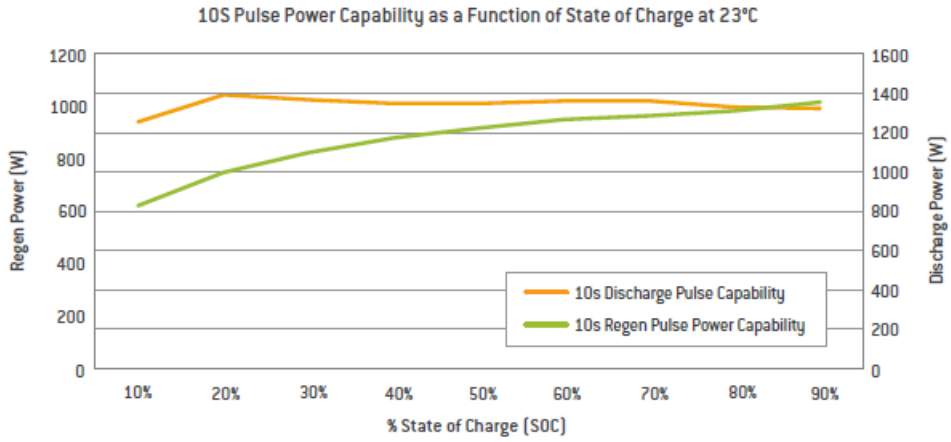

CYCLE LIFE

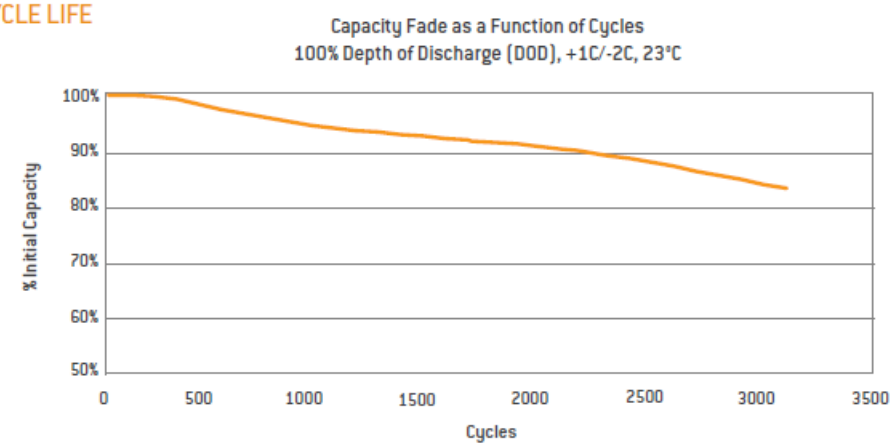

Preliminary specifications, performance may vary depending on use conditions and application.
A123 Systems makes no warranty explicit or implied with this datasheet. Contents subject to change without notice.

CORPORATE HEADQUARTERS
A123 Systems, Inc.
200 West Street
Waltham, MA 02451
(617) 778-5700

www.a123systems.com

A123 SYSTEMS

MD100105-03

Appendix E

Maccor Series 4200 Specifications

The Maccor Series 4200 specifications are presented below, taken directly from the Maccor product webpage [49].

MACCOR

BATTERY & CELL TEST EQUIPMENT WORLD WIDE

MODEL 4200 DESKTOP AUTOMATED TEST SYSTEM

The Model 4200 has all the power of Maccor's Series 4000 floor standing cabinet conveniently packaged in a desktop cabinet.

The Model 4200 is supplied as a complete turnkey system with Tester PC and software. Powered by Maccor's standard test system software and utilizing the same technology found in Maccor's high-precision Series 4000 Automated Test System, the Model 4200 is the perfect desktop test system in Maccor's line of high quality, dependable test systems.

The Model 4200 is supplied with a PowerPole® interface for easily connecting cables or cell holders. Each desktop cabinet is available with up to 16 test positions, however, test systems can have multiple test cabinets.

The Model 4200 can be configured with multi-current range channels, which have a current control range of 300nA to 5A. These multi-current range channels can be configured for voltage ranges of -2V to +8V or 0V to +5V as standard. The accuracy for current and voltage on these channels is ± 0.02% FSR. Alternately, the system can be configured with single current range channels, which can be configured for higher voltages and currents. The single current range channels have a current accuracy of ± 0.05% FSR and a voltage accuracy of ± 0.02% FSR.

Standard Features and Functions

- Adaptable To A Wide Range Of Products (i.e. batteries, super-capacitors, fuel cells, etc.) and Battery Chemistries
- Easily Scalable To Support Capacity Expansion At Acceptable Costs
- Easy To Use And Maintain Minimizing Labor Force
- Customizable To Meet Varying And Evolving Customer Requirements
- Easily Adaptable To Meet A Wide Range Of Testing Needs
- Each Test Station Operates Independently Of The Other Positions
- Can Be User Programmed To Operate In Steps Of Constant Current, Constant Power, Constant Voltage, Constant Resistance, or Voltage Scan (Cyclic Voltammetry).
- With the MIMS Client software, data is easily viewed graphically with different standard graphs. Several Chart types may be displayed at the same time with the ability to store the display settings as a template. Data from different devices may be overlaid on a single chart or viewed side-by-side.

Specifications

Configuration	1 – 16 channels
Current	
Current Range	Per Your Specifications, currents up to 15 Amps available†
Maximum System Charge Current	Per Your Specification, up to 240 Amps
Minimum Full Scale Current	Per Your Specifications, 150 µAmps available
† Higher channel currents (up to a maximum of 240 Amps) can be supplied on systems with fewer channels.	
Voltage	
Minimum Measurement	-2 Volts‡
Measurement Range	Per Your Specifications, voltages up to 150 volts available
Typical Voltage Range	-2V to +8 Volts
‡ Lower minimum measurements can be attained. These would need to be discussed and agreed upon.	
Power	
Maximum System Charge Power	2400 Watts
Maximum System Discharge Power	2400 Watts
Time	
Minimum Step Time	10 mS*
Control, Measurement, and Adjustment	every 10 mS
* 4.6 mS Telecom Pulsing Option Available	

MACCOR
Maccor, Inc
4322 S 49th W Avenue Tulsa, Oklahoma 74107 USA
Contact: Mark Hulse Position: V.P Sales & Marketing
Telephone: +1 918-630-2256 Facsimile: +1 918-445-1496
Email: m.hulse@maccor.com Web: www.maccor.com

Rev 1.2 (January 2012)

Appendix F
Hybrid Test Bench Review

The HTB (Figure F.1) was originally designed and built to test various hybrid technologies and assess their usefulness in vehicle design. However, the HTB has been modified to test batteries on different duty cycles and to measure battery performance and degradation.

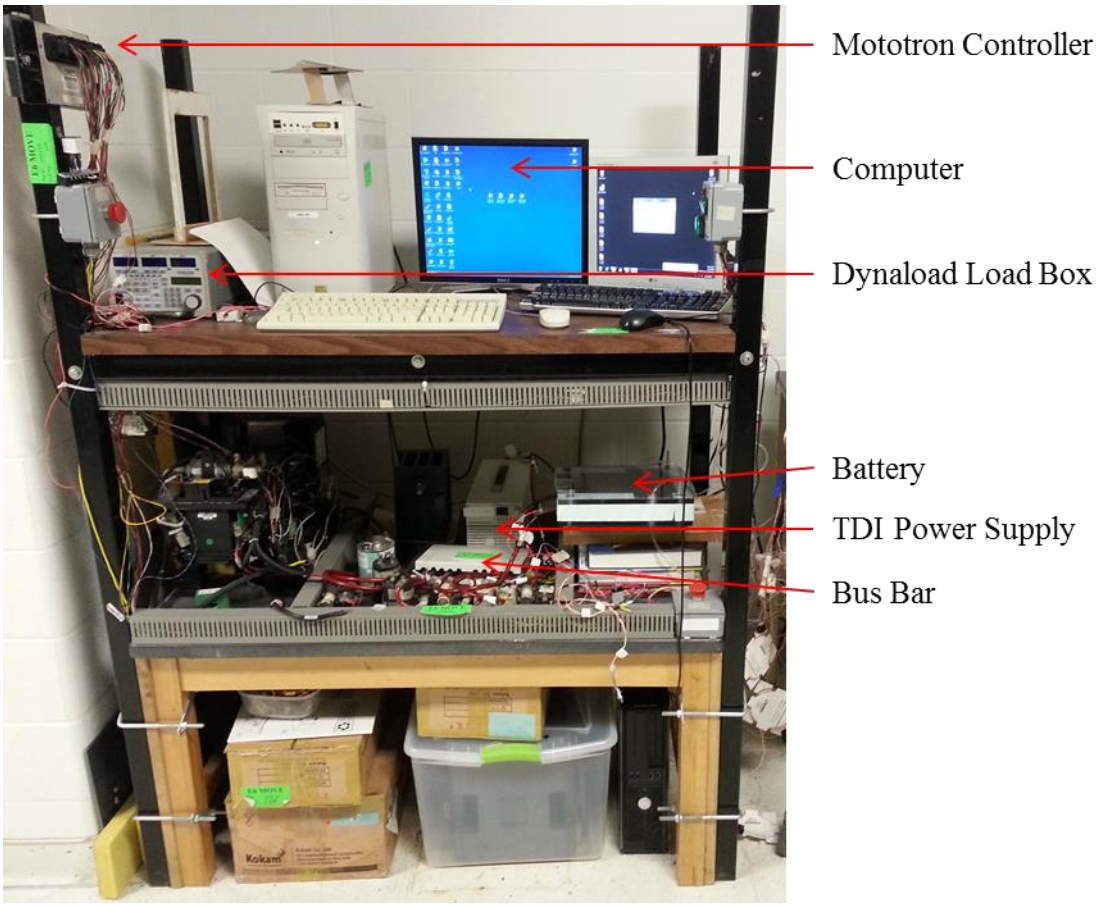

Figure F.1 Labeled image of the HTB

The HTB schematic (Figure F.2) provides an overview of the hardware and connections installed on the bench. The computer provides the basic controls using LabVIEW VI to the controller and load box via RS-232 cables, and the power supply with an Ethernet cable. The computer also offers a GUI for the user to monitor the progress of the experiment. The controller uses analog I/O signal wiring to communicate with the relays and measure the battery voltage. The controller transmits the measured

battery voltage back to the computer. The computer sets the current or voltage values on the load box and power supply depending on the experiment. The current measured internally of the load box and power supply is transmitted back to the computer. Depending on the computer requests, the power supply or load box will provide power to or draw power from the battery, respectively. The component specification sheets are provided in Appendix G.

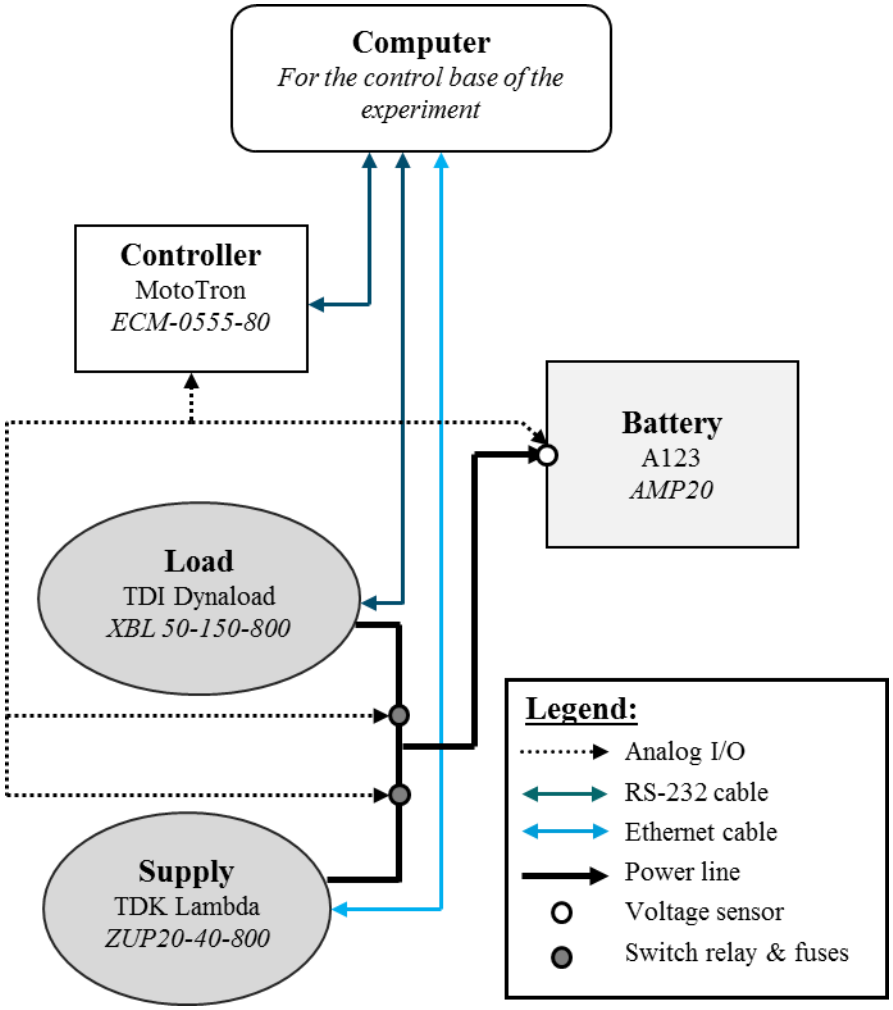

Figure F.2 Labeled schematic of the HTB

LabVIEW VI is software that uses dataflow programming to communicate with and control hardware in a system. For this investigation, LabVIEW was programmed specifically for conducting battery aging experiments. The GUI front panel (Figure F.3) connects the user with controls over the hardware and live monitoring capabilities of the battery performance. From the front panel, the user

can define operational limits of the load box and power supply, and the initial step of the experiment (*e.g.*, rest, charge, discharge). Additionally, the user can confirm the Mototron controller, Dynaload load box, and Lambda power supply are functioning properly before beginning the experiment. Furthermore, the user can monitor the battery current and voltage throughout the experiment; as well as other additional information.

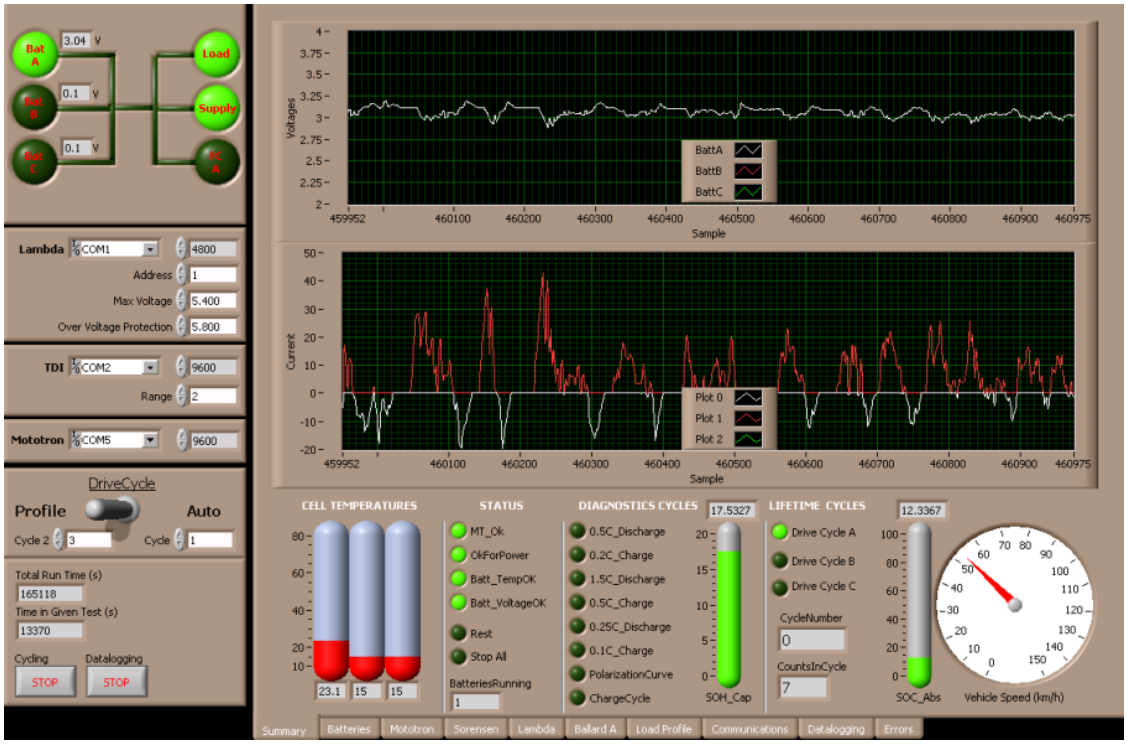

Figure F.3 LabVIEW front panel GUI used to control hardware and monitor the experiment

Additionally, the load profile panel of the LabVIEW GUI offers user control and monitoring of the aging procedure (Figure F.4). The user can define the number of degradation cycles to perform, and any SOC limit above which the battery would not perform a charging event. Also, the load profile panel displays the discharge capacity for each degradation cycle.

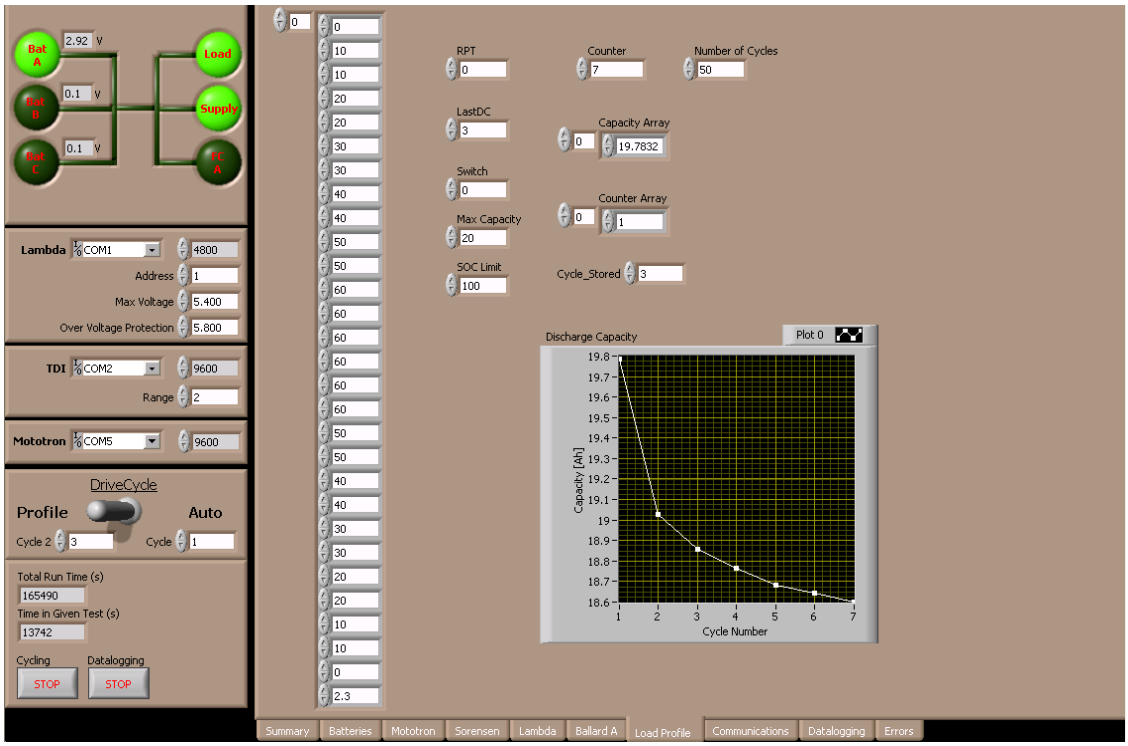

Figure F.4 Load profile panel of GUI to define and monitor the aging procedure

The LabVIEW programming is split into 8 frames consisting of several time sequence structures; which execute in order only when the previous structure has completed.

The first frame initializes the system (Figure F.5). The status of the batteries and hardware are set to ‘false’ so they can be appropriately changed to ‘true’ in the case their operational conditions are satisfied. Additionally, the log file name and directory is requested from the user to determine where the experimental data will be stored.

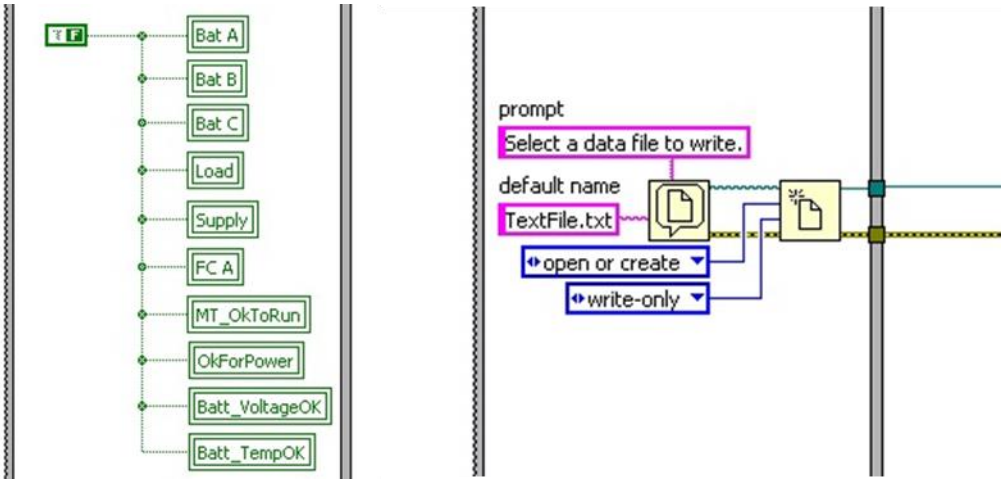

Figure F.5 LabVIEW system initialization procedures

After system initialization, the LabVIEW program progresses to the second frame to initialize the Mototron controller. The Mototron communication ports are configured according to the Mototron specifications (Figure F.6a). The baud rate is defined by the user in the front panel while the flow control, parity, data bits, stop bits, and terminal character are defined directly in the LabVIEW programming. The Mototron settings are requested by LabVIEW to determine the number of batteries connected to the system and to identify any potential errors in the hardware (Figure F.6b). If there are no errors in the hardware, the light indicating a working controller will activate on the front panel.

(a)

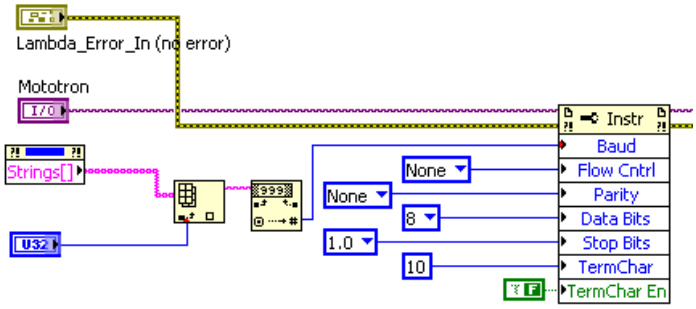

(b)

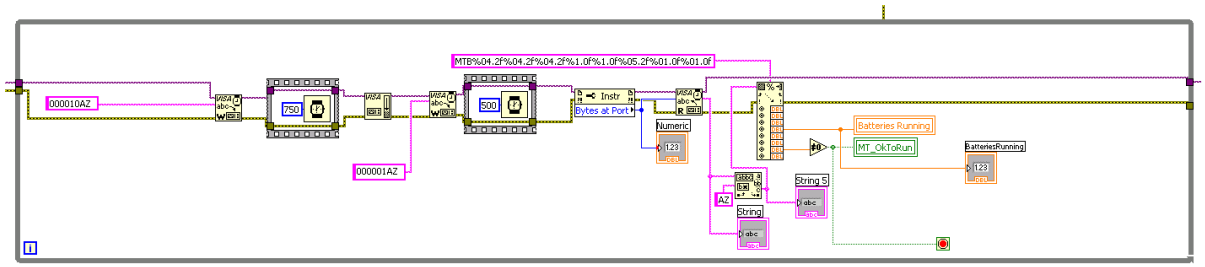

Figure F.6 Mototron controller initialization procedure

The third frame initializes the Lambda power supply is initialized through port configuration, and given an address through which LabVIEW can communicate with the power supply (Figure F.7a). In addition, the operating limits of the Lambda are defined by the user in the front panel and transmitted to the device. Finally, the Lambda settings are requested to confirm that the transmission was successful and to determine if any errors existed (Figure F.7b). If no errors exist, the light indicating a working power supply on the front panel turns on.

(a)

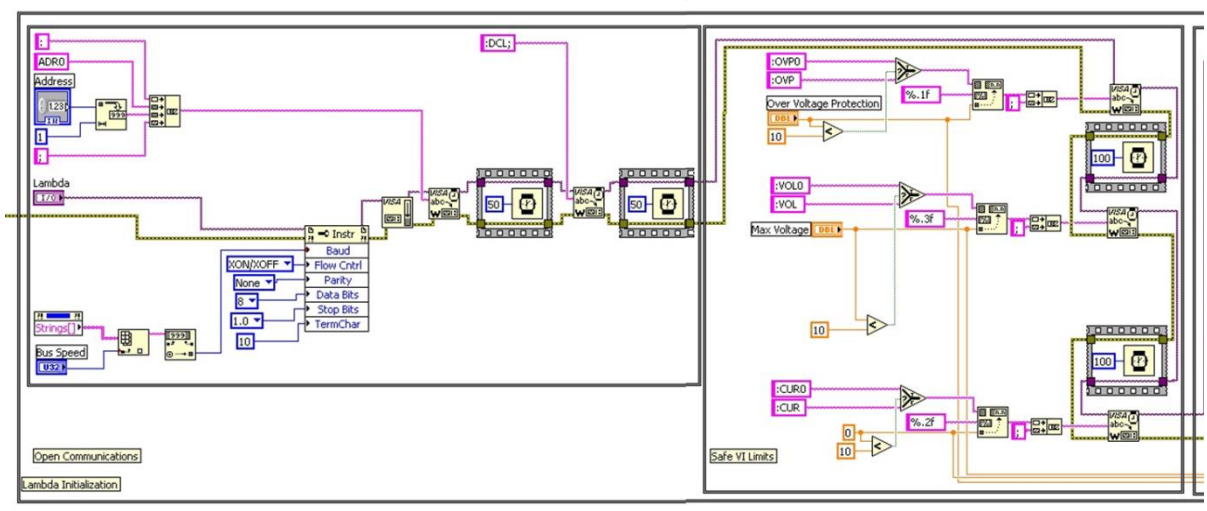

(b)

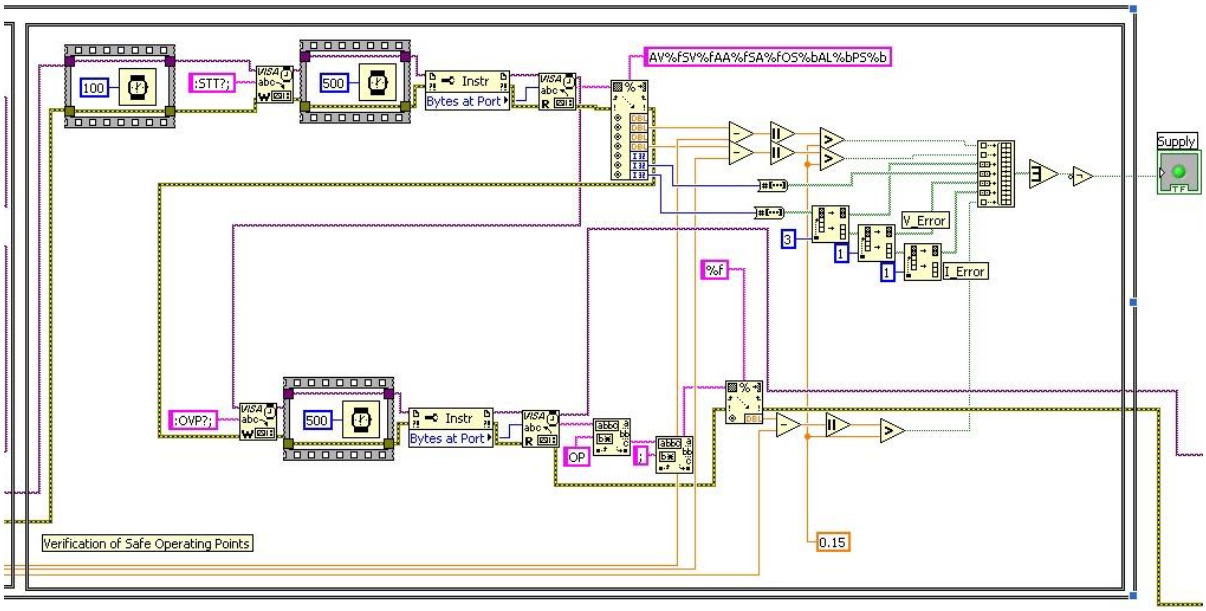

Figure F.7 Lambda power supply initialization procedure

The fourth frame initializes the Dynaload load box. As before, the Dynaload ports are configured and the operating limitations are transmitted to the device (Figure F.8a). Additionally, the physical device input is locked to prevent any setting changes during operation. The operating limits are then confirmed and the light indicating a working load box is turned on (Figure F.8b).

(a)

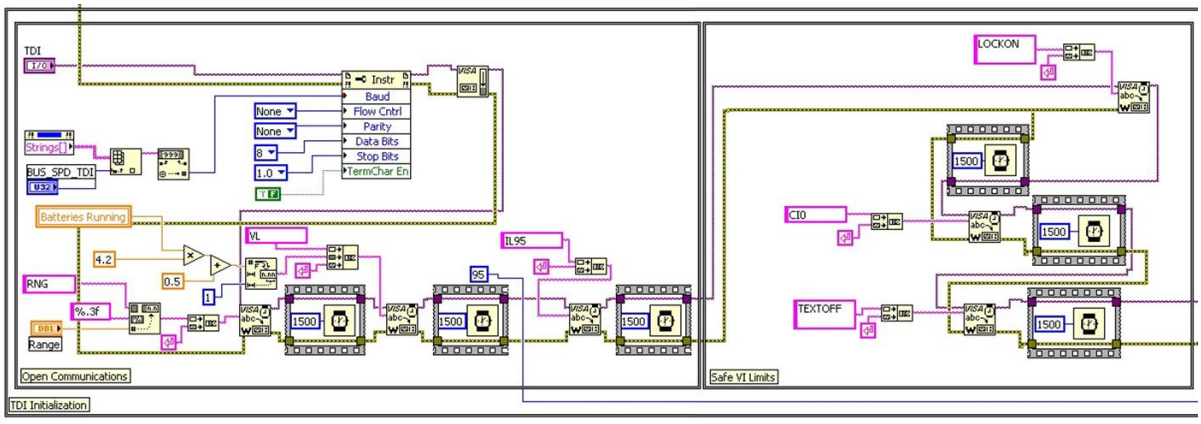

(b)

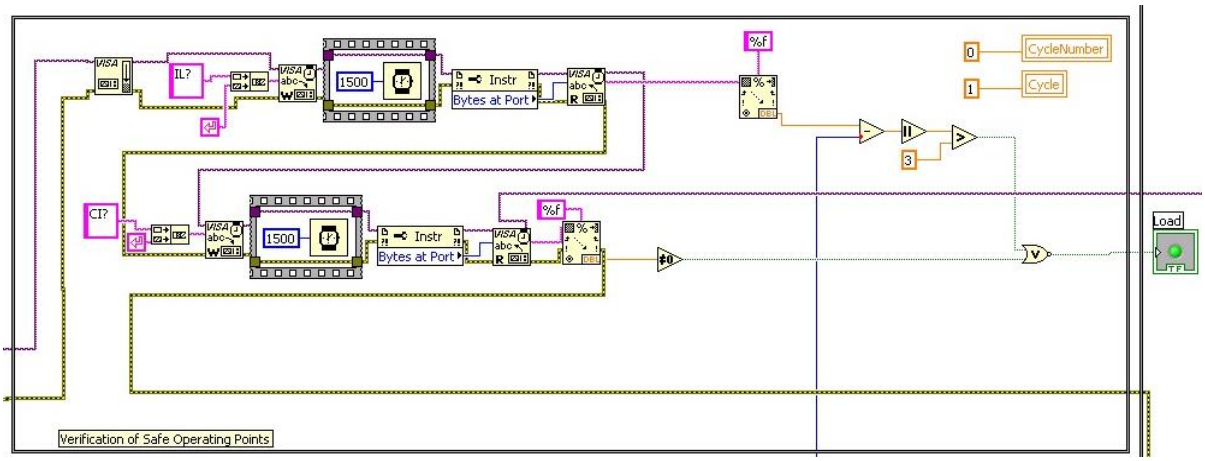

Figure F.8 Dynaload load box initialization procedure

Finally, in the fifth frame, the final check to ensure the system is power-capable occurs (Figure F.9). The Mototron status is requested by LabVIEW and the light confirming system power turns on if there are no errors in the Mototron's response.

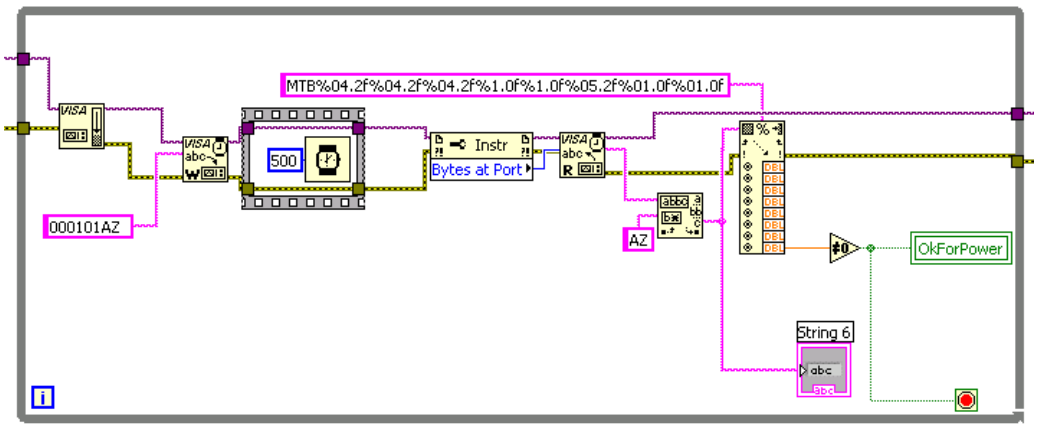

Figure F.9 Final system power confirmation from the Mototron controller

The sixth frame simply readies the power supply and load box for the upcoming experiment, and reads the experimental start time (Figure F.10). The internal relays of the devices close, connecting them to the system.

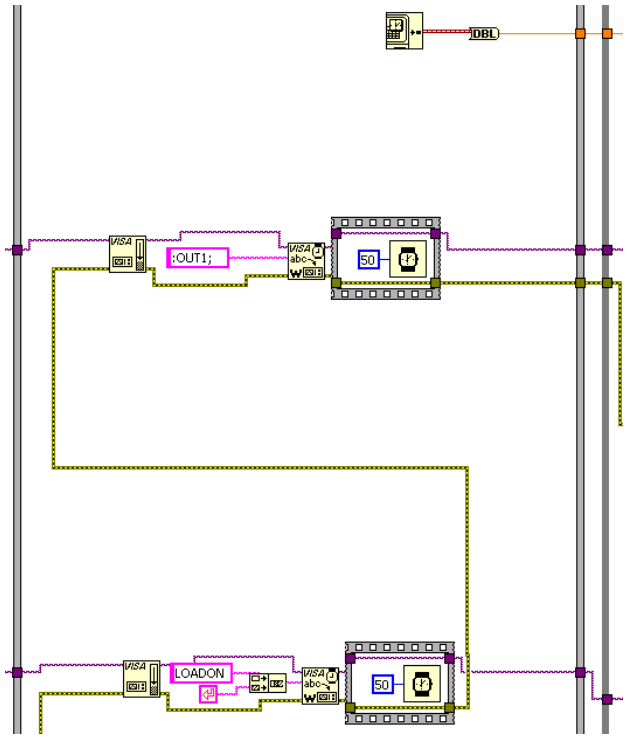

Figure F.10 Recording start time and closing internal relays of Dynaload and Lambda

The seventh, and largest frame, contains the programming required to successfully cycle and age the battery. This frame consists of six sections of programming (Figure F.11).

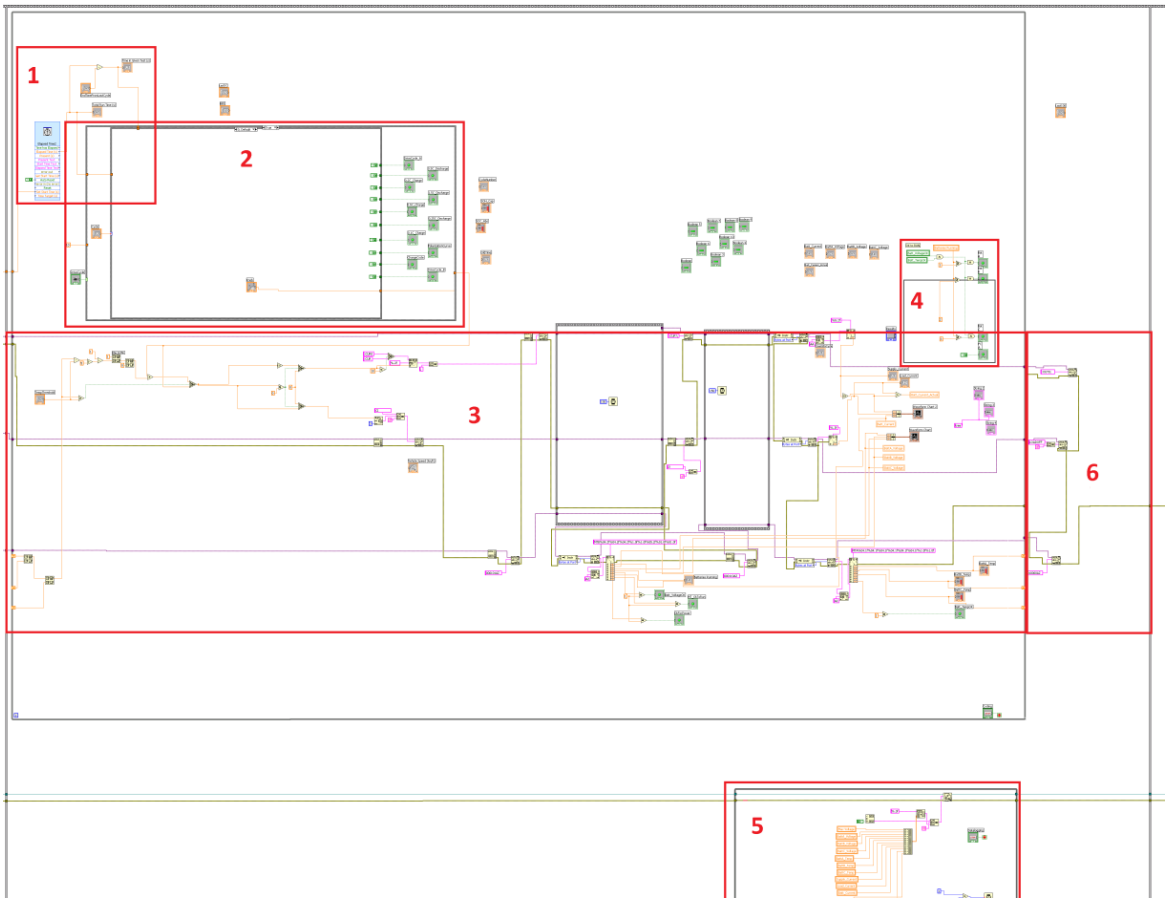

Figure F.11 Operational frame split into six sections of programming

The first section is an operational timer (Figure F.12). The start time from frame six is used as a reference time to measure the elapsed time during operation. The total run time is presented on the front panel GUI, along with the elapsed time for a given test. For example, the total run time for a full charge/discharge cycle would be double the elapsed time for a charge event. These times are used in the following section.

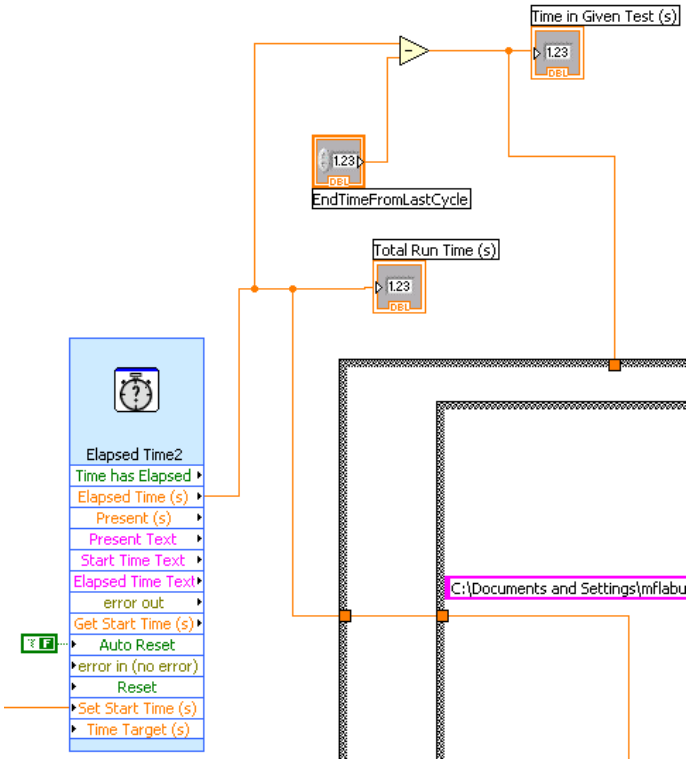

Figure F.12 Elapsed time module keeping track of total and test run times

The second section contains the test procedures that will be imposed onto the battery (Figure F.13). A case structure is used to identify whether the 'Profile' or 'Auto' operations are selected on the front panel (*i.e.,* 'false', 'true', respectively). The original HTB was designed to operate in 'Auto', however this work uses 'Profile'; thus only that case will be discussed. Within the 'Profile' case there is another case structure containing six cases; each of which are a battery test procedure. Only Cycle 1, Cycle 3, and Cycle 6 are used in this experiment; however more are available. Figure F.13 shows the default case, Cycle 1, which performs a CC charge at 20 A until a battery voltage limit of 3.6 V is reached. The front panel light indicating a charging period is also turned on. While there are other structures within this case, they have little importance.

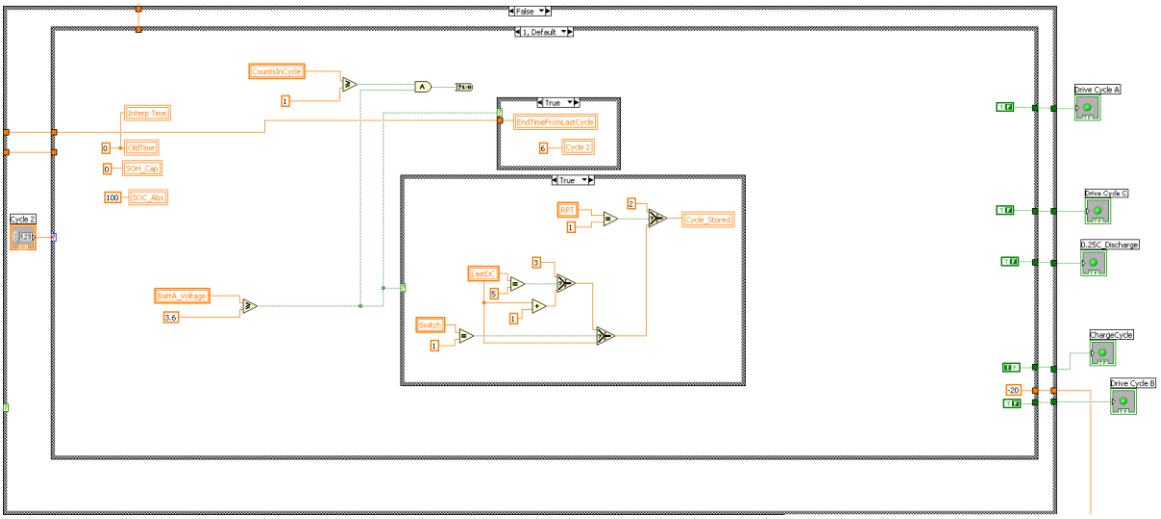

Figure F.13 The charging profile is selected within the 'Profile' operation mode

Cycle 3 contains the programming necessary to test the battery on a variable current duty profile (Figure F.14). In this experiment, Cycle 3 contains the UDDS duty cycle derived from the A123 battery pack in the EcoCar 2 vehicle model. The 'Drive Cycle A' light on the front panel is turned on during Cycle 3's operation. The UDDS duty cycle is imported into LabVIEW from a text file, and interpolated at 0.1 s intervals according to the elapsed time passed from the previous section of programming. The duty cycles repeats itself until the battery voltage reaches a lower limit of 2 V. To prevent the duty cycle from requesting currents outside the operational limits of the devices, the current is saturated at -40 A and 150 A. The SOC is calculated during operation and displayed on the front panel. If the SOC is above the SOC limit set on the load profile GUI panel, the charging current is set to zero. However this feature is not used in this work. When the battery voltage reaches its lower limit, the total discharged capacity is plotted on the load profile GUI panel.

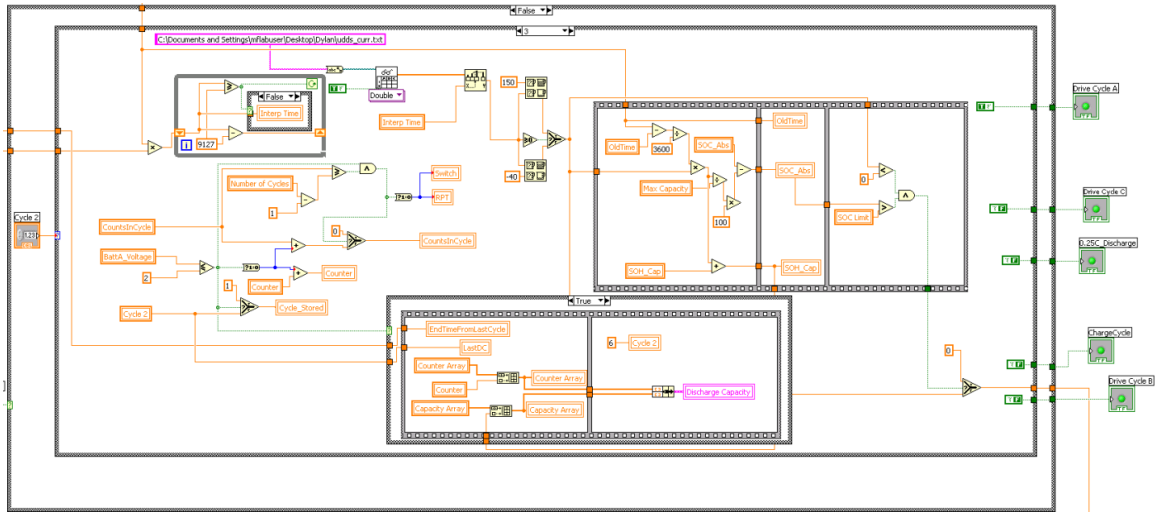

Figure F.14 UDDS duty cycle selected within the 'Profile' operation mode

Cycle 6 consists of a 30 minute resting period, where the 'Rest' light on the front panel is turned on. There is no complicated programming involved in this case.

The next section imposes the duty cycle defined in the previous section onto the battery (Figure F.15). If the requested current from the previous section is negative, the power supply is instructed supply that current to the battery. If the requested current is positive, the load box is instructed to consume that current from the battery. The internal load box and power supply currents are measured and transmitted to LabVIEW. Additionally, the battery voltage signal is transmitted to LabVIEW from the Mototron controller. These signals are plotted on the front panel GUI, and are subsequently passed to the next section.

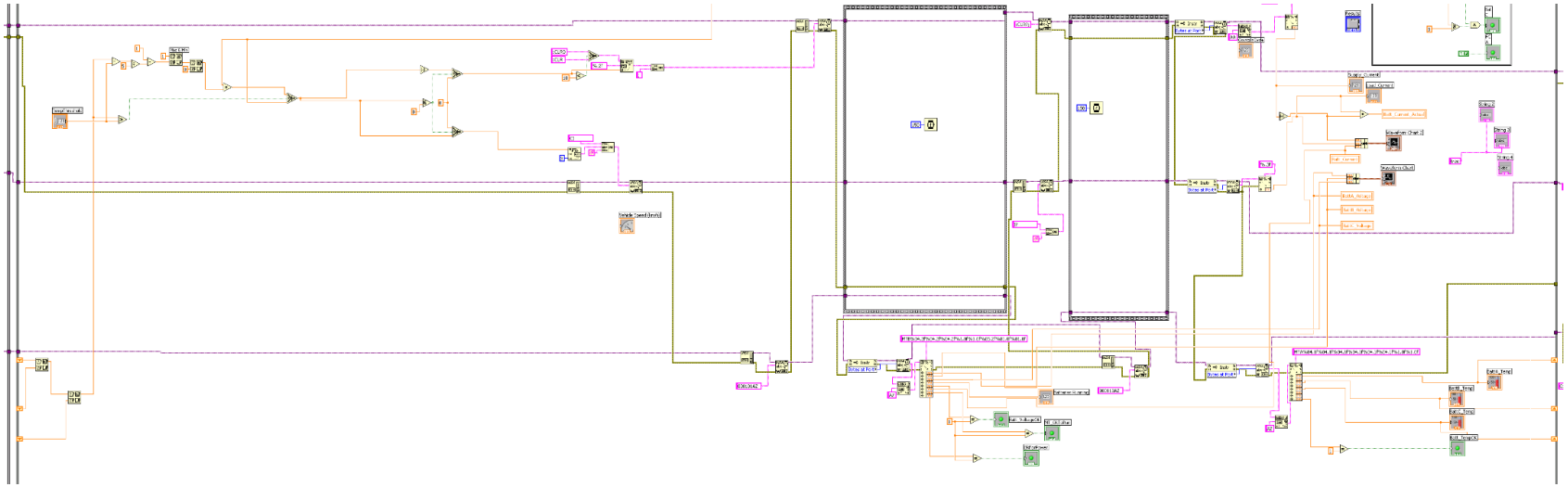

Figure F.15 Programming required to operate the devices on the selected duty cycle and to measure current and voltage signals

Another section within the sixth frame is the battery status check (Figure F.16) where the front panel GUI light indicating proper battery function turns on if the battery temperature and voltage conditions are within their operational limits.

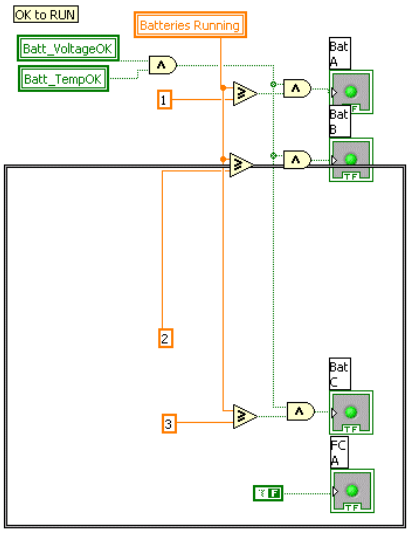

Figure F.16 Battery status check

The second most important section of this frame contains the programming necessary for data logging (Figure F.17). The date, time, battery voltage, temperature, power supply current, load box current, step number, and cycle number signals are logged every 150 ms.

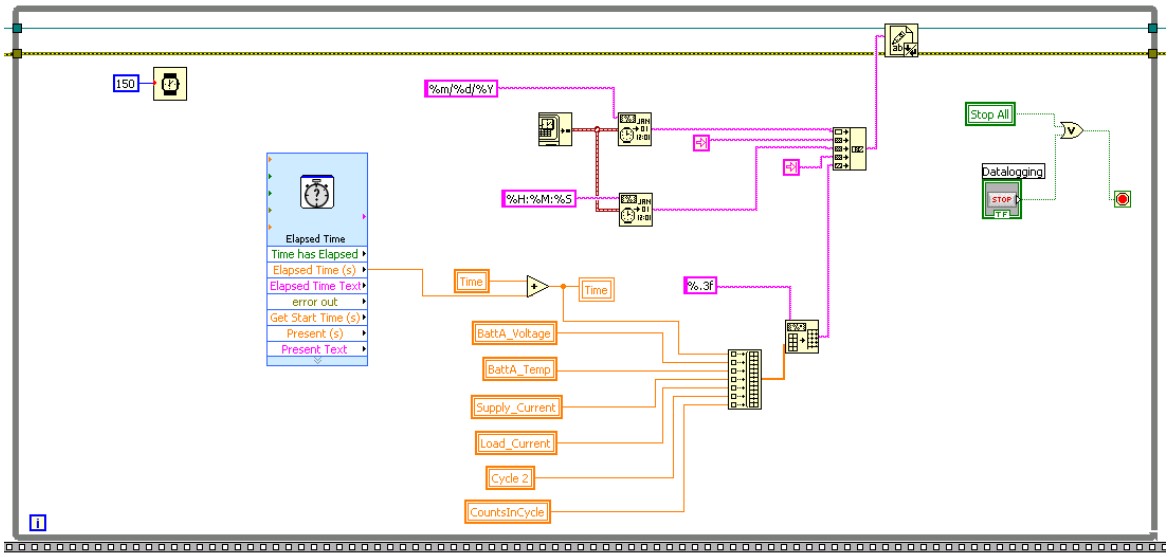

Figure F.17 Data logging programming

The final section of this frame opens the internal relays of the Lambda power supply, Dynaload load box, and Mototron controller to disconnect the devices from the system before ending the scripts (Figure F.18).

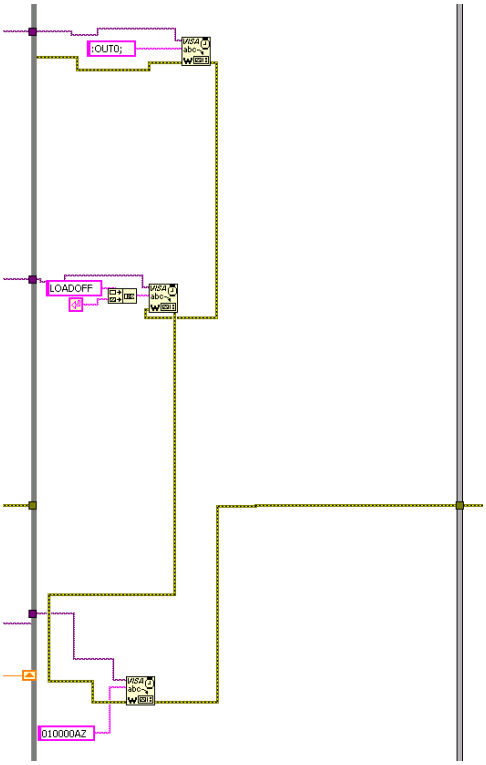

Figure F.18 Opening internal relays of the Dynaload, Lambda, and Mototron controller

The eighth and final frame is similar to the first part of the first frame, when it turns off the operational lights on the front panel GUI (Figure F.5).

Appendix G

HTB Device Specifications

The Lambda Power Supply ZUP 20-40-800 specifications are taken directly from the TDK Lambda Corporation products webpage [50].

TDK·Lambda

ZUP SERIES Programmable CVCC 200W ~ 800W 19Model

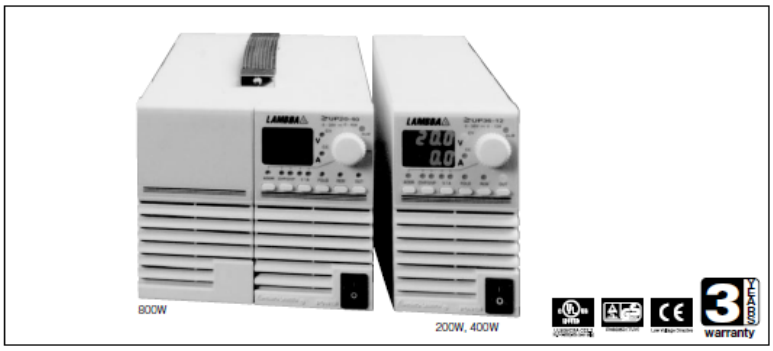

■ Features

- Constant Voltage/Constant Current
- Built-in RS232 & RS485 Interface
- An embedded Microprocessor controller
- Digital Encoder Knob
- Software Calibration
- Last Setting Memory
- Parallel Operation (Master/Slave) Active Current Sharing
- External Voltage or Resistance Programming
- Voltage up to 120V, Current up to 132A
- Active Power Factor Correction: 99%
- 85~265Vac Universal Input Voltage
- 19" Rack Mounted ATE and OEM
- Worldwide Safety Agency Approvals
- CE Mark for LVD and EMC Regulation

■ Model naming method

ZUP 36 - 12 / □ □ □

- Series name
- Output Voltage (0 ~ 36V)
- Output Current (0 ~ 12A)
- Front Panel: L. Output Jacks; BLANK: Standard
- AC Cable: E. Europe; U. USA; O. Unterminated; I. SI 32 std.; BLANK: None
- Serial Link Cable: W. Cable included; BLANK: None

■ Applications

■ Conformity to RoHS Directive

This means that, in conformity with EU Directive 2002/95/EC, lead, cadmium, mercury, hexavalent chromium, and specific bromine-based flame retardants, PBB and PBDE, have not been used, except for exempted applications.

■ Product Line up

	200W		400W		800W	
Output Voltage	Output Current	Model	Output Current	Model	Output Current	Model
0-6V	0-33A	ZUP6-33	0-66A	ZUP6-66	0-132A	ZUP6-132
0-10V	0-20A	ZUP10-20	0-40A	ZUP10-40	0-80A	ZUP10-80
0-20V	0-10A	ZUP20-10	0-20A	ZUP20-20	0-40A	ZUP20-40
0-36V	0-6A	ZUP36-6	0-12A	ZUP36-12	0-24A	ZUP36-24
0-60V	0-3.5A	ZUP60-3.5	0-7A	ZUP60-7	0-14A	ZUP60-14
0-80V	0-2.5A	ZUP80-2.5	0-5A	ZUP80-5	—	—
0-120V	0-1.8A	ZUP120-1.8	0-3.6A	ZUP120-3.6	—	—

ZUP

ZUP Specifications

ITEMS/UNITS			MODEL	UNIT	ZUP6-33	ZUP6-66	ZUP6-132	ZUP10-20	ZUP10-40	ZUP10-80	ZUP20-10
OUTPUT VOLTAGE			(*1)	V	0-6			0-10			
OUTPUT CURRENT			(*2)	A	0-33	0-66	0-132	0-20	0-40	0-80	0-10
RATED OUTPUT POWER				W	198	396	792	200	400	800	200
CONSTANT VOLTAGE	LOAD REGULATION				0.005%+2mV From No load to Full load, constant input voltage.						
	LINE REGULATION				0.005%+1mV From 85-132VAC or 170-265VAC, constant load.						
	RMS RIPPLE (5Hz-1MHz Bandwidth)			mV	5	5	8	5	5	8	5
	RIPPLE (pk to pk) (20MHz Bandwidth)			mV	50	50	100	50	50	90	50
	RECOVERY TIME		(*3)	mS	1			0.5			
	TEMPERATURE COEFFICIENT				30ppm/···C from rated voltage following 30-minute warm-up.						
	TEMPERATURE DRIFT				0.01%+2mV Change in output over 8-hour interval under constant line, load and ambient temp following30-minute warm-up.						
	UP PROGRAMMING RESPONSE TIME (*4)			mS	50	50	60	50	50	60	50
	DOWN PROGRAMMING	FULL LOAD		mS	50	50	50	50	50	50	50
	RESPONSE TIME	NO LOAD		mS	250			350			
CONSTANT CURRENT	LOAD REGULATION		(*5)		0.01%+5mA	0.01%+5mA	0.07%+10mA	0.01%+5mA	0.01%+5mA	0.07%+10mA	0.01%+5mA
	LINE REGULATION		(*6)		0.01%+2mA	0.01%+2mA	0.01%+5mA	0.01%+2mA	0.01%+2mA	0.01%+5mA	0.01%+2mA
	RMS RIPPLE (5Hz-1MHz Bandwidth)			mA	50	100	200	25	50	100	15
	TEMPERATURE COEFICIENT				100ppm/ ···C from rated current following 30-minute warm-up.						
	TEMPERATURE DRIFT		(*8)		0.02%+5mA	0.02%+5mA	0.05%+10mA	0.02%+5mA	0.02%+5mA	0.05%+10mA	0.02%+5mA
PROGRAMMING (*9)	VOLTAGE	RESOLUTION			Better than 0.028% of rated output voltage						
		ACCURACY			0.02%+5mV			0.02%+8mV			
	CURRENT	RESOLUTION			Better than 0.03% of rated output current						
		ACCURACY			0.4%+40mA						
OVERVOLTAGE PROTECTION			(*10)	V	0-7.5			0-13			
HOLD-UP TIME					20mS At 100V/200VAC, rated output voltage and output current.						
DISPLAY	VOLTAGE				3 digits (6v; 20v; 36v; 60v; 80v); 3.5 digits (10v; 120v) accuracy: 0.2% +/- 2 digits.						
	CURRENT				3.5 digits (132A); All others 3 digits, accuracy: 0.5% +/- 3 digits.						
	STATUS				CV/CC, Alarm, Fold, Local/Remote, On/Off.						
OUTPUT PROTECTIONS					Over Voltage, Over Temperature, Foldback.						
INPUT	INPUT VOLTAGE		(*11)		85-265Vac Continuous, 47-63Hz						
	INPUT CURRENT		(*12)	A	3.0/1.5	5.6/2.7	11.2/5.4	2.9/1.4	5.6/2.7	11.2/5.4	2.9/1.4
	INRUSH CURRENT (100/200V)			A	15/30 (*7)	15	30	15/30 (*7)	15	30	15/30 (*7)
	EFFICIENCY (*12)			%	69/72	74/77	74/77	73/77	79/82	77/81	74/78
	INPUT CURRENT HARMONICS				Complies with EN61000-3-2, Class A						
	POWER FACTOR (TYP)				0.99 at 100/200Vac, 100% load.						
ENVIRONMENT	OPERATING TEMPERATURE				0 to 50 ···C ; 100% Load.						
	OPERATING HUMIDITY				30-90% RH (No dewdrop).						
	STORAGE TEMPERATURE				-20 to 70 ···C						
	STORAGE HUMIDITY				10 - 95% RH (No dewdrop).						
MECHANICAL	VIBRATION				10-55Hz, Amplitude (sweep 1 min) 2G, X, Y, Z, When mounted with mounting screws.						
	SHOCK				Less than 20G						
	WEIGHT			Kg	2.9	3.2	5.8	2.9	3.2	5.8	2.9
	SIZE (W x H x D)			mm	200W and 400W units: 70 x 124 x 350. 800W units: 140 x 124 x 350 (Refer to outline drawing)						
EXTERNAL CONTROL FUNCTIONS	OUTPUT ON/OFF				By TTL Signal or Dry Contact (Refer to Instruction manual).						
	OUTPUT GOOD				Open collector (Refer to Instruction manual).						
	OUTPUT VOLTAGE PROGRAMMING				By Voltage (0-4V) or by Resistance (0-4K) (Refer to Instruction manual).						
	OUTPUT CURRENT PROGRAMMING				By Voltage (0-4V) or by Resistance (0-4K) (Refer to Instruction manual).						
	REMOTE SENSING				Maximum 0.5V drop on each load wire for model up to 60V and 2V for the 80V, 120V models						
	COMMUNICATION INTERFACE				RS232 and RS485 Built-in, IEEE488 Optional.						
APPROVALS	SAFETY STANDARDS				UL3111-1, EN61010-1						
	EMC STANDARDS				EN61326-1, IEC 61326-1, FCC part 15 (class A).						
CONDUCTED EMI					EN55022-B, FCC-B, VCCI-2						
RADIATED EMI					EN55022-A, FCC-A, VCCI-1						
SERIES OPERATION					Up to 2 units (Refer to Instruction manual).						
PARALLEL OPERATION					Master - Slave method; up to 5 units (Refer to Instruction manual).						
COOLING					Forced air by blower fan (Blower fan is mounted within unit).						
WITHSTAND VOLTAGE					Input - Chassis...2.0kVAC 1 min, Input - Output...3.0kVac 1 min, Output - GND...500VAC 1 min.						
ISOLATION RESISTANCE					More than 100MOhm at 25 ···C and 70% R.H.						

(*1) Minimum voltage is guaranteed to maximum 0.2% of the rated output voltage.

(*2) Minimum current is guaranteed to maximum 0.4% of the rated output current.

(*3) Time for recovery to within +/-50mV against current change of 50% to 100%.

(*4) From zero volts to full scale , resistive load and current setting at maximum.

(*5) From no load to full load , constant input voltage. (Measure with JEITA RC-9131 probe.)

(*6) From 85~132Vac or 170~265Vac constant load.

(*7) At cold start Ta=25 ···C.

(*8) Change in output over 8 hour interval constant line, load and ambient temperature following 30-minutes warm-up.

(*9) Given for control of the output via the serial communication or via front panel controls.

(*10) Inverter shut down method, manual reset (OVP will shut down output)

(*11) For cases where conformance to various safety specs. (UL, IEC, etc.) are required, to be described as 100-240VAC (50/60Hz) on name plate.

(*12) At 100V/200V and Maximum Output Power.
- When forced air cooling, refer to derating curve.

ZUP

ZUP20-20	ZUP20-40	ZUP36-6	ZUP36-12	ZUP36-24	ZUP60-3.5	ZUP60-7	ZUP60-14	ZUP80-2.5	ZUP80-5	ZUP120-1.8	ZUP120-3.6
0-20		0-36			0-60			0-80		0-120	
0-20	0-40	0-6	0-12	0-24	0-3.5	0-7	0-14	0-2.5	0-5	0-1.8	0-3.6
400	800	216	432	864	210	420	80	200	400	216	432
								0.005%+4mV			
								0.005%+2mV			
5	5	5	5	5	5	5	5	20	20	20	20
50	80	50	50	70	50	50	60	70	70	80	80
0.2		0.2			0.2			0.2		0.2	
400		500			750			800		1000	
50	60	50	50	60	50	50	60	100	100	100	100
50	50	50	50	50	50	50	70	60	60	80	80
0.01%+5mA	0.07%+10mA	0.01%+5mA	0.01%+5mA	0.07%+10mA	0.01%+5mA	0.01%+5mA	0.07%+10mA	0.01%+5mA	0.01%+5mA	0.01%+5mA	0.01%+5mA
0.01%+2mA	0.01%+5mA	0.01%+2mA	0.01%+2mA	0.01%+5mA	0.01%+2mA	0.01%+2mA	0.01%+5mA	0.01%+2mA	0.01%+2mA	0.01%+2mA	0.01%+2mA
30	60	7.5	15	30	5	10	20	5	5	5	5
0.02%+5mA	0.05%+10mA	0.02%+5mA	0.02%+5mA	0.05%+10mA	0.02%+5mA	0.02%+5mA	0.05%+10mA	0.02%+5mA	0.02%+5mA	0.02%+5mA	0.02%+5mA
0.02%+12mV		0.02%+20mV			0.02%+35mV			0.02%+50mV		0.02%+80mV	
0-24		0-40			0-66			0-88		0-132	
5.6/2.7	11.2/5.4	2.9/1.4	5.6/2.7	11.2/5.4	2.9/1.4	5.6/2.7	11.2/5.4	2.6/1.3	4.9/2.4	2.9/1.4	5.3/2.6
15	30	15/30 (*7)	15	30	15/30 (*7)	15	30	15/30 (*7)	15	15/30 (*7)	15
79/83	79/82	76/80	80/84	80/84	75/79	80/84	80/84	78/82	83/87	78/82	82/86
3.2	5.8	2.9	3.2	5.8	2.9	3.2	5.8	2.9	3.2	2.9	3.2

ZUP

Outline Drawing

[ZUP 200W/400W Units]

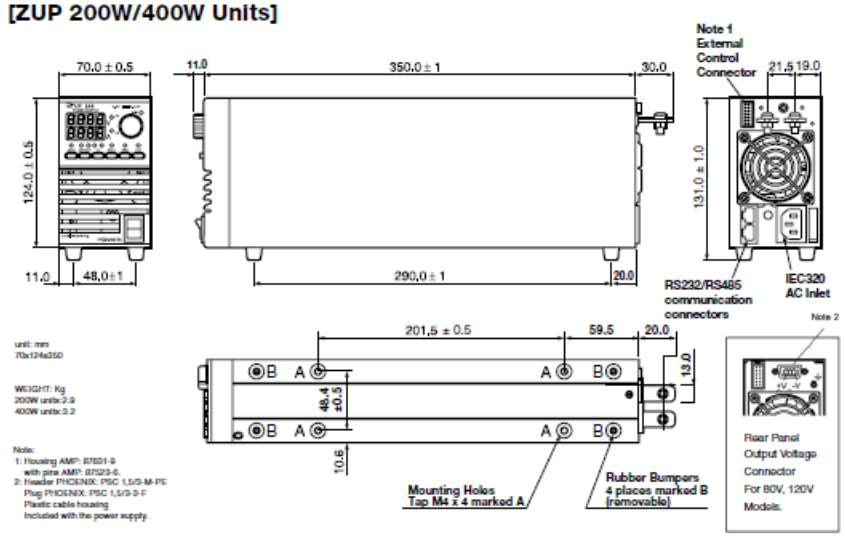

[ZUP 800W Unit]

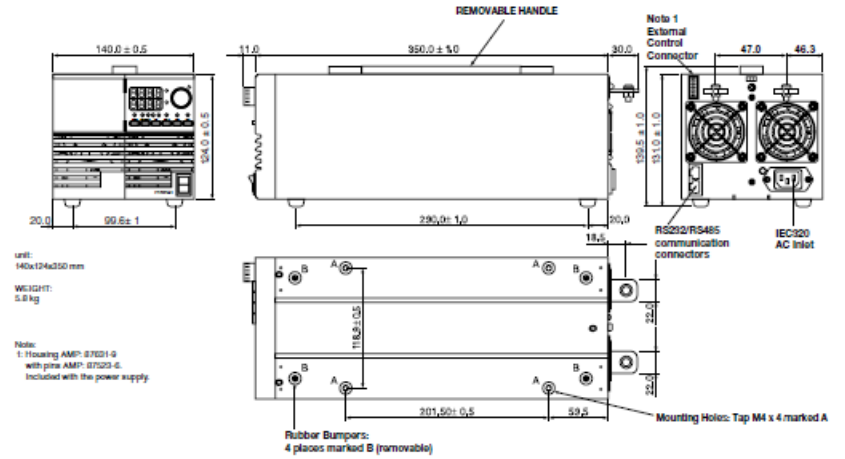

ZUP

Accessories / optional items (refer to the attached diagram for appearance)

Accessories

1. AC Cord Sets

Three optional cords are possible according to order:

Region	AC Cord	Power Supply Connector	Wall Plug	P/N
				ZUP / J
Europe	10A / 250Vac L =2m	IEC320-C13	INT'L 7 / VII	ZUP / E
				ZUP / O

North America

Europe

SI-32 Standard

2. Communication Cable

RS232/RS485 cable is used to connect the power supply to the PC controller

Mode	PC connector	Communication cable	Power Supply Connector	P/N
RS232	DB-9	Shield Ground , L=1m	EIA / TIA-568A (RJ-45)	ZUP/NC401
RS232	DB-25	Shield Ground , L=1m	EIA / TIA-568A (RJ-45)	ZUP/NC403

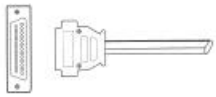

DB-25 (female connector)

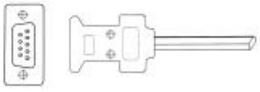

DB-9 (female connector)

EIA/TIA (RJ-45)

3. ZUP serial link cable

Used to chain Power Supply to Power Supply from a serial communication bus

Mode	Communication cable	Power Supply Connector Remote IN / OUT	P/N
RS485	Shield Ground , L = 50cm	EIA / TIA-568A (RJ-45)	ZUP / W

ZUP

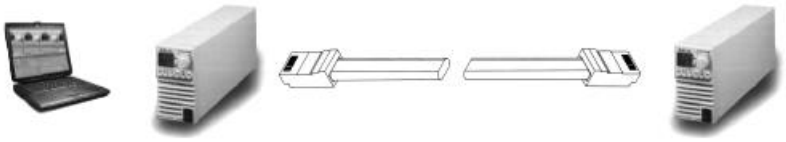

Options (200W, 400W, 800W Models)

1. FRONT PANEL OUTPUT JACKS
P/N: ZUP / L

Outline Drawing: Physical Dimensions in mm.
ZUP 200W/400W Units: 70x153x405.9
ZUP 800W Units: 140x153x405.9

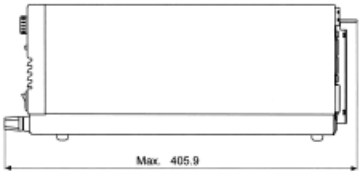

Up to 20A output current via front panel jacks.

2. ZUP ASSEMBLIES
Dual Output Packing 200W/400W models
P/N: ZUP/NL200

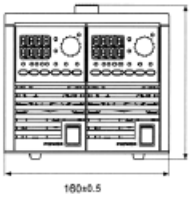

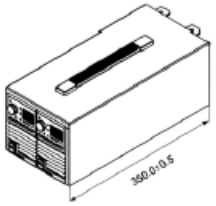

3. 19" RACK MOUNTED ATE AND OEM UP TO 2.4 KW
Up to six power units can be assembled into a 19 , 3U rack, kit P/N NL100.
In cases where the entire rack is not occupied with power units, NL101 blank panels can be installed.
P/N: ZUP/NL100

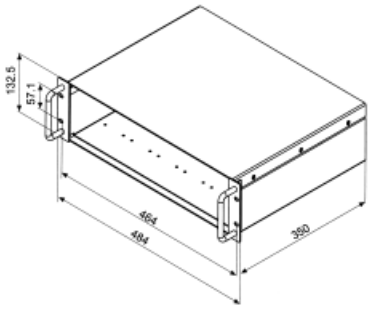

ZUP

Application examples

ZUP Configurations

BENCH TOP POWER SUPPLY

PARALLEL OPERATION

Master - Slave method: Active current sharing up to 5 units.

REMOTE PROGRAMMING VIA RS232

Up to 31 ZUP units can be controlled via RS232 interface.

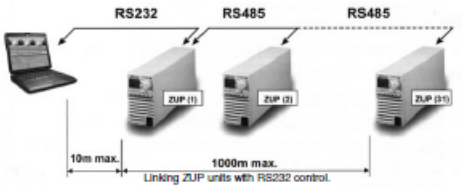

REMOTE PROGRAMMING VIA RS485

Up to 31 ZUP units can be controlled via RS485Interface.
For operation environments that require high noise immunity or long distance communication, it is recommended to use the built- in RS485Interface.

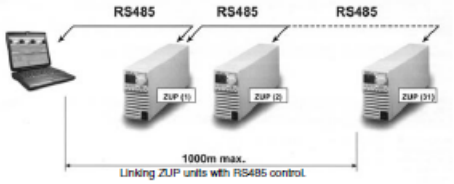

Remote Programming Via GPIB.

GPIB⇨RS485 CONTROLLER

The GP485 is a high performance serial to GPIB interface
It enables a ZUP series with RS485 port to be a Talker, Listener, or controller on the GPIB

* Controls up to 31 ZUP units through a single GPIB address.
* Conforms to all versions of the IEEE488 standard, including IEEE488.2.
* 19 racking possibility.
* Application software - LabView, LabWindows.

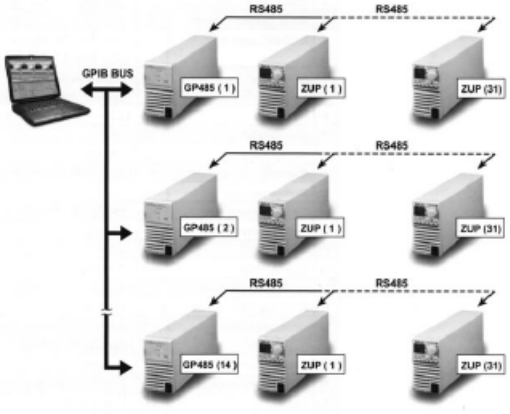

ZUP

ZUP SERIES

TDK·Lambda

Rack Mounted ATE and OEM up to 2.4KW

Six units can be assembled into 19-inch rack / 3U high
to meet your configuration requirements

Power Modules Table

Module Type	200W	400W	800W
0 – 6V	33A	66A	132A
0 – 10V	20A	40A	80A
0 – 20V	10A	20A	40A
0 – 36V	6A	12A	24A
0 – 60V	3.5A	7A	14A
0 – 80V	2.5A	5A	
0 – 120V	1.8A	3.6A	
19"rack width	1 / 6 width	1 / 6 width	2 / 6 width

ZUP

The TDI Dynaload XBL 50-150-800 load box specifications were downloaded directly from the TDI Power website [51].

XBL Series 800

- Excellent Programming Accuracy
- High Speed Programmable Slew Rate
- Ethernet Control
- Closed Box Calibration
- RBL Command Support
- Pulse Load Shaping
- Full Range Switching

The XBL Dynaload Series features 800, 2000 and 4000 watt models with wide range voltage inputs and sophisticated computer programming via GPIB, Ethernet, or RS232. These units feature an integrated web page for local system operation and control.

Individual models are available for specialized low voltage high current applications. High voltage models up to 1000 volts are also available.

All models include easy to apply master slave parallel capabilities and closed box calibration. Higher power models incorporate variable speed forced air cooling to assure a quiet environment.

General Specifications

OPERATION

Constant Current: 0 to selected full scale current
Prog. Accuracy: .1% of setpoint ±5ma
Resolution(IEEE): .0015% of selected full scale

Constant Resistance: Constant Resistance mode operates in Amps/Volt, IEEE units entered in ohms or A/V
Prog. Accuracy: 1% of setpoint +- 5 ma
Resolution(IEEE): .0015% of selected full scale

Constant Voltage: 0 to selected selected full scale
Prog. Accuracy: 1% of setpoint +- 250mv
Resolution(IEEE): .0015% of selected full scale

Constant Power: 0 to full scale power
Prog. Accuracy: 1% of setpoint +-250mw
Resolution(IEEE): .0015% of full scale power

ANALOG MODE

Ext. Prog: 0 to 10 Volts input yields 0 to selected full scale Input Impedance: 330k Ohms

PULSE MODE

Frequency: 1Hz to 3.5kHz
Duty Cycle: 0 - 100%
Minimum Pulse Width: 125usec

Adjustable Slew Rate:
Max: 0 to full scale in 10µS - adjustable

OUTPUT SIGNALS

Current Sample Output:
Scaling: 10 Volts = selected full scale
Accuracy: ±0.5% of selected full scale

MISCELLANEOUS

AC Input: User Selectable 100VAC,120VAC, 200VAC, 240VAC, ±10%, 48 - 62 Hz @ 350W
Ambient Temp: 0°C to 40°C

PROTECTION

Current Limit:
Analog Models: Approximately 105% of selected full scale current
Range(IEEE): 0-105% of selected full scale
Resolution(IEEE): 0.4% of selected full scale

Voltage Limit:
Analog Models: Load disconnect at 105% of selected full scale voltage
Range(IEEE): 0-105% of selected full scale
Resolution(IEEE): 0.4% of selected full scale

Power Limit:
Range(IEEE): 0 - 840 Watts
Resolution(IEEE): 0.4%

Thermal: Load disconnect at internal temperature of 105°C

Undervoltage: Load inhibited at less than1 Volt, when enabled

COMMUNICATION CHANNEL READBACK

Current:
Resolution: .0015% of Selected Full Scale
Accuracy(Range): 0.1% ±5ma

Voltage:
Resolution: .0015% of Selected Full Scale
Accuracy(Range): 0.1% ±5ma

Power:
Resolution: 1 Watt
Accuracy: 0.1% ±5ma

Communication Modes:
IEEE 488
RS 232
Ethernet (HTTP, TCP, & Telnet)

TDI POWER — *Innovative Test Systems... Global Test Solutions*

SAFE OPERATING AREA & SPECIFICATIONS

XBL 50-150-800

OPERATING RANGES (FULL SCALES)
Voltage: 10 Volts, 20 Volts, 50 Volts
Current: 2 Amps, 20 Amps, 150 Amps
Power: 800 Watts
Short Circuit: 0.0026 Ohms max.

CONSTANT RESISTANCE RANGES

High Ohms Mode

Range	2A	20A	120A
10V	0-.1 A/V	0-1 A/V	0-7.5 A/V
20V	0-.05 A/V	0-.5 A/V	0-3.75 A/V
50V	0-.02 A/V	0-.2 A/V	0-1.5 A/V

Low Ohms Mode

Range	2A	20A	120A
10V	0-1 A/V	0-10A/V	0-75 A/V
20V	0-.5 A/V	0-5 A/V	0-37.5 A/V
50V	0-.2 A/V	0-2 A/V	0-15 A/V

INPUT CHARACTERISTICS:

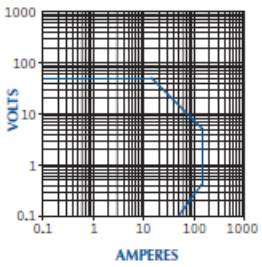

XBL 100-120-800

OPERATING RANGES (FULL SCALES)
Voltage: 10 Volts, 50 Volts, 100 Volts
Current: 2 Amps, 20 Amps, 120 Amps
Power: 800 Watts
Short Circuit: 0.007 Ohms max.

CONSTANT RESISTANCE RANGES

High Ohms Mode

Range	2A	20A	120A
10V	0-.1 A/V	0-1 A/V	0-6 A/V
50V	0-.02 A/V	0-.2 A/V	0-1.2 A/V
100V	0-.01 A/V	0-.1 A/V	0-.6 A/V

Low Ohms Mode

Range	2A	20A	120A
10V	0-1 A/V	0-10A/V	0-60 A/V
50V	0-.2 A/V	0-2 A/V	0-12 A/V
100V	0-.1 A/V	0-1 A/V	0-6 A/V

INPUT CHARACTERISTICS:

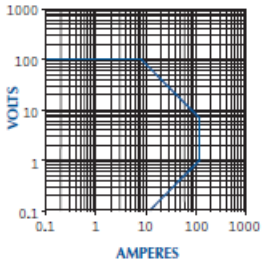

XBL 400-120-800

OPERATING RANGES (FULL SCALES)
Voltage: 20 Volts, 200 Volts, 400 Volts
Current: 2 Amps, 20 Amps, 120 Amps
Power: 800 Watts
Short Circuit: 0.03 Ohms max.

CONSTANT RESISTANCE RANGES

High Ohms Mode

Range	2A	20A	120A
20V	0-.05 A/V	0-.5 A/V	0-3 A/V
200V	0-.005 A/V	0-.05 A/V	0-.3 A/V
400V	0-.0025 A/V	0-.025 A/V	0-.15 A/V

Low Ohms Mode

Range	2A	20A	120A
20V	0-.5 A/V	0-5 A/V	0-30 A/V
200V	0-.05 A/V	0-.5 A/V	0-3 A/V
400V	0-.025 A/V	0-.25 A/V	0-1.5 A/V

INPUT CHARACTERISTICS:

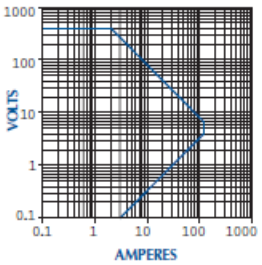

XBL 600-40-800

OPERATING RANGES (FULL SCALES)
Voltage: 20 Volts, 200 Volts, 600 Volts
Current: 2 Amps, 20 Amps, 40 Amps
Power: 800 Watts
Short Circuit: 0.035 Ohms max.

CONSTANT RESISTANCE RANGES

High Ohms Mode

Range	2A	20A	40A
20V	0-.05 A/V	0-.5 A/V	0-1 A/V
200V	0-.005 A/V	0-.05 A/V	0-.1 A/V
400V	0-.0025 A/V	0-.025 A/V	0-.05 A/V

Low Ohms Mode

Range	2A	20A	40A
20V	0-.5 A/V	0-5 A/V	0-10 A/V
200V	0-.05 A/V	0-.5 A/V	0-1 A/V
400V	0-.025 A/V	0-.25 A/V	0-.5 A/V

INPUT CHARACTERISTICS:

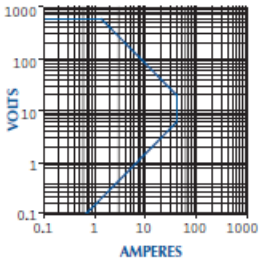

800W Outline

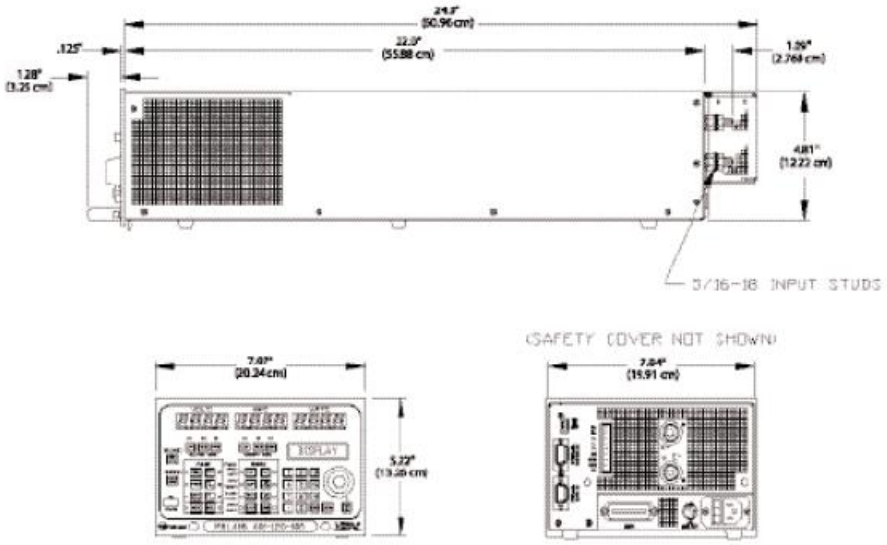

Appendix H
Glossary of Terms

Important terms and ideas are presented below to effectively convey the concepts involved with battery characterization and performance testing. These terms and ideas offer a basic understanding of the concepts that are to be covered in detail in the following sections.

Battery Cell – The simplest form of a battery consisting of two electrodes, a separator, and electrolyte encased in sealed packaging.

Battery Pack – The grouping of several battery cells in parallel or series configurations to increase the capacity or voltage output compared to a single cell.

Rated Battery Capacity – The amperes available during a one-hour discharge of the battery for a given current; provided by the battery manufacturer.

Maximum Battery Capacity – Similar to the rated battery capacity, except it is determined from experimentation.

State of Charge (SOC) – An estimation of the remaining battery capacity available for discharge as a percentage of the maximum battery capacity.

Depth of Discharge (DOD) – An estimation of the extent to which the battery capacity has been consumed as a percentage of the maximum battery capacity. In other words, the depth of discharge is the complement of the state of charge.

C-rate – A referential expression for current that depends on the battery capacity. For example, a 20 Ah battery would be subjected to C/2, 1C, and 2C rates according to 10 A, 20 A, or 40 A, respectively.

Resistance – The resistance of a battery to the flow of current, measured in Ohms, developed within the battery cell and through any connections between battery cells in battery packs.

Open Circuit Potential (OCP) – The equilibrium potential difference between the positive and negative electrodes of a battery, measured while the battery is not under load.

Coulombic Efficiency – A representation of the lithium ions lost to side-reactions during the charging process of a battery. Therefore, the coulombic efficiency is a percentage of the available battery capacity of discharge compared to the battery capacity previously charged to the battery.

Battery Characterization – A series of test procedures to characterize the battery open circuit voltage and resistance as a function of the state of charge, as well as the coulombic efficiency. The tests can be conducted at different C-rates and temperatures to account for their effects on the battery characteristics.

Capacity Fade – The loss of cycleable lithium in the battery that reduces the overall capacity over the life of a battery.

Power Fade – The increase in battery resistance over the life of the battery that decreases the power capability for a given current.

Calendar Aging – Irreversible capacity fade of the battery during storage according to the storage conditions, such as voltage and temperature.

Battery Performance Testing – A series of test procedures that determine how the battery performs in a given application with respect to energy and power capabilities, and capacity and power fade.

Beginning of Life (BOL) – A point in time that signifies the beginning of the battery performance testing period, at which point the battery characteristics will have already been defined.

End of Life (EOL) – A point in time that signifies the ending of the battery performance testing period, usually defined according to the extent of capacity fade.

Battery Cycle Life – The amount of time, cycles, or capacity throughput that a battery can endure in a given application, determined from the battery performance testing between the beginning of life and end of life conditions.

Battery Scaling – The extrapolation of battery characteristics and performance results of a tested battery to that of a differently sized and untested battery.

Appendix I
Scaling Analysis

Introduction

Cell performance testing provides information on how the battery will perform in its application. The testing results can be used to develop a battery model to predict its performance. However, the model depends on the cell that was tested and if that cell were changed then the model is no longer statistically valid. Inevitably, the new cell would need to be tested as well. While designing a battery pack for a vehicle, one may take several sizes into consideration. Unfortunately, testing all of those cells can be labourious and time consuming. Therefore, it is desirable to develop a technique to scale the results from cell performance testing of a single cell to differently sized cell. Furthermore, the scaling analysis should extend from the performance of a single cell to the performance of a battery pack. The objective of the scaling analysis is to develop the capability to predict the performance of a battery pack for a given cell size and configuration.

Cell to Cell Scaling

The concept behind cell-cell scaling is to generate a predictive model for a small, simple battery that can be modified to predict performance for a larger, more sophisticated battery. To do so, the model must consider the materials within the cells and the physical dimensions of the cells. Kwon *et al.* proposed such a system for a lithium-polymer battery that will be presented below [52].

To represent the scaling basis, a single battery cell is considered with two electrodes separated by a polymer electrolyte (Figure I.1).

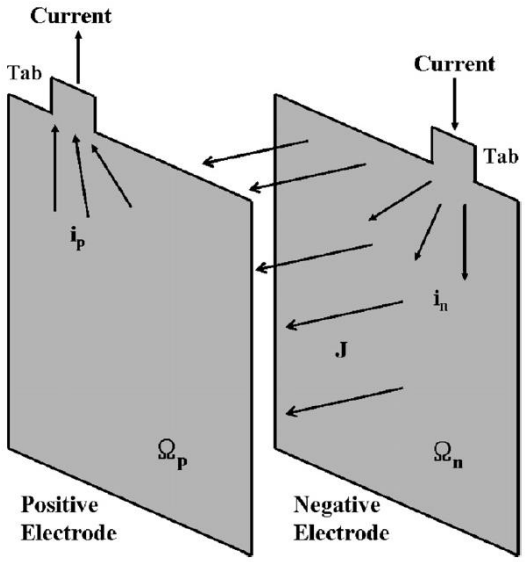

Figure I.1 Schematic of cell used for scaling basis [52]

As the cell is discharged current enters the negative electrode through the tab and disperses across the electrode surface. Imbalance in the linear current densities on the electrode surface cause a current density to flow through the separator and collect on the surface of the positive electrode. The current accumulates towards the positive electrode tab and exits the cell. This process can be presented mathematically as follows.

Conservation of current on the surface of the electrodes dictates that the distribution of linear current densities is equivalent to the current density leaving the electrode,

$$\nabla\overrightarrow{\iota_p} - J = 0 \tag{I.1}$$

$$\nabla\overrightarrow{\iota_n} + J = 0 \tag{I.2}$$

where $\overrightarrow{\iota_p}$ and $\overrightarrow{\iota_n}$ are the linear current density vectors on the positive and negative electrode, respectively, and J is the current density between the electrodes.

Unfortunately, the distribution of linear current density vectors on the electrode surface is difficult to measure. Thus, the linear current density vectors are expressed in terms of potentials using Ohms law,

$$\overrightarrow{\iota_p} = -\frac{\nabla V_p}{r_p} \tag{I.3}$$

$$\overrightarrow{\iota_n} = -\frac{\nabla V_n}{r_n} \tag{I.4}$$

where V_p and V_n are potentials, and r_p and r_n are resistances on the positive and negative electrode surfaces, respectively.

The resistances of the electrodes are determined by the inverse of the combined active material and current collector electrical conductivity,

$$r_{p/n} = \frac{1}{t_a S_a + t_c S_c} \tag{I.0.1}$$

where the t_a and t_c are the thicknesses, and S_a and S_c are the electrical conductivities of the active material and current collector, respectively.

Equations (I.1) and (I.2) can be modified using equations (I.3) and (I.4) to relate the current density within the cell to the electrode potentials.

$$\nabla^2 V_p + r_p J = 0 \tag{I.6}$$

$$\nabla^2 V_n - r_n J = 0 \tag{I.7}$$

The boundary conditions for the positive electrode are presented below, where n is the normal to the boundary, I_0 is the current through the tab, and L is the length of the tab.

$$\frac{\partial V_p}{\partial n} = 0 \tag{I.8}$$

$$\frac{\partial V_p}{\partial n} = -\frac{r_p I_0}{L} \tag{I.9}$$

The first boundary condition (I.8) applies to all boundaries except for the boundary at the tab. It implies that there is no current flow through those boundaries. Additionally, the second boundary condition (I.9) applies only to the boundary at the tab and suggests that the current flow across the boundary is proportional to the battery current provided to the load during a discharge.

The boundary conditions for the negative electrode are presented below, where the first boundary condition indicates a lack of current flow through all boundaries except for the boundary at the tab

(I.10), while the second boundary condition fixes the negative electrode tab potential at zero (I.11). Fixing the tab potential to zero effectively sets a reference potential for the cell.

$$\frac{\partial V_n}{\partial n} = 0 \tag{I.10}$$

$$V_n = 0 \tag{I.11}$$

To solve the system of equations presented thus far, a relationship must be derived between the electrode potentials and the current density across the separator. Tiedemann and Newman [53, 54] proposed that the relationship depends on the polarization characteristics of the electrodes, presented below.

$$J = Y(V_p - V_n - U) \tag{I.12}$$

However, Y and U are fitted functions dependent on the DOD of the active material defined by Gu [55],

$$U = \beta_0 + \beta_1(DOD) + \beta_2(DOD)^2 + \beta_3(DOD)^3 \tag{I.13}$$

$$Y = \beta_4 + \beta_5(DOD) + \beta_6(DOD)^2 \tag{I.14}$$

where the β's are parameters to be determined through experimentation. Furthermore, the DOD can be calculated from the current density across the separator according to the following equation, where A is the area of the electrode.

$$DOD = \frac{A\int_{t_0}^{t} Jdt}{Q_T} \tag{I.15}$$

The finite element method is used to solve the set of equations presented above to obtain the potential distribution over the surface of the electrodes. Therefore, given a battery current represented by the current flowing through the tabs, I_0, the cell potential response can be predicted. Assuming the parameters from equations (I.13) and (I.14) are fitted accurately; Kwon *et al.* showed that the simulated battery potential response for CC discharging accurately predicted the experimental results [52].

It was later determined that by using the fitted parameters for a smaller cell, a larger cell's performance could be predicted by accounting for the change in electrode size [56]. However, this

conclusion was restricted to the assumptions that the larger and smaller cells were manufactured with the same materials and processes; making them identical except for their physical dimensions. In many cases, battery manufacturing processes can vary dramatically between batches of cells of the same size, let alone cells of different sizes. Therefore, caution is recommended when applying this cell-cell scaling method.

Cell to Pack Scaling

It is convenient to perform characterization and performance testing on single cells because the equipment required only needs to satisfy the voltage and current capabilities of the cell being tested. Testing a battery pack increases voltage and current requirements; increasing the cost of the equipment. For these two reasons, it is proposed that battery cell test results can be scaled to predict battery pack performance. Commonly, a packing factor is used to scale the mass and/or volume of a single cell to that of a pack by including wiring, insulation, thermal management materials, and pack casing. The packing factor will be greater than unity, since unity would suggest that only battery cells were present in a pack. Additionally, a battery size factor is used to scale the power, energy, and life capabilities of a cell to satisfy pack requirements [4]. Essentially, the battery size factor represents the number of cells required in the pack to satisfy performance demands [4]. However, the battery size factor does not account for any change in performance by connecting multiple cells together. Much like how the packing factor accounts for the extra mass or volume of a pack, there needs to be battery performance factors that account for deviations in performance unaccounted for using the battery size factor.

The desired purpose of the battery performance factors are to aid in the accurate prediction of battery pack performance from battery cell test results. Dubarry *et al.* claim that the variation between cell capacities causes significant performance differences between the scaled battery pack simulations and the experimental results [13]. Furthermore, Dubarry *et al.* propose that a resistance look-up-table (LUT) can be generated as a function of SOC and C-rate [13]. Such a resistance LUT could be normalized to a cell's capacity by measuring the capacity of each cell in the pack. A battery resistance factor is used for each cell in the pack to modify its resistance LUT. It was found that for a small pack size, the battery resistance factor was effective at lowering the deviation in potential responses between simulated results and experimental data (Figure I.2) [13]. The total capacity discharged by

the simulated pack decreased from 6.5% error to 1.6% error compared to the experimental results [13].

(a) (b)

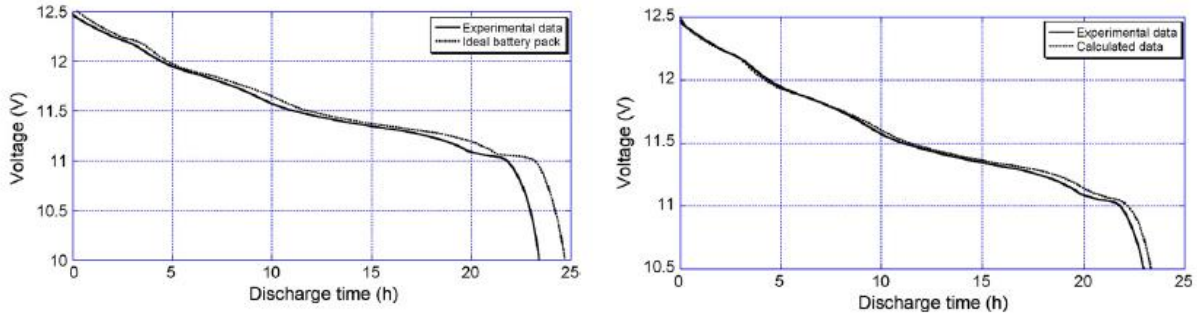

Figure I.2 The simulated battery pack potential response compared to experimental results (a) without the battery resistance factor, and (b) with the battery resistance factor

Although the battery resistance factor appears to be effective for small battery packs, it may not be capable of predicting performance issues for larger packs. Additionally, testing each cell in a battery pack for its maximum capacity can be tedious and costly. Therefore, the following technique is proposed to obtain the battery resistance factors without having to cycle the batteries individually:

- Charge the battery pack according to the standard charging procedure for a cell after applying the battery size factor.
- Let the pack rest for 2 h or until the voltage change is insignificant over a 30 min time period.
- Demand a C/25 discharge rate, and measure the initial voltages of each cell.
- Let the pack rest for 2 h or until the voltage change is insignificant over a 30 min time period.
- Demand a 1C discharge rate, and measure the initial voltages of each cell.
- Take the slope between those two voltage readings according to the discharge rate demanded to find the normalized polarization resistance.
- Determine the battery resistance factors, θ_i, by comparing the cells' normalized polarization resistances, $R_{np,i}$, with the reference cell's normalize polarization resistance, $R_{np,0}$.

$$\theta_i = \frac{R_{np,i}}{R_{np,0}} \tag{I.16}$$

- Discharge the battery pack according to the standard discharge procedure for a cell after applying the battery size factor and stop when the cut-off potential is reached.
- Let the pack rest for 2 h or until the voltage change is insignificant over a 30 min time period.
- Measure each battery cell's OCP and determine the cell's SOC from the OCP curve measured in the cell characterization tests.
- Determine each cell's maximum capacity, $Q_{T,i}$, using the cell's SOC, and the capacity processed, Q_P, during the discharge.

$$Q_{T,i} = \frac{100 Q_P}{SOC} \tag{I.17}$$

Such a test plan would require one cycle, whereas the tests proposed by Dubarry *et al.* would require as many cycles as there are cells in the pack. Therefore, the proposed method would save time and costs.

Appendix J
Electrochemical VSSD Model

Electrochemical Model Development

A fundamental electrochemical model has been developed in an attempt to predict battery performance and aging throughout its lifetime. The model has three levels that define the physical systems within the battery (Figure J.1). The macro level contains a positive electrode, negative electrode, and separator; the micro level contains four particle groups for each electrode; and the nano level contains the SEI layer. The electrodes are macroscopically defined according to Newman's porous-electrode theory [57], and microscopically using variable solid-state diffusivity [32].

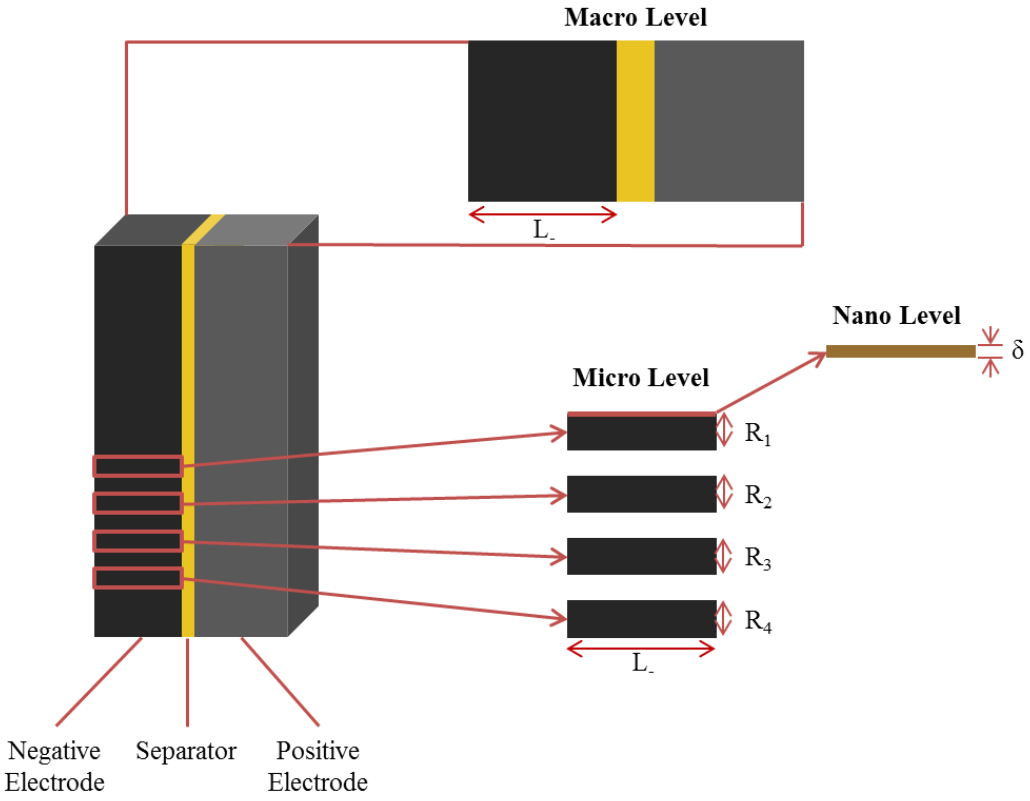

Figure J.1 Visual representation of the electrochemical model and its various dimensions

Porous-Electrode Theory

The complexity associated with modeling the porous materials is simplified using a one-dimensional model, ignoring the pore geometry. Within the cell the pores of the electrodes are filled by the electrolyte, resulting in the solid and solution phases. Therefore, the electrodes and electrolyte are considered as two materials in superposition at any point in space and time.

Considering a unit volume within the electrode, there is conservation of charge. Thus, any charge flowing into the solid phase is negated by the charge flowing out of the solution phase according to electroneutrality; where i_1 is the transfer current density in the solid phase and i_2 is the transfer current density in the solution phase.

$$\nabla \cdot i_1 + \nabla \cdot i_2 = 0 \tag{J.1}$$

In the electrode, the average transfer current density from the solid phase to the solution phase (i_n) describes the relationship between an increase in ionic current equivalent to a decrease in the electronic current; where a is the specific interfacial area.

$$\nabla \cdot i_1 = -a i_n \tag{J.2}$$

$$\nabla \cdot i_2 = a i_n \tag{J.3}$$

Charge migration in the solid phase is governed by Ohm's law; where σ_{eff} is the effective conductivity of the solid phase, and Φ_1 is the solid phase electric potential.

$$i_1 = -\sigma_{eff} \nabla \Phi_1 \tag{J.4}$$

Electronic conductivity of the electrode material (σ) is corrected for its porosity and tortuosity using the Bruggeman expression; where ε is the electrode porosity and γ is the Bruggeman correction factor.

$$\sigma_{eff} = \sigma(1 - \varepsilon)^{\gamma} \tag{J.5}$$

Charge-transfer reaction kinetics at the solid/solution interface are described by the Butler-Vomer equation; where α_a and α_c are the anodic and cathodic transfer coefficients respectively, R is the university gas constant, T is the absolute temperature, η_s is the surface overpotential, and i_0 is the exchange current density.

$$i_n = i_0 \left[exp\left(\frac{\alpha_a F \eta_s}{RT}\right) - exp\left(-\frac{\alpha_c F \eta_s}{RT}\right) \right] \tag{J.6}$$

The exchange current density is an agglomeration of several terms defined later when describing the variable solid-state diffusivity model.

The surface overpotential consists of the solid phase electric potential, solution phase electric potential (Φ_2), and the open circuit potential of the cell (U).

$$\eta_s = \Phi_1 - \Phi_2 - U \tag{J.7}$$

Within the solution phase, dilute solution theory is not applicable for most lithium ion batteries because the electrolyte concentration exceeds the theory's limitations. Additionally, multicomponent diffusion is used to describe an electrolyte consisting of three or more species. For simplification, the electrolyte is assumed to consist of two dissociative species within a solvent for a total of three species. Therefore, concentrated solution theory and multicomponent diffusion are used to govern the solution phase; where c_i is the concentration of species i, μ_i is the electrochemical potential of species i, K_{ij} is the friction coefficient for the interaction between species i and j, and v_i is the velocity of species i with respect to a reference velocity.

$$c_i \nabla \mu_i = \sum_{j \neq i} K_{ij}\left(v_j - v_i\right) \tag{J.8}$$

The friction coefficient represents an agglomeration of terms related to the concentration of species (c_i and c_j), total concentration (c_T) and the diffusion coefficient describing species interaction ($\mathcal{D}_{ij}$).

$$K_{ij} = \frac{RTc_i c_j}{c_T \mathcal{D}_{ij}} \tag{J.9}$$

The total concentration is a sum of all the species concentrations, including that of the solvent.

$$c_T = \sum_i c_i \tag{J.10}$$

Additionally, Newton's third law dictates that the diffusion (friction) coefficients describing species interaction are equal regardless of which species is acting on the other.

$$\mathcal{D}_{ij} = \mathcal{D}_{ji} \tag{J.11}$$

For a binary electrolyte such as $LiPF_6$, common in lithium ion batteries, equation 8 produces two independent flux densities; where '+' is the cation, '−' is the anion, and '0' is the solvent, ν_+ and ν_- are the number of moles of cations and anions dissociated into a solvent from a molecule of

electrolyte with their sum represented by ν, $\mathcal{D}$ is the electrolyte diffusion coefficient based on a thermodynamic driving force, c is the electrolyte concentration, μ_e is the chemical potential of the electrolyte, z_+ and z_- are the cation and anion charge numbers, and t_+^0 and t_-^0 are the cation and anion transference numbers.

$$N_+ = c_+ v_+ = -\frac{\nu_+ \mathcal{D} c_T}{\nu R T c_0} c \nabla \mu_e + \frac{i_2 t_+^0}{z_+ F} + c_+ v_0 \tag{J.12}$$

$$N_- = c_- v_- = -\frac{\nu_- \mathcal{D} c_T}{\nu R T c_0} c \nabla \mu_e + \frac{i_2 t_-^0}{z_- F} + c_- v_0 \tag{J.13}$$

The first term describes the diffusive flux density of the electrolyte. The second term describes the species migration within the solution phase. The final term describes the species convection according to the solvent velocity; however the solvent velocity is often negligible. Ultimately, the convection term is typically excluded from further consideration.

The diffusion coefficient based on a thermodynamic driving force is defined as a combination of the diffusion coefficients describing species interaction.

$$\mathcal{D} = \frac{(z_+ - z_-)\mathcal{D}_{0+}\mathcal{D}_{0-}}{z_+ \mathcal{D}_{0+} - z_- \mathcal{D}_{0-}} \tag{J.14}$$

The transference numbers are defined with respect to the solvent velocity.

$$t_+^0 = 1 - t_-^0 = \frac{z_+ \mathcal{D}_{0+}}{z_+ \mathcal{D}_{0+} - z_- \mathcal{D}_{0-}} \tag{J.15}$$

The gradient of chemical potential of the electrolyte can be expressed using the concentration gradient of the electrolyte; where f is the mean molar activity coefficient of the electrolyte.

$$\frac{1}{\nu R T} c \nabla \mu_e = \left(1 + \frac{d \ln f}{d \ln c}\right) \nabla c \tag{J.16}$$

Herein, α is defined as the electrolyte activity correction factor.

$$\alpha_e = \left(1 + \frac{d \ln f}{d \ln c}\right) \tag{J.17}$$

The material balance for a species contains a homogenous production term (R) that describes the electrochemical reaction at the solid/solution interface. In a real system, the reaction would be defined

as a boundary condition; however, porous electrode theory defines the solid and solution phases according to superposition and thus the reaction is defined in the production term.

$$\frac{\partial c_i}{\partial t} = -\nabla N_i + R_i \tag{J.18}$$

Since the production term describes the electrochemical reaction at the solid/solution interface, it is directly proportional to the average transfer current density from the solid phase into the solution phase.

$$R_i = \frac{a i_n}{F} \tag{J.19}$$

To derive the material balance of the electrolyte, equations (J.12), (J.13), and (J.19) must be substituted into equation (J.18) to yield two expressions; one for each species. The two resulting equations can be rearranged to solve for the electrolyte concentration; where D_{eff} is the effective electrolyte diffusion coefficient. Also, the material balance of the electrolyte must also be adjusted to account for the electrode porosity.

$$\varepsilon \frac{\partial c}{\partial t} = \nabla\left(D_{eff} \varepsilon \nabla c\right) - \frac{i_2 \nabla t_+^0}{F} + \frac{i_n a (1 - t_+^0)}{F} \tag{J.20}$$

The effective diffusion coefficient for the electrolyte attempts to correct the diffusion coefficient based on a thermodynamic driving force using the Bruggeman expression to account for the porous electrode; where α is the electrolyte activity correction factor.

$$D_{eff} = \frac{\alpha_e \mathcal{D} c_T}{c_0} \varepsilon^{\gamma - 1} \tag{J.21}$$

A mass balance of the electrolyte around the separator is similar to equation (J.20), except there is no surface reaction taking place; thus the production term does not exist. Also, the porosity of the separator (ε_s) is different from that at the electrodes.

$$\varepsilon_s \frac{\partial c}{\partial t} = \nabla\left(D_{eff} \varepsilon_s \nabla c\right) - \frac{i_2 \nabla t_+^0}{F} \tag{J.22}$$

Considering the reference electrode reaction offers a starting point for determining the transfer current in the solution phase; where s_+ is the stoichiometric value of the cation, M_+ is a symbol representing the chemical formula of the cation, and n is the number of electrons.

$$s_+ M_+^{z_+} + s_- M_-^{z_-} + s_0 M_0 \rightleftharpoons n e^- \tag{J.23}$$

The thermodynamic principles surrounding the reference electrode reaction relate electrochemical potentials to the potential gradient in the solution phase.

$$s_+ \nabla \mu_+ + s_- \nabla \mu_- + s_0 \nabla \mu_0 = -nF \nabla \Phi_2 \tag{J.24}$$

The electrochemical potential gradient of the solvent is set to zero according to the Gibbs-Duhem equation. Furthermore, the equation can be rearranged into a form easier to work with.

$$-F \nabla \Phi_2 = \left(\frac{s_+}{n \nu_+} - \frac{s_0 c}{n c_0} \right) \nabla \mu_e - \frac{1}{z_-} \nabla \mu_- \tag{J.25}$$

The electrochemical potential gradient of the anion can be substituted for after deriving an expression from the combination of equations (J.8), (J.12), and (J.13); where κ is the ionic conductivity of the solution.

$$-\frac{1}{z_-} \nabla \mu_- = \frac{F}{\kappa} i_2 - \frac{t_+^0}{z_+ \nu_+} \nabla \mu_e \tag{J.26}$$

The ionic conductivity depends on the interactions of the species the solution contains.

$$\frac{1}{\kappa} = \frac{-RT}{c_T z_+ z_- F^2} \left(\frac{1}{\mathcal{D}_{\pm -}} + \frac{c_0 t_-^0}{c_+ \mathcal{D}_{0-}} \right) \tag{J.27}$$

Equations (J.25) and (J.26) yield an expression that relates the transfer current density in the solution phase with the potential gradient in the solution phase. Also, the expression must be corrected for the porosity of the electrode using the Bruggeman expression.

$$i_2 = -\kappa \varepsilon^\gamma \left(\nabla \Phi_2 - \frac{2RT(1 - t_+^0)}{F} \alpha_e \nabla \ln c \right) \tag{J.28}$$

Finally, the transfer current through the separator is also defined by equation (J.28); however the ionic conductivity κ_s of the separator is different from that at the electrodes.

$$i_2 = -\kappa_s \varepsilon_s^\gamma \left(\nabla \Phi_2 - \frac{2RT(1 - t_+^0)}{F} \alpha_e \nabla \ln c \right) \tag{J.29}$$

Variable Solid-State Diffusivity Model

The porous electrode theory describes the macroscopic phenomena of the cell, with exception to the average transfer current density from the solid phase to the solution phase. The particle-scale phenomena are described by the VSSD. The VSSD model assumes that the particles contain a mixture of empty sites (S) and lithiated sites (LiS) within its lattice.

$$Li^+ + e^- + S \rightleftharpoons Li^+S^- \tag{J.30}$$

The objective of the VSSD model is to describe the concentration of LiS in the electrode while accounting for several particle groups within the electrode. Concentrated solution theory postulates that the flux density of LiS is dependent upon its chemical potential gradient; where c_{max} is the maximum concentration of LiS of the electrode, and $y_{LiS,k}$ is the normalized concentration of LiS in the kth particle group.

$$N_{LiS,k} = -c_{max}\frac{\mathcal{D}_{LiS}y_{LiS,k}}{RT}\nabla\mu_{LiS,k} \tag{J.31}$$

Rearranging, the flux equation takes on a simpler form as the Fickian diffusion coefficient (D_k) is used.

$$N_{LiS,k} = -D_k c_{max}\nabla y_{LiS,k} \tag{J.32}$$

The Fickian diffusion coefficient is then expressed according to the normalized activity correction factor.

$$D_k = \mathcal{D}_{LiS}\frac{\partial\mu_{LiS,k}}{\partial y_{LiS,k}} = \mathcal{D}_{LiS}\alpha_k \tag{J.33}$$

Additionally, the normalized activity correction factor can also be derived by applying the Gibbs-Duhem equation for a binary system to the equilibrium potential of the electrode (U_k). The equilibrium potential can be determined experimentally.

$$\alpha_k = -\frac{F}{RT}y_{LiS,k}\left(1 - y_{LiS,k}\right)\frac{\partial U_k}{\partial y_{LiS,k}} \tag{J.34}$$

The material balance for LiS within the particles is assumed to be constant in the axial direction, but not radially.

$$c_{max}\frac{\partial y_{LiS,k}}{\partial t} = -\frac{1}{r^2}\nabla\left(r^2 N_{LiS,k}\right) \tag{J.35}$$

The aforementioned average transfer current density from the solid phase to the solution phase was defined according to the Butler-Volmer equation. The current density represents the charge-transfer associated with the insertion process. Considering the particle-scale kinetics, the exchange current density depends upon the mole fraction of LiS at the surface of the particle ($y_{s,k}$); where k_c^0 is the reaction rate constant.

$$i^0 = Fk_c^0 c^{1-\beta} c_{max}\left(1 - y_{s,k}\right)^{1-\beta} {y_{s,k}}^{\beta} \tag{J.36}$$

Furthermore, the equations pertaining to the porous electrode theory must be updated to account for the particle size distribution introduced for the VSSD model.

$$ai_n = \sum_k a_k i_{n,k} \tag{J.37}$$

$$i_{n,k} = i_0 \left[exp\left(\frac{\alpha_a F \eta_k}{RT}\right) - exp\left(-\frac{\alpha_c F \eta_k}{RT}\right)\right] \tag{J.38}$$

$$\eta_k = \Phi_1 - \Phi_2 - U_k \tag{J.39}$$